

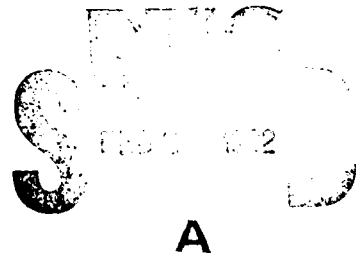
MICROCOPY RESOLUTION TEST CHART  
NATIONAL BUREAU OF STANDARDS-1963-A

AD A110282

FOREIGN TECHNOLOGY DIVISION



ACTA AERONAUTICA ET ASTRONAUTICA SINICA



BTIC FILE COPY

Approved for public release;  
distribution unlimited.



82 02 01 061

# EDITED TRANSLATION

14 FTD-ID(RS)T-1129-81

17 29 December 1981

MICROFICHE NR: FTD-81-C-002049

6 ACTA AERONAUTICA ET ASTRONAUTICA SINICA

English pages: 220

Source: *DTIC COPY INSPECTED* Acta Aeronautica et Astronautica Sinica, Vol. 2, Nr. 2, 1981, pp. 1-102

Country of origin: China

Translated by: LEO KANNER ASSOCIATES  
F33657-81-D-0264

Requester: FTD/TQTA

Approved for public release; distribution unlimited.



A

THIS TRANSLATION IS A RENDITION OF THE ORIGINAL FOREIGN TEXT WITHOUT ANY ANALYTICAL OR EDITORIAL COMMENT. STATEMENTS OR THEORIES ADVOCATED OR IMPLIED ARE THOSE OF THE SOURCE AND DO NOT NECESSARILY REFLECT THE POSITION OR OPINION OF THE FOREIGN TECHNOLOGY DIVISION.

PREPARED BY:  
TRANSLATION DIVISION  
FOREIGN TECHNOLOGY DIVISION  
WP.AFB, OHIO.

## TABLE OF CONTENTS

OSCILLATORY SUBSONIC POTENTIAL FLOWS AROUND THREE-DIMENSIONAL BODIES AND ITS APPLICATION TO THE CALCULATION OF DYNAMIC STABILITY DERIVATIVES OF THE AIRCRAFT	1
Liu Qiangang, Wu Changlin and Jian Zhen (Northwestern Polytechnical University)	
AN INTERPOLATION MIXED DIFFERENTIAL METHOD FOR TRANSONIC LARGE DISTURBED SYMMETRICAL POTENTIAL FLOW AROUND AIRFOIL	18
Ling Heyao (Design Department of Hongan Aircraft Company)	
THE CALCULATION OF LIFT AND DRAG CHARACTERISTICS OF SUBSONIC WINGS WITH WINGLETS	36
Zhou Renliang (Nanjing Aeronautical Institute)	
A NEW MODEL FOR PREDICTING OVERLOAD RETARDATION EFFECT IN FATIGUE CRACK PROPATATION	52
He Qingzhi (Beijing Institute of Aeronautics and Astronautics)	
J-INTEGRAL EXPERIMENTAL CALIBRATION OF SHEET SPECIMENS WITH SINGLE EDGE NOTCH	68
Liu Ligeng, Chen Xianxi and Cai Qigong (Central Iron and Steel Research Institute)	
ON THE DESIGN OF TRANSONIC TURBINE CASCADE BY HODOGRAPH METHOD	82
Ling Zhiguang (Institute of Engineering Thermophysics Academia Sinica) Xin Shaokang and Zhu Shican (Fudan University)	

THREE DIMENSIONAL STRESS ANALYSIS FOR A SHROUDED AIR-COOLED TURBINE BLADE	119
Shung Changbing and Xiao Junxiang (Beijing Institute of Aeronautics and Astronautics)	
A STUDY OF THE METHODS FOR MEASURING A RADAR'S ECCM PERFORMANCE	142
Li Nengjing (PLA Air Force Laboratory)	
AIMING COMPUTATION FOR FIGHTER WEAPON AIMING SYSTEM	184
Zhang Sen (Optic Machinery Research Institute)	
THE OPTIMUM DESIGN OF NON-MOMENT LAMINATED COMPOSITE PLATE - According to static failure strength condition -	201
Ma Zukang (Northwestern Polytechnical University)	
Brief Reports on Academic Activities	
BRIEF REPORT ON THE FIRST FLIGHT TEST RESEARCH ACADEMIC EXCHANGE MEETING	182

OSCILLATORY SUBSONIC POTENTIAL FLOWS AROUND THREE-DIMENSIONAL BODIES AND ITS APPLICATION TO THE CALCULATION OF DYNAMIC STABILITY DERIVATIVES OF THE AIRCRAFT

Liu Qiangang, Wu Changlin and Jian Then  
(Northwestern Polytechnical University)

Abstract

This article introduces a unified method for processing the oscillatory subsonic potential flows around three-dimensional bodies of various configurations. The major feature of this method is the employment of the finite element method to directly explain the use of the integro-differential equation for the velocity potential on the surface of the body derived from the Green theorem to obtain the velocity potential distribution on the surface of the body. Later, we further used the finite difference method for the differential of the velocity potential so as to obtain the pressure distribution on the surface of the body.

Due to the fact that theoretically this method is relatively stringent, when used for the calculation of flows around bodies with complex configurations the obtained results were relatively accurate. Because of this, in the last several years its application has become more and more widespread abroad. Similar basic equations from related reference [3] were utilized, yet there were dissimilarities in the calculation of the aerodynamic influence coefficient. This article also applies this method for the calculation of dynamic stability derivatives of the aircraft and the obtained results are in agreement with the experimental results.

## I. Perturbation Velocity Potential and Boundary Conditions

If we take a right angle coordinate system such as the one shown in fig. 1 (in the figure the OX axis direction is identical to the undisturbed air flow speed of the y direction) under small perturbation, there is the following perturbation velocity potential equation:

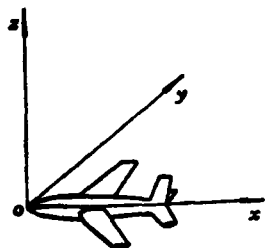


Fig. 1.

$$\frac{\partial^2 \varphi}{\partial x^2} + \frac{\partial^2 \varphi}{\partial y^2} + \frac{\partial^2 \varphi}{\partial z^2} - \frac{1}{c_0^2} \left( U^2 \frac{\partial^2 \varphi}{\partial x^2} + 2U \frac{\partial^2 \varphi}{\partial x \partial t} + \frac{\partial^2 \varphi}{\partial t^2} \right) = 0 \quad (1)$$

In the formula,  $\varphi$  is the perturbation velocity potential,  $c_0$  is the speed of sound in the undisturbed air flow and  $t$  is the time.

If we can use the following equation to show the surface of the body:

$$s(x, y, z, t) = 0 \quad (2)$$

then the boundary conditions of the surface of the body is:

$$\varphi^{(n)} \equiv \frac{\partial \varphi}{\partial n} = \frac{Vs}{|\nabla s|} \nabla \varphi = -\frac{1}{U|\nabla s|} \left( \frac{\partial s}{\partial t} + U \frac{\partial s}{\partial x} \right) \quad (3)$$

In the formula,  $n$  is the outer normal line of the  $s$ .

The following transformation is carried out for the variables  $x, y, z, t$  and velocity potential  $\varphi$ :

$$\begin{aligned} X &= x/\beta L, \quad Y = y/L, \quad Z = z/L \\ T &= \beta t/L, \quad \phi = \varphi/UL \end{aligned} \quad (4)$$

In the formula,  $\beta = \sqrt{1 - M_\infty^2}$ ;  $M_\infty$  is the Mach number of the undisturbed air flow and  $L$  is the characteristic length of the body.

By applying the Green function method for the subsonic perturbation flow we obtained the following formula:

$$4\pi E\phi(p, T) = -\iint_{S_B} \left[ \frac{\partial\phi}{\partial N_1} \right]' \frac{1}{R} dS_B + \iint_{S_B} \left\{ (\phi)' \frac{\partial}{\partial N_1} \left( \frac{1}{R} \right) - \left[ \frac{\partial\phi}{\partial T} \right]' \frac{1}{R} \frac{\partial R}{\partial N_1} \right\} dS_B + \iint_{S_W} \left\{ (\Delta\phi)' \frac{\partial}{\partial N_1} \left( \frac{1}{R} \right) - \left[ \frac{\partial\Delta\phi}{\partial T} \right]' \frac{1}{R} \frac{\partial R}{\partial N_1} \right\} dS_W \quad (5)$$

In the formula,  $S_B$  and  $S_W$  separately indicate the surface of the body and the vortex surface of the body's trailing edge;  $\Delta\phi$  is the difference of the velocity potential on the top and bottom of the vortex surface;  $p(X, Y, Z)$  are points in the flow field;  $q(X_1, Y_1, Z_1)$  are points on the surface of the body or vortex surface;  $X_1, Y_1, Z_1$  are integral variables;  $N_1$  is the outer normal line of point  $q$ ;  $R$  is the distance between two points of  $p$  and  $q$ .

$$R = \sqrt{(X_1 - X)^2 + (Y_1 - Y)^2 + (Z_1 - Z)^2} \quad (6)$$

$r$  is the required time that the perturbation is emitted from point  $q$  and is transmitted to point  $p$ .

$$\tau = R + M_\infty(X_1 - X) \quad (7)$$

When the functions indicated in the brackets takes  $T_1 = T - \tau$ ;  $E$  is the parameter and when point  $p$  is above  $S_B$ ,  $E = 1/2$ . When point  $p$  is outside  $S_B$  and not above  $S_W$  then  $E = 1$ .

When point  $p$  is above  $S_B$ , formula (5) takes  $\phi$  as the integro-differential equation of the unknown function. It can be used to calculate the velocity potential distribution of the surface of the body.

It is worthy to note that in formula (5) the velocity potential difference  $\Delta\phi$  on the top and bottom of the vortex surface is actually not another unknown quantity. It can be determined by the difference on the top and bottom of the

trailing edge of the surface of the body:

$$\Delta\phi(q, T_1) = \Delta\phi(q_{TE}, T_1 - \mu_1) \quad (8)$$

In the formula,  $q_{TE}$  and  $q$  separately indicate points on the trailing edge of the surface of the body and the vortex surface. Moreover, when they are on the same vortex line;  $\mu_1$  is the required time of the vortex point flowing from point  $q_{TE}$  to point  $q$ :

$$\mu_1 = \beta^2(X_1 - X_{TE})/M_\infty \quad (9)$$

In the formula,  $X_{TE}$  is the X coordinate of point  $q_{TE}$ .

The above integro-differential equation can use the finite element method to seek a solution. In order to solve this equation, we divided the surface of the body into  $N_B$  quadrilateral elements and took the  $\left(\frac{\partial\phi}{\partial N}\right)^r$ ,  $(\phi)^r$ ,  $\left(\frac{\partial\phi}{\partial T}\right)^r$  in each of the elements to be constants and be equal to their values in the figure centers of each of the elements. At the same time, all of the vortex lines are divided on the vortex surface and each of the vortex lines and series of elements on the surface of the body are joined. The length of the vortex line can take any effective length.<sup>[6]</sup> Each vortex line is further divided into many quadrilateral elements and the value of  $(\Delta\phi)^r$ ,  $\left(\frac{\partial\Delta\phi}{\partial t}\right)^r$  in each element are also assumed to be constants and be equal to their values in the figure centers of each of the elements. At the same time, we also considered the Kutta conditions and the trailing edge's  $\Delta\phi$  of the surface of the body could be considered to be approximately equal to the  $\Delta\phi$  value of the trailing edge's joined element figure centers. Therefore, formula (8) can be written as:

$$\Delta\phi_s(T - \tau_{ih}) = \sum_j K_{jh} \phi_j(T - \tau_{ih} - \mu_h) \quad (10)$$

In the formula,  $i$  and  $j=1$  and  $2 \dots N_B$  is the serial number of the element on the surface of the body;  $h=1$  and  $2 \dots N_W$  is the

serial number of the element on the vortex surface ( $N_w$  is the total of elements on the vortex surface);  $K_{jh}$  is the coefficient, and when the element  $j$  is joined with the trailing edge of the surface of the body and the element  $h$  is on the trailing edge vortex line of the element  $j$ ,  $K_{jh} = \pm 1$  (when the element  $j$  is on the top surface it takes a "+" and when on the bottom surface it takes a "-") otherwise  $K_{jh} = 0$ ;  $\Delta\phi$  indicates the  $\Delta\phi$  of the  $h$  element's figure center on the vortex surface;  $\phi_j$  indicates the  $\phi$  of the  $j$  element's figure center on the surface of the body;  $\tau_{jh}$  is the time required for the perturbation to be transmitted from the  $h$  element's figure center on the vortex surface to the  $i$  element's figure center on the surface of the body;  $\mu_h$  is the time required for the vortex point to flow from the  $\rho_{TE}$  point to the  $h$  elements figure center. In considering the use of the above approximation, when calculating  $\mu_h$ , the trailing edge's coordinate  $X_{TE}$  of the surface of the body and the trailing edge's joined  $X$  coordinates of the surface body element figure center can substitute so that the  $\mu_h$  in formula (10) can be written as:

$$\mu_h = \beta^2 (X_h - X_j) / M_\infty \quad (11)$$

In the formula,  $X_h$  and  $X_j$  separately indicate the  $h$  element on the vortex surface and the  $X$  coordinate of the  $j$  element figure center on the surface of the body.

After undergoing the above process, when the  $p$  point was on the  $S_B$ , formula (5) changed into a constant differential equation with a constant coefficient and linear time difference variable:

$$\begin{aligned} \phi_i(T) = & \sum_j b_{ij} \phi_j^{(n)}(T - \tau_{ij}) + \sum_j C_{ij} \phi_j(T - \tau_{ij}) + \sum_j D_{ij} \dot{\phi}_j(T - \tau_{ij}) \\ & + \sum_j \sum_k K_{jk} C_{ik} (T - \tau_{ik} - \mu_k) \\ & + \sum_j \sum_k K_{jk} D_{ik} \dot{\phi}_j(T - \tau_{ik} - \mu_k) \quad i = 1, 2 \dots N_s \end{aligned} \quad (12)$$

In the formula,  $\tau_{ij}$  is the time required for the perturbation to be transmitted from the  $j$  element's figure center of the surface of the body to the  $i$  element's figure center;  $\dot{\phi}_j = \left(\frac{\partial \phi}{\partial T}\right)_j$ ,  $\phi_j^{(N)} = \frac{\partial \phi}{\partial N_j}$ ,  $b_{ij}$ ,  $C_{ij}$ ,  $D_{ij}$ ,  $C_{ih}$ ,  $D_{ih}$  are the aerodynamic influence coefficients:

$$\begin{aligned}
 b_{ij} &= -\frac{1}{2\pi} \iint_{S_{Bj}} \frac{1}{R} dS_{Bj} \\
 C_{ij} &= \frac{1}{2\pi} \iint_{S_{Bj}} \frac{\partial}{\partial N_i} \left( \frac{1}{R} \right) dS_{Bj} \\
 D_{ij} &= -\frac{1}{2\pi} \iint_{S_{Bj}} \frac{1}{R} \frac{\partial R}{\partial N_i} dS_{Bj} \\
 C_{ih} &= \frac{1}{2\pi} \iint_{S_{Wh}} \frac{\partial}{\partial N_i} \left( \frac{1}{R} \right) dS_{Wh} \\
 D_{ih} &= -\frac{1}{2\pi} \iint_{S_{Wh}} \frac{1}{R} \frac{\partial R}{\partial N_i} dS_{Wh}
 \end{aligned} \tag{13}$$

In the formula,  $S_{Bj}$  indicates the surface of the  $j$  element on the surface of the body;  $S_{Wh}$  indicates the surface of the  $h$  element on the vortex surface;  $b_{ij}$  and  $C_{ij}$  can use analytic formula calculation - the formula for calculating  $C_{ih}$  is the same as for  $C_{ij}$  only it is necessary to change the  $j$  into an  $h$  in the formula. For approximate calculation, we could also use  $D_{ij} = R_{ij} C_{ij}$  and  $D_{ih} = R_{ih} C_{ih}$ : In these formulas  $R_{ij}$  and  $R_{ih}$  are separately the  $j$  element on the surface of the body and distance from the  $h$  element's figure center on the vortex surface to the  $i$  element's figure center on the surface of the body.

Equation (12) can be used to calculate the indeterminate constant flow around bodies.

## II. Calculation Formula for Harmonic Oscillatory Flows Around Bodies

When a body revolves around its fixed constant reference state and creates harmonic oscillation, its additional perturbation velocity potential can be shown as:

$$\phi(X, Y, Z, T) = \hat{\phi}(X, Y, Z) e^{i\Omega(T + M_\infty X)} \quad (14)$$

In the formula:

$$\Omega = \omega L / a_\infty \beta = K M_\infty / \beta \quad (15)$$

In this formula,  $\omega$  is the oscillation frequency;  $K$  is the conversion frequency; and  $\Omega$  is the conversion frequency computed in the compressibility effect.

After the surface of the body is divided into a finite element, formula (14) can be written as:

$$\phi_j(T) = \hat{\phi}_j e^{i\Omega(T + M_\infty X_j)} \quad (16)$$

When formula (16) is substituted into formula (12), after arrangement, we obtained:

$$[\delta_{ij} - \hat{c}_{ij} - \hat{w}_{ij}] \{\hat{\phi}_j\} = \{\hat{b}_{ij}\} \{\hat{\phi}_j^{(N)}\} \quad (17)$$

In the formula,  $\delta_{ij}$  is the Kronecker function, when  $i \neq j$  then  $\delta_{ij} = 0$ , and when  $i = j$  then  $\delta_{ij} = 1$ .

$$\hat{c}_{ij} = e^{-i\Omega R_{ij}} (1 + i\Omega R_{ij}) C_{ij} \quad (18)$$

$$\hat{b}_{ij} = e^{-i\Omega R_{ij}} b_{ij} \quad (19)$$

$$\hat{w}_{ij} = \sum_h K_{jh} e^{-iK(x_h - x_j + M_\infty R_{jh})/\beta} (1 + i\Omega R_{jh}) C_{jh} \quad (20)$$

When the body creates harmonic oscillation, the equation for the surface of the body can be written as:

$$s(X, Y, Z, T) = Z - Z_{u,1}(X, Y) \mp \tilde{Z}(X, Y) e^{i\Omega T} \quad (21)$$

In the formula, "-" corresponds to the upper surface; "+" corresponds to the lower surface; footnote u indicates the upper

surface,  $l$  indicates the lower surface, and  $\tilde{z}(x, y)$  is the model of vibration. Therefore, the boundary condition of the oscillatory flow around the surface of the body can be written as:

$$\hat{\phi}^{(N)} = N_z \left( iK\tilde{z} + \frac{1}{\beta} \frac{\partial \tilde{z}}{\partial X} \right) e^{-i\omega M_\infty x} \quad (22)$$

In the formula,  $N_z$  is the cosine of the constant reference state of the outer normal line  $N$  on the surface of the body and the  $oZ$  axis included angle.

In general, for indeterminate motion, the pressure coefficient can be calculated according to the following formula:

$$C_p = -2 \left( \frac{\beta}{M} \frac{\partial \phi}{\partial T} + \frac{1}{\beta} \frac{\partial \phi}{\partial X} \right) \quad (23)$$

and for the harmonic oscillatory flow around the body:

$$C_p = \tilde{C}_p e^{i\omega T} \quad (24)$$

From formulas (23), (24) and (14) we obtained:

$$\tilde{C}_p = -\frac{2}{\beta} e^{iK\beta x} \frac{\partial}{\partial X} (\hat{\phi} e^{iKx/\beta}) \quad (25)$$

When calculating the numerical value, the finite difference method could be used for the differential in the above formula.

After ascertaining the geometric parameters of the surface of the body and the boundary conditions, we could explain equation group (17) and obtain the  $\hat{\phi}_j$  value ( $j=1, 2, \dots, N_B$ ) of the  $N_B$  dispersion points on the surface of the body. Further, we could also obtain the pressure distribution from formula (25).

### III. Its Application to the Calculation of Dynamic Stability Derivatives of the Aircraft

Equation (17) has been applied for the calculation of a

great many types of oscillatory flows around bodies. It can be used to calculate aircraft fluttering, the effects of gusts and the indeterminate aerodynamic forces when the aircraft makes other various oscillatory movements. In this section, we will present calculations for the pressure distribution and dynamic stability derivatives when an aircraft creates pitch oscillation as concrete applications of this method.

If after the aircraft has perturbation at a certain equilibrium and this revolves around its center of gravity creating pitch oscillation, its model of vibration can be indicated as:

$$\ddot{Z}_1 = a_0(X_g - X_1) \beta \quad (26)$$

In the formula,  $X_{\xi}$  is the x coordinate of the aircraft's center of gravity.

Based on the method introduced in the above section, we can obtain, at this time, the variable pressure coefficient  $\tilde{C}_{p0}$  of the aircraft's surface and carrying out the integral of this variable pressure coefficient obtain:

$$\tilde{C}_L = \tilde{C}_L^R + i\tilde{C}_L^I \quad (27)$$

$$\tilde{C}_m = \tilde{C}_m^R + i\tilde{C}_m^I \quad (28)$$

In the formula, letters R and I separately indicate the real part and imaginary part. At this time, the aircraft's lift and pitching-moment coefficient are separately:

$$C_L = RL(\tilde{C}_L e^{i\omega t}) \quad (29)$$

$$C_m = RL(\tilde{C}_m e^{i\omega t}) \quad (30)$$

In the formula, "RL" indicates the real part.

On the other hand, after the aircraft has perturbation and creates pitch oscillation, its lift and pitching-moment coefficient can be indicated as:

$$C_L = C_{L\alpha} \alpha + C_{L\dot{\alpha}} \left( \frac{\dot{\alpha} L}{v} \right) + C_{L\dot{\theta}} \left( \frac{\dot{\theta} L}{v} \right) \quad (31)$$

$$C_m = C_{m\alpha} \alpha + C_{m\dot{\alpha}} \left( \frac{\dot{\alpha} L}{v} \right) + C_{m\dot{\theta}} \left( \frac{\dot{\theta} L}{v} \right) \quad (32)$$

In the formula,  $\bar{\alpha} = \frac{\dot{\alpha} L}{v}$ ,  $\bar{\theta} = \frac{\dot{\theta} L}{v}$ .

In the above two formulas, the small amounts above the second order are omitted. (5)

When the aircraft has pitch harmonic oscillation, the increment of its attack angle and pitch angle is:

$$\alpha = \theta = \alpha_0 R L (e^{j\omega t}) \quad (33)$$

From formulas (29)-(33) we obtain:

$$\tilde{C}_L = \alpha_0 [C_{L\alpha} + iK(C_{L\dot{\alpha}} + C_{L\dot{\theta}})] \quad (34)$$

$$\tilde{C}_m = \alpha_0 [C_{m\alpha} + iK(C_{m\dot{\alpha}} + C_{m\dot{\theta}})] \quad (35)$$

In comparing the imaginary parts of formulas (27) and (34) and formulas (28) and (35) we obtain:

$$C_{L\dot{\alpha}} = \frac{\tilde{C}_L'}{\alpha_0 K} - C_{L\dot{\theta}} \quad (36)$$

$$C_{m\dot{\alpha}} = \frac{\tilde{C}_m'}{\alpha_0 K} - C_{m\dot{\theta}} \quad (37)$$

Therefore,  $C_{L\dot{\theta}}$  and  $C_{m\dot{\theta}}$  can be obtained under fixed constant hypothetical conditions. The value of the dissimilar conversion frequency times of  $C_{L\dot{\alpha}}$  and  $C_{m\dot{\alpha}}$  can be obtained from formulas (36) and (37).

#### IV. Calculation Examples

We applied the above method in a TQ-6 electron computer at the Optical Machine Institute of the Chinese Academy of

Sciences in Xian for the calculation of aircraft wings, ellipsoids, the lift distribution of the pitch harmonic oscillation created by a certain aircraft (aircraft wing, fuselage, tail assembly) and the dynamic stability derivatives  $C_{L\dot{\alpha}}$  and  $C_{m\dot{\alpha}}$  of an aircraft. The results were as follows :

### 1. Aircraft Wings

The form of the plane's aircraft wing was rectangular, the aspect ratio was  $\lambda=2$ , the relative thickness was  $\bar{c}=0.001$ , it revolved on a  $x=c/2$  axis to create harmonic oscillation and when in  $M_\infty=0$  and  $K=2$  its lift distribution was as shown in figure 2.

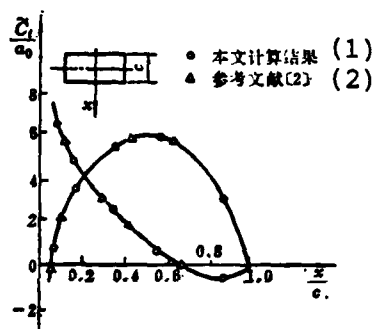


Fig. 2. The Lift Distribution of the Rectangular Wing Root Chord Area When a Rotating  $x=c/2$  Axis Creates Harmonic Oscillation

1. Results of this article's calculations
2. Reference work [2]

It can be seen from figure 2 that the results of this article's calculations are identical to those of reference work [2]. Because the divisions into pieces were relatively few, the lift distribution of the trailing edge section near the aircraft wing was not given accurate calculation values by reference work [2]. They only used a curve to indicate its distribution tendency. Yet, in this article, because we used the already known conditions of the  $\Delta\phi$  value on the vortex surface, although the division into pieces were few, accurate calculation results were still obtained for the trailing edge section near the aircraft wing.

## 2. Ellipsoids

The ratio of the major axis and minor axis of the ellipsoid was 8. It revolved around the center to create pitch harmonic oscillation. Its pressure distribution is shown in chart 3.

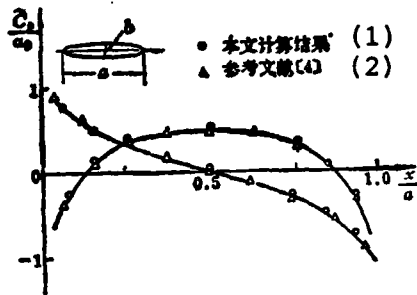


Chart 3 The Pressure Distribution When an  $a/b=8$  Ellipsoid Creates Pitch Harmonic Oscillation

1. Results of this article's calculations
2. Reference work [4]

In the chart, the results shown by the symbol " $\Delta$ " are the analytically interpreted calculations obtained by reference work [4] based on Helmholtz's wave motion equation. It can be seen from the chart that given the situation of few divisions into pieces (only 54 pieces were divided on half an ellipsoid), the results of this article's calculations were still relatively the same as the analytical interpretations.

## 3. Aircraft Wings, Fuselage and Tail Assembly

Below we will give the test results of a certain aircraft (aircraft wings, fuselage, tail assembly) when it uses different frequencies to revolve around its center of gravity and create pitch harmonic oscillation. The outer geometrical

form of the aircraft is generally as is shown in figure 4.

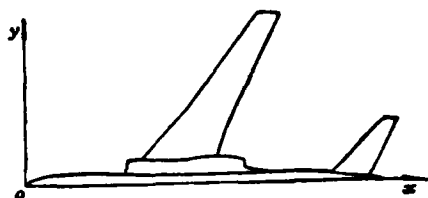


Fig. 4.

Strictly speaking, the dynamic stability derivative should have the oscillation frequency be close to zero. Because of this, we took a relatively small numerical value in the calculation yet this did not cause any apparent calculation errors in frequency when calculating the frequency. Figures 5, 6 and 7 separately show the lift on certain sections of the aircraft wings and tail surface, and the pressure distribution on a certain meridian along the fuselage when the aircraft used these frequencies to create pitch harmonic oscillation.

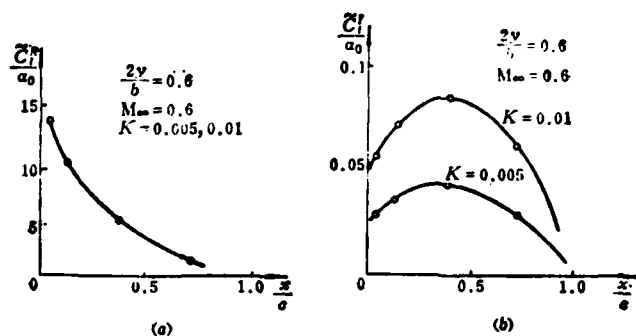


Fig. 5. The Lift Distribution on a Certain Section of the Aircraft Wing When a Certain Aircraft Revolves Around Its Center of Gravity and Creates Pitch Harmonic Oscillation

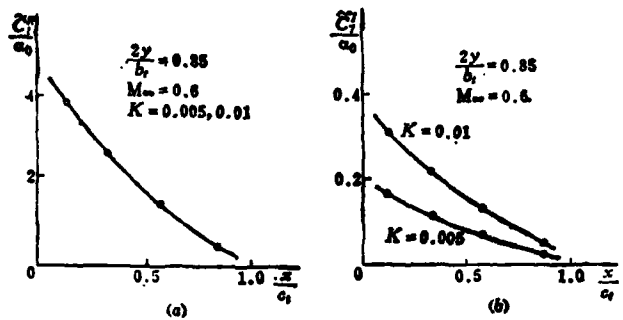


Fig. 6. The Lift Distribution on a Certain Section of a Flat Wing When a Certain Aircraft Revolves Around Its Center of Gravity and Creates Pitch Harmonic Oscillation

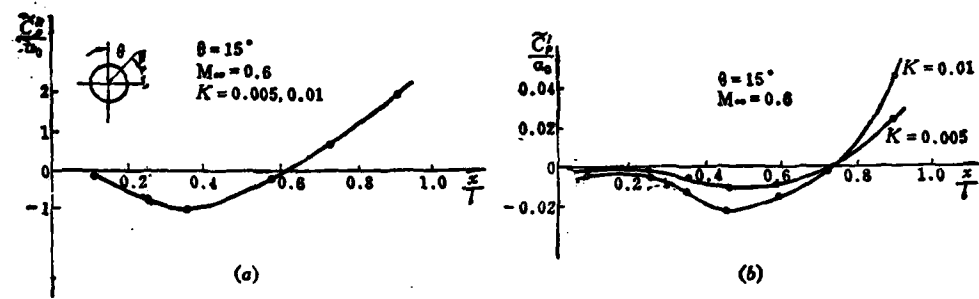


Fig. 7. The Pressure Distribution on a Certain Meridian Along the Fuselage When a Certain Aircraft Revolves Around Its Center of Gravity and Creates Pitch Harmonic Oscillation

See table 1 for the calculation results of the aircraft's  $\tilde{C}_m/\alpha_0$  and dynamic stability derivative  $C_{m\dot{\alpha}}$  when  $M_\infty = 0.6$ .

$K$	$\tilde{C}_m^1/\alpha_0$	$C_{m\dot{\alpha}}$
0.005	-0.0545	-1.787
0.01	-0.109	-1.787

Table 1

In the calculations, the aircraft's  $C_{m\dot{\alpha}}$  uses  $-9.119^{(1)}$ .

It can be seen from table 1 that when  $Mach_\infty = 0.6$ , the aircraft's  $C_{m\dot{\alpha}}$  can use  $-1.787$ .

Therefore, in recently published works, we still have not seen theoretical calculations or experiment results for the indeterminate aerodynamic force of aircraft wings, fuselage and tail assembly. The above calculations in this article are still not suitable material to offer for comparison. Yet, at present, we already have test results for the dynamic stability derivatives of the aircraft. See table 2 for the dynamic stability derivative test values of the aircraft when at  $Mach_\infty = 0.6$ .

	$C_{m\dot{\alpha}}$	$C_{m\ddot{\alpha}}$
(1) 实验值	-1.864	-9.529
(2) 计算值	-1.787	-9.119

Table 2

1. Test value
2. Calculated value

It can be seen from table 2 that the test values of the

aircraft's dynamic stability derivatives are quite close to the calculated values of reference work (1). This also explains in one sense, this article's calculated results of the indeterminate aerodynamic force of the aircraft wings, fuselage and tail assembly.

## V Conclusion

This article introduced a unified method for processing the oscillatory subsonic potential flows around three dimensional bodies of various configuration. It also presented calculation results for the indeterminate aerodynamic force and dynamic stability derivatives of a single wing, ellipsoids, aircraft wings and tail assemblies when different frequencies were used to create pitch harmonic oscillation. Actual calculations showed that the application range of this method is quite wide and can be used for the calculation of the oscillatory flows around bodies of various different and complex configurations. Moreover, the amount of calculation work is relatively small and the results are relatively accurate. At present, then, this is a good method for calculating oscillatory subsonic flows.

## References

1. Liu Qiangang, Wu Changlin and Jian Zheng, The Calculation of the Pressure Distribution and Aerodynamic Derivatives of Quasi-Static Elastic Aircraft, Northwestern Polytechnical University Scientific and Technical Data, no. 1024 (1979).
2. L. Morino, and C.C. Kuo, Subsonic Potential Aerodynamics for Complex Configurations, A General Theory, AIAA Journal, Vol.12, No. 2, 1974.
3. K. Tseng, and L. Morino, Fully Unsteady Subsonic and Supersonic Potential Aerodynamics of Complex Aircraft Configurations for Flutter Applications, AIAA/ASME/SAE 17th Structures, Structural Dynamics and Materials Conference Proceedings, 1976.

4. K. L. Chao, and H. Försching, Prediction of Unsteady Airloads on Harmonically Oscillating Spheroids Based on an Analytical Solution of the Governing Wave Equation, *Zeitschrift für Flugwissenschaften und Weltraumforschung*, Jan./Feb. 1974.
  
5. William P. Rodden, and Joseph P. Giesing, Application of Oscillatory Aerodynamic Theory to Estimation of Dynamic Stability Derivatives, *Journal of Aircraft*, Vol. 7, No. 3, 1970.
  
6. Lee-Tzong Chen, Steady and Oscillatory, Subsonic and Supersonic Aerodynamic Pressure and Generalized Forces for Complex Aircraft Configurations and Applications to Flutter, CR. 142983, 1975.

# OSCILLATORY SUBSONIC POTENTIAL FLOWS AROUND THREE-DIMENSIONAL BODIES AND ITS APPLICATION TO THE CALCULATION OF DYNAMIC STABILITY DERIVATIVES OF THE AIRCRAFT

*Liu Qiangang, Wu Changlin and Jian Zheng*  
(Northwestern Polytechnical University)

## Abstract

A general formulation for oscillatory subsonic potential flows around three-dimensional bodies of various configuration and its application to the calculation of dynamic stability derivatives of the aircraft are presented. By applying the Green function method, we obtained an integro-differential equation relating the perturbation velocity potential to its normal derivatives on the surface of the body. In order to solve this equation, the surface of the body and its wave are divided into small quadrilateral elements. The unknown  $\phi$  and its derivatives are assumed to be constant within each element. Thus the integro-differential equation reduces to a set of differential-delay equations in time. This set of equations can be used as the basis of a general method for the fully unsteady flow calculation. For oscillatory subsonic potential flow, this set of equations further reduces to a set of linear algebraic equations which is solved numerically to yield the values of  $\phi_i$  at the centroid of each element. The pressure coefficient is evaluated by the finite difference method. The lift and the moment coefficients are determined by numerical integration of the pressure coefficient. The dynamic stability derivatives are obtained from the imaginary parts of the lift and the moment coefficients.

The formulations in this paper are embedded into a general computer program. Several typical numerical results have been obtained by means of this program. Figure 2 shows the distribution of lift coefficient  $\tilde{C}_L$  along the middle section for a rectangular wing oscillating in pitch with  $\lambda = 2$ ,  $\tau = 0.001$ ,  $M_\infty = 0$ ,  $K = 2$ . The result is identical to the original calculation by Morino<sup>(4)</sup>. Figure 3 shows the distribution of pressure coefficient  $\tilde{C}_p$  for a harmonically oscillating spheroid with  $\frac{a}{b} = 8$ ,  $M_\infty = 0.5$ ,  $K = 2$ . The result is in good agreement with the analytical solution of wave equation<sup>(4)</sup>. Figures 5, 6, 7 show the distributions of lift coefficient  $\tilde{C}_L$  at various stations of an aircraft (wing-body-tail combination) oscillating in pitch with  $M_\infty = 0.6$ ,  $K = 0.005, 0.01$ . Table 2 shows the dynamic stability derivatives  $C_{L\dot{\alpha}}$ ,  $C_{m\dot{\alpha}}$  of the aircraft. The results are in good agreement with the experimental data.

AN INTERPOLATION MIXED DIFFERENTIAL METHOD FOR TRANSONIC LARGE  
DISTURBED SYMMETRICAL POTENTIAL FLOW AROUND AIRFOIL

by Ling Heyao

(Design Department of Hongan Aircraft Company)

Abstract

By extending an interpolation mixed differential method[1] for transonic small disturbed steady potential flow to the transonic large disturbed steady potential flow, we proposed an interpolation mixed differential method for solution of the exact equation for transonic potential flows in the local speed coordinate system. In numerical illustration of this method, the pressure distributions of the double arc airfoil and NACA0015 airfoil in symmetrical state are computed and compared with the data of the experiments [2,3] and the results of the computation for the double arc airfoil by the small disturbed mixed differential method. The results were close. The computations proved that the interpolation mixed differential scheme is stable and convergent. This paper has solved the difficulty of computing the Mach  $\infty$  number which near 1.

I. Preface

Since 1970 when Murman and Cole[4] proposed the use of an interpolation mixed differential method for solving the transonic small disturbed potential flow equation, various different methods have continued to appear for the solution of transonic flow and development has been very fast. Beginning from the end of 1973, using reference [4] as a basis, Professor Luo Shijun further developed and extended the computation and application

of transonic steady disturbed potential flow and obtained a great many results[1]. In order to extend the application range of the mixed differential method, reference [6] extended the mixed differential scheme for the transonic small disturbed potential flow to the transonic large disturbed potential flow. The revolving mixed differential scheme was proposed whereupon computation results were obtained for the obtuse flow around the body yet the amount of computation work was relatively large. Because of this, this article proposes a new computation method which is an interpolation mixed differential method for the local speed coordinate system.

## II. Speed Potential Equation in the Local Speed Coordinate System

In a plane flow, the exact speed potential equation is:

$$(a^2 - u^2)\phi_{xx} + (a^2 - v^2)\phi_{yy} - 2uv\phi_{xy} = 0 \quad (1)$$

In the formula,  $a$  indicates the speed of sound;  $u$  and  $v$  separately indicate the speed component along the  $x$  and  $y$  coordinate axes; and  $\phi(x, y)$  indicates the speed potential.

In the son local speed coordinate system,  $s$  is the tangent of the 0 point on the flow line and  $n$  is the normal line of the 0 point on the flow line (see fig. 1). In the local speed coordinate system, the local speed  $q$  is identical to the  $s$  axis. Because of this, there is no division of speed in the  $n$  axis direction.

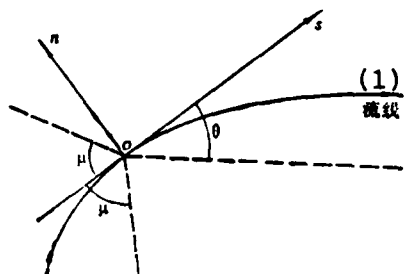


Fig. 1. The Local Speed Coordinate System

Key: 1. Flow line

Based on this, when equation (1) is converted to the local speed coordinate system, it possesses the following equation form:

$$(a^2 - q^2)\phi_{ss} + a^2\phi_{nn} = 0 \quad (2)$$

When the two sides of formula (2) are divided by  $a^2$ , we obtain:

$$(1 - M^2)\phi_{ss} + \phi_{nn} = 0 \quad (3)$$

In the formula,  $M=q/a$  is the local Mach number.

Equation (3) is a non-linear partial differential equation. Given that the  $1-M^2$  item can be positive, negative or zero, it is also an equation which can be an equational form in a flow line for an elliptical form, hyperbolic form or parabolic form. Because of this, equation (3) is a mixed form and the solution of the flow field is a mixed problem.

In the supersonic or sonic range, equation (3) is a hyperbolic form or parabolic form with an existing group of characteristic lines. In the local coordinate system, the characteristic line is symmetrical to the local speed axis and furthermore the characteristic line makes a local Mach angle  $\mu$  with

the included angle of the local speed. Thus, the characteristic line is exactly the local Mach angle. In the small disturbed plane potential flow, the characteristic line is symmetrical to the basic coordinate axis, and the two situations of the characteristic line equation forms in each coordinate system are completely identical. Because of this, in the same way we conclude that the stability of the differential scheme in the small disturbed potential flow is appropriate for the large disturbed plane potential flow in the local speed coordinate system.

### III. The Fitting and Interpolation of the Speed Potential Surface

The speed potential surface in the binary flow is a complex surface. It is necessary to use a single function to express the formula exactly and this is actually impossible. We should use, based on the network's nodal point distribution, any "speed potential surface piece" to describe it. Within each speed potential surface piece the smoothness requirements in the speed potential curved surface piece should be guaranteed. In this way, after joining with a suitable form of a speed potential surface piece, nearly any form of speed potential surface piece can express it and thus the required accuracy can be attained.

Based on reference work [7], we can find the boundary line for the ruled surface interpolation formula of the line. The angular point of the already known ruled surface is 00,01,10,11 (see figure 2). We can form a set of boundary lines:

$$0^n = (00 \ 01) \begin{bmatrix} F_0 \\ F_1 \end{bmatrix} \quad (4)$$

$$1^n = (10 \ 11) \begin{bmatrix} F_0 \\ F_1 \end{bmatrix} \quad (5)$$

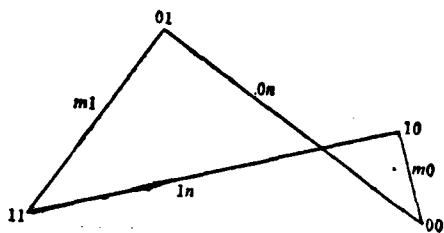


Fig. 2. The Position Information of the Ruled Surface Angular Points

After attaining these two lines, the identical parameter value  $n$  points on their surface are viewed as corresponding points and lines are drawn in each of the pairs of corresponding points in the same manner. When this type of line becomes the  $m$  line on the ruled surface, we obtain the  $m$  line formula:

$$mm = (F_0 \ F_1) \begin{bmatrix} 0 \ n \\ 1 \ n \end{bmatrix} \quad (6)$$

When we make this type of  $m$  line the "generating line" and the slip on the two "base lines" of formulas (4) and (5) causes the  $n$  to change from 0 to 1, we obtain the total  $m$  line of the ruled surface. This is also the scanning of the entire ruled surface. Thus, formula (6) is an equation for the ruled surface.

Using formulas (4) and (5), we can write formula (6) as:

$$(mm) = (F_0 \ F_1) \begin{bmatrix} 00 & 01 \\ 10 & 11 \end{bmatrix} \begin{bmatrix} F_0 \\ F_1 \end{bmatrix} \quad (7)$$

The entire element in the divalent square matrix on the right side of the formula is the constant vector and they are

all position information of the angular points on the ruled surface angular points. Therefore, this square matrix is called the angular point information square matrix. The information in the square matrix is easily provided by actual problems and formula (7) is also convenient for numerical computations.

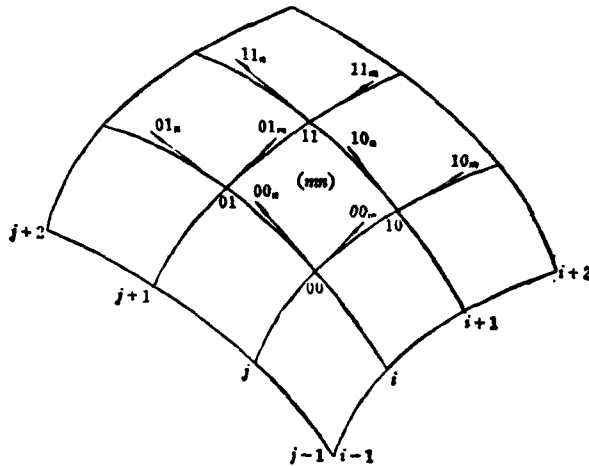


Fig. 3. Double Cubic Surface

If the known surface boundary lines are cubic functions, then they accordingly form a ruled surface equation which in turn can form a double cubic surface interpolation formula (see fig. 3). Without undergoing deductions, an equation is given similar to formula (7):

$$(mn) = (F_0, F_1, G_0, G_1) \begin{pmatrix} 00 & 01 & 00_s & 01_s \\ 10 & 11 & 10_s & 11_s \\ 00_{ss} & 01_{ss} & 00_{sss} & 01_{sss} \\ 10_{ss} & 11_{ss} & 10_{sss} & 11_{sss} \end{pmatrix} \begin{pmatrix} F_0 \\ F_1 \\ G_0 \\ G_1 \end{pmatrix} \quad (8)$$

Functions  $F_0, F_1, G_0$  and  $G_1$  in formulas (7) and (8) are called mixed functions[7]. The complete elements in the tetravalent square matrix of formula (8) are constant vectors. They are all

position vector, tangent vector and torsional vector information on the angular points.

The tangent vectors and torsional vectors on the surface's (mn) four angular points can use the differential method computation (see fig. 3). The tangent vector differential formula on the ij nodal point is:

$$ij_m = \frac{(i+1, j) - (i-1, j)}{\Delta m_{i,j} + \Delta m_{ij}} + 0(\Delta) \quad (9)$$

$$ij_n = \frac{(i, j+1) - (i, j-1)}{\Delta n_{i,j} + \Delta n_{ij}} + 0(\Delta) \quad (10)$$

$\Delta m$  and  $\Delta n$  are the nodal points of the two parametric change directions.

The torsion vector differential formula on the ij nodal point is:

$$ij_{mn} = \frac{1}{\Delta n_{i,j-1} + \Delta n_{ij}} \left[ \frac{(i+1, j-1) - (i-1, j-1)}{\Delta m_{i-1,j-1} + \Delta m_{i,j-1}} - \frac{(i+1, j+1) - (i-1, j+1)}{\Delta m_{i-1,j+1} + \Delta m_{i,j+1}} \right] + 0(\Delta) \quad (11)$$

The tangent vectors and torsion vectors on the other three angular points can be computed in a similar manner.

The differential formula for the tangent vector and torsion vector on the boundary can be formed according to the imbedding boundary condition and exterior extent topological methods mentioned in reference [1]. We will not go into greater detail here.

The interpolation accuracy of interpolation formula (8) is higher than that of formula (7). Formula (7) only guarantees the continuance of the positions on the adjacent surface boundaries; the boundary slope is not continuous and shows a surface bending; the adjacent curved surface boundary line is also not continuous in the tangent vector on the angular point and shows a curved surface inflection thus forming a space broken line. However, formula (8) not only guarantees the continuance of the position on the adjacent curved surface boundary but also ensures the tangent vector continuance of the boundary slope and boundary line on the angular points.

#### IV. The Differential Scheme and Boundary Conditions

The differential scheme explained by the mixed differential of a non-linear mixed partial differential equation must be based on the flow field at subsonic, sonic and supersonic speeds. Then equation (3) can separately choose the different patterns of an ellipsoid, paraboloid and hyperbolic. In order for the differential scheme of the linear hyperbolic type equation to satisfy the Courant-Friedrichs-Lewy stability conditions in the local speed coordinate system, the dependent area of the difference equation must be greater than the dependent area of the differential equation. If we use the center difference on the  $n$  axis and use the upstream one side difference on the  $s$  axis, then the dependent area of the difference equation is necessarily greater than or equal to the dependent area of the differential equation. Also, the stability conditions are always satisfied. The perturbation in the subsonic flow field can be disseminated in every direction and conversely it is also dependent on the points all around the flow field. Therefore, both the  $n$  axis and  $s$  axis use the center difference scheme and are able to exactly describe the physical characteristics of subsonic perturbation.

Taking the  $ij$  nodal point as the basic point, they separately interpolate the step length on the local speed coordinate system as the corresponding speed potential values of  $\phi_1$ ,  $\phi_2$ ,  $\phi_3$  and  $\phi_4$  of  $\Delta$ .

The center difference form is used for the tangent flow field (see fig. 4).

$$\phi_{,,} = \frac{\phi_1 - 2\phi_{ij} + \phi_2}{\Delta^2} + O(\Delta^2) \quad (12)$$

The upstream one side difference form is used for the inner points of the supersonic tangent flow field (see chart 4).

$$\phi_{,,} = \frac{\phi_1 - 2\phi_2 + \phi_{ij}}{\Delta^2} + O(\Delta) \quad (13)$$

The center difference form is always used for the normal flow field (see fig. 4).

$$\phi_{,,} = \frac{\phi_3 - 2\phi_{ij} + \phi_4}{\Delta^2} + O(\Delta^2) \quad (14)$$

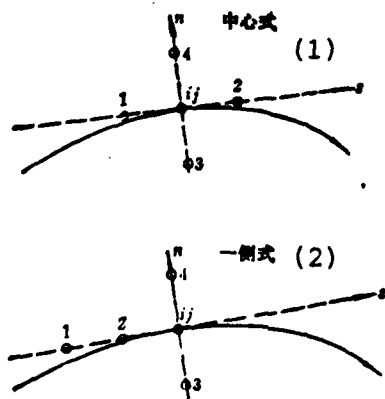


Fig. 4.

Fig. 4. The Difference Scheme for the Inner Points of the Flow Field

Key: 1. Center form  
2. One side form

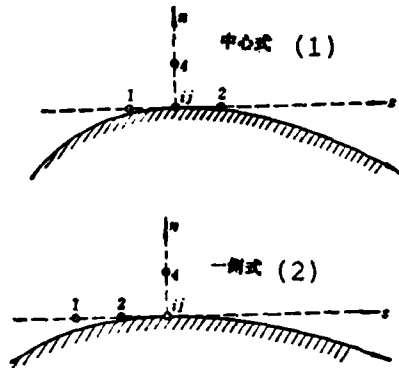


Fig. 5. The Difference Scheme on the Surface of the Body

Key: 1. Center formula  
2. One side formula

The boundary condition for the surface of the body in formula (3) is:

$$\phi_n = 0 \quad (15)$$

Because the boundary line for the surface of the body is a flow line, the speed on the normal surface of the body is naturally 0 and the local speed  $q$  must be in contact tangent with the surface of the body. When the boundary conditions of the surface of the body are imbedded into the normal divalent partial derivative we obtain the difference formula on the surface of the body:

$$\phi_{nn} = -\frac{2}{\Delta^2} (\phi_i - \phi_{ij}) + 0(\Delta) \quad (16)$$

The tangent divalent partial derivatives separately use formulas (12) or (13) based on whether they are subsonic or supersonic.

When this article concretely processed the boundary but had not yet satisfactorily obtained the actual surface of the body, the position was shifted on to the chord line. The tangent direction was still identical to the tangent direction on the surface of the body. That is vector  $s$  on the chord line was parallel to vector  $s^1$  on the surface of the body (see Fig. 6).

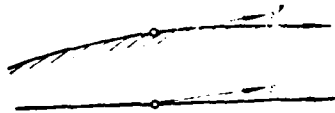


Fig. 6. Simplified Schematic of the Boundary

The local speed  $q$  in the Mach number square represented form always uses the center difference scheme:

$$q = \frac{\phi_2 - \phi_1}{2\Delta} + O(\Delta^2) \quad (17)$$

In the flow field, each point of the local speed  $q$  and the basic coordinate axis included angle  $\theta$  is different. Based on speed components  $u$  and  $v$  in the basic coordinate system we can obtain:

$$\theta = \text{tg}^{-1} \frac{v}{u} \quad (18)$$

In the formula, both  $u$  and  $v$  use the center difference form:

$$\left. \begin{aligned} u &= \frac{\phi_{i,j+1} - \phi_{i,j-1}}{\Delta x_{i-1} + \Delta x_i} + o(\Delta) \\ v &= \frac{\phi_{i,j+1} - \phi_{i,j-1}}{\Delta y_{i-1} + \Delta y_i} + o(\Delta) \end{aligned} \right\} \quad (19)$$

#### V. The Difference Equation and Its Analytical Method

Given that the flow field is subsonic or sonic and supersonic, separating composite formulas (12)-(17), we obtained the mixed difference equation of the flow field.

For the inner points and points on the surface of the body in the subsonic flow field,  $1-M^2 > 0$ .

$$(1-M^2)(\phi_1 - 2\phi_{1j} + \phi_2) + \begin{cases} 2(\phi_4 - \phi_{1j}) = 0 & \text{物面点 (1)} \\ (\phi_3 - 2\phi_{1j} + \phi_4) = 0 & \text{内点 (2)} \end{cases} \quad (20)$$

Key: 1. Points on the surface of the body  
2. Inner points

For the inner points and points on the surface of the body in the supersonic flow field (including the sonic points),  $1-M^2 \leq 0$

$$(1-M^2)(\phi_1 - 2\phi_2 + \phi_{1j}) + \begin{cases} 2(\phi_4 - \phi_{1j}) = 0 & \text{物面点 (1)} \\ (\phi_3 - 2\phi_{1j} + \phi_4) = 0 & \text{内点 (2)} \end{cases} \quad (21)$$

Key: 1. Points on the surface of the body  
2. Inner points

The equation of sonic discriminate difference is:

$$1 - M^2 = 1 - 1 / \left[ \frac{4\Delta^2 q_\infty^2}{(\phi_2 - \phi_1)^2} \left( \frac{\gamma - 1}{2} + \frac{1}{M_\infty^2} \right) - \frac{\gamma - 1}{2} \right] \quad (22)$$

In the formula,  $q_\infty = 1$  and  $\gamma = 1.4$ .

Besides  $\phi_{ij}$ , difference equations (20) and (21) were both obtained by previous field speed potential interpolation. Because of this, we used the point relaxation simple iteration solution. Its formula is differentiated as:

For  $1 - M^2 > 0$ ,

$$\phi_{ij} = \frac{1}{2 - M^2} \left[ (1 - M^2)(\phi_1 + \phi_2) + \begin{cases} 2\phi_3 & \text{物面点 (1)} \\ (\phi_3 + \phi_4) & \text{内点 (2)} \end{cases} \right] \quad (23)$$

Key: 1. Points on the surface of the body  
2. Inner points

For  $1 - M^2 \leq 0$ ,

$$\phi_{ij} = \frac{-1}{1 + M^2} \left[ (1 - M^2)(\phi_1 - 2\phi_2) + \begin{cases} 2\phi_3 & \text{物面点 (1)} \\ (\phi_3 + \phi_4) & \text{内点 (2)} \end{cases} \right] \quad (24)$$

Key: 1. Points on the surface of the body  
2. Inner points

In order to quicken the computation convergence speed, the relaxation operation formula was applied in the relaxation iteration computation process:

$$\phi_{ij}^{(n)} = \omega \bar{\phi}_{ij}^{(n)} + \phi_{ij}^{(n-1)} (1 - \omega) \quad (25)$$

In the formula,  $\bar{\phi}_{ij}^{(n)}$  is the iteration computation result of the n

sequence having not undergone relaxation processing,  $\phi^{(n)}$  and  $\phi^{(n-1)}$  are the iteration computation results of the n sequence and n-1 sequence after having gone through relaxation processing;  $\omega$  is the relaxation factor, its value is determined by requirements and it generally uses  $\omega \leq 2$  but this paper's computations generally takes it as 1.

The computation of the initial field uses the undisturbed homogeneous flow field or the computation result field near the Mach  $\infty$  number. The formula for the undisturbed homogeneous flow field is:

$$\phi_{ii} = q_{\infty} x \quad (26)$$

The distant field boundary speed potential value without exception uses the undisturbed homogeneous flow field value.

The pressure coefficient formula is:

$$\bar{p} = \frac{2}{\gamma M_{\infty}^2} \left\{ \left[ 1 - \frac{(\gamma-1)M_{\infty}^2}{2} (q^2 - q_{\infty}^2) \right]^{\frac{\gamma}{\gamma-1}} - 1 \right\} \quad (27)$$

In the formula, local speed q uses the center difference formula.

## VI. Numerical Illustrations and Their Analysis

This article writes on two numerical illustrations. One is the sharp nosed double arc airfoil and the other is the blunt nosed NACA0015 airfoil. Their relative thicknesses are 0.06 and 0.15 respectively.

The computation was done on the TQ-6 computer which has close to a 1 million time operational speed. Two types of

computation networks were used: the 42x25 and the 82x40 were used to test the effects of different network densities on the computation results and iteration convergences. The computations showed that the different network densities had no effects on computation stability. The figure results of these computations all used the 42x25 network.

The computation results uniformly used two similar wing surfaces with pressure coefficient errors of  $\Delta\bar{p} \leq 0.0001$ . See figs. 7 and 8 for the computation results.

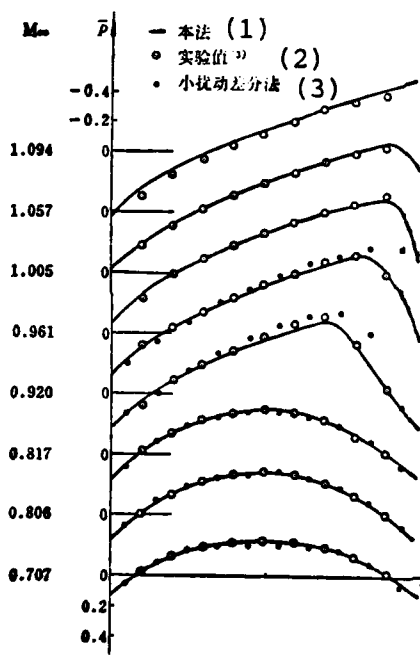


Fig. 7. The Pressure Distribution of the Double Arc Airfoil

Key: 1. Our method  
 2. Test values [3]  
 3. Small disturbed difference method

Fig. 7 appends the test values and small disturbed difference method computation values from reference [3]. The

results in this paper coincide very well with the test values and are actually closer to the test values than the small disturbed difference method.

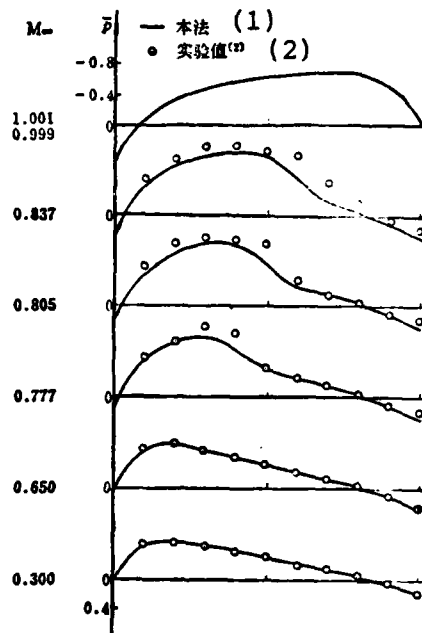


Fig. 8. The Pressure Distribution of the NACA0015 Airfoil  
 Key: 1. Our method  
 2. Test values [2]

Fig. 8 appends the test values from reference [2]. When in a subcritical state, the results of this article coincide very well with the test values. Yet, in a supercritical state, the pressure coefficient computation values are higher than the test values. When at a supercritical state, the airfoil's boundary layer is even larger. This article did not consider the effects of the increased thickness of the boundary layer and therefore the computations tend to be high.

Due to the fact that in the computation process of this paper the stability was very stable there was no acute oscillation divergence. Therefore the computation initial values were uniform for the flow field.

In reference [1] the computation of the  $Mach_{\infty}$  number was close to 1 and therefore the oscillation divergence which used the computation of the initial field was the result field of the above computed  $Mach_{\infty}$  number. Moreover the computed  $Mach_{\infty}$  number increment was very small and  $\Delta M_{\infty} = 0.001$ . That is, with the use of these types of strict measures the computed  $Mach_{\infty}$  number only reached 0.953. Zheng Youwen, one of the writers of recently composed article (1), utilized the zero initial field as well as the control relaxation factor method and computed the NACA0012 blunt nosed airfoil whereupon he only reached  $M_{\infty} = 0.95$ . He also pointed out that up until the present, when using a precise potential flow equation to compute the NACA0012 airfoil, after  $M_{\infty} > 0.9$ , the computations were divergent and no convergent computation results were obtained. Nevertheless, this article obtained convergent computation results for the NACA0015 and double arc airfoil when  $Mach_{\infty}$  was close to 1 as well as corresponding  $Mach_{\infty}$  numbers of 0.999 and 1.001 (the results for the double arc airfoil are not shown in chart 7). Numerically, the two  $Mach_{\infty}$  computation results are almost identical and thus we have overcome the difficulty of computing the  $Mach_{\infty}$  near 1.

## VII. Conclusion

This method is applicable for subsonic, transonic and supersonic flows.

The computation accuracy of this method is higher than the mixed differential method for transonic small disturbed potential flow. Because the equation is a hypothesis for small undisturbed perturbation, with the expansion of the computation's

application range, we can compute the large perturbation flow field of a blunt nosed body.

#### References

1. Luo Shijun, Zheng Youwen and Wang Dieqian, Mixed Differential Method for Transonic Constant Potential Flow, National Defense Industry Publishing House, 1979.
2. Donald, J. G. Gerald, E.N. & Robert, N.D., A Systematic Investigation of Pressure Distribution at High Speeds over Five Representative NACA Low-Drag and Conventional Airfoil Sections, NACA TR832, 1945.
3. Knechtel, E.D. Experimental Investigation at Transonic Speeds of Pressure Distributions over Wedge and Circular-Arc Airfoil Section and Evaluation of Perforated-Wall Interference, NASA TND-15, 1959.
4. Murman, E.M. & Cole, J.D., Calculation of Plane Steady Transonic Flows, AIAA J. Vol 9, No.1, (1971)114~121.
5. Bailey, F.R., On The Computation of Two-and Three-Dimensional Steady Transonic Flows by Relaxation Methods, Lecture Notes in Phy.41(1975)1~77.
6. Jameson, A., Iterative Solution of Transonic Flow over Airfoils and Wings, Including Flow at Mach 1. Comm. on Pure and Applied Math.27(1974)283~309.
7. Coons, S.A., Surface for Computer-Aided Design of Space Forms. AD-663504, 1967.

AN INTERPOLATION MIXED DIFFERENTIAL  
METHOD FOR TRANSONIC LARGE DISTURBED  
SYMMETRICAL POTENTIAL FLOW AROUND  
AIRFOIL

*Ling Heyao*

*(Design Department of Hong An Aircraft Company)*

**Abstract**

By extending an interpolation mixed differential method for transonic small disturbed steady potential flow to the transonic large disturbed steady potential flow, we proposed an interpolation mixed differential method for solution of the exact equation for transonic potential flows in the local speed coordinate system. In numerical illustration of this method the pressure distributions of double arc airfoil and NACA0015 airfoil in symmetrical state are computed and compared with the data of experiments<sup>(2,3)</sup> and the results of the computation for the double arc airfoil by the small disturbed mixed differential method. The comparisons are shown in a good approximation, therefore it is proved that the interpolation mixed differential scheme is stable and convergent. This paper has found a way out of the difficulty at Mach number near 1.

THE CALCULATION OF LIFT AND DRAG CHARACTERISTICS OF SUBSONIC WINGS WITH WINGLETS

by Zhou Renliang  
(Nanjing Aeronautical Institute)

Abstract

This paper uses the finite fundamental solution to divide the spanwise lattice and determine the spanwise locations of control points by means of the constant roll-angle method. We calculated the lifts of rectangular wings with different winglets at subsonic speeds and calculated the induced drags by using the combined flow field method. From the calculations of various configurations of a winglet, we have found out some rules affecting the lift and drag characteristics of wings and picked out a favorable configuration from them. The mechanism of winglets is also analyzed.

Symbols

$\Delta\theta$	Degree of constant roll-angle
$\theta$	The included angle of the roll-angle ray and y axis
$M$	Total number of lines of the lattice
$N$	Total number of rows of the lattice
$s$	Line series number of the lattice
$b$	Wing chord length
$l$	Wing semispan length
$\delta$	Winglet angle
$\alpha$	Wing attack angle
$S$	Wing area
$\lambda$	Wing aspect ratio
$\Delta S$	Lattice area
$\Gamma$	Circulation coefficient
$\Delta C_p$	Load coefficient
$D$	Normal induced speed on wing
$V_\infty$	Overtaking flow speed
$C_y$	Wing lift coefficient
$C_{xi}$	Wing induced drag coefficient
$\Delta$	Induced drag factor

## I. Preface

A winglet is an aerodynamic plan with a simple and effective structure as well as a new technology for improved aircraft performance. The winglet which is fitted on the wing can raise the lift coefficient and lower the induced drag coefficient of a subsonic aircraft, thus raising the climbing rate and economizing on cruise fuel consumption. Therefore, at present, the winglet has already been given serious attention in aerodynamic research and by aircraft designers.

Although some articles and test results have been published on winglet research still there have not been very many. Furthermore, there has not been ample theoretical research and aerodynamic mechanism analysis on the winglet.

This paper which employed the finite fundamental solution method recommended in reference [1], the constant roll-angle method to divide the spanwise lattice and to determine the spanwise locations of control points, and the combined flow field method to calculate the induced drag, obtained satisfactory lift and induced drag values. On this foundation, we calculated and compared the lift and drag characteristics for wings with winglets of various configurations. In this way, we found out some rules affecting the aerodynamic layout of the winglet and picked out a favorable configuration from them. We also analyzed the aerodynamic mechanism of the wing's vortex elimination action and reduction of reduced drag by means of the circulation distribution chart and distribution chart for the circulation change rate.

## II. Computation Methods

### 1. Calculation of the wing lift coefficient

We used the constant roll-angle method to divide the spanwise lattice and to determine the spanwise locations of control points. The principle of the constant roll-angle method is as follows:

Taking the semispan length  $L$  as the radius, the center of the circle is placed on the coordinate origin to create a  $1/4$  circle and beginning from the  $y$  axis each  $\Delta\theta$  angle is a meridional ray and thus we can obtain a group of meridional rays. The  $\Delta\theta$  angle is determined by the following formula:

$$\Delta\theta = \frac{\pi}{4N} \quad (1)$$

The included angle of each ray and  $y$  axis is  $\theta$ :

$$\theta = K\Delta\theta \quad K=1, 2 \dots 2N \quad (2)$$

When the point of intersection of these rays and the arc are projected on the  $y$  axis,  $K$  is the projection of the odd numbered ray point of intersection on the  $y$  axis. This becomes the spanwise location of control points and  $K$  is the even numbered ray point of intersection on the  $y$  axis which becomes the lattice dividing line. For the chordwise, we used the partitioned lattice and chordwise location of control points taken on the  $1/2$  chord line of the lattice. On the half wing, the common  $M \times N$  lattice becomes a winglet section beginning from a certain row to the wing tip causing it to have the required warp angle and thus forming the unflat surface of a wing tip with a winglet.

On each lattice there is arranged a compressible horse shoe vortex, there is added a chordwise location placed on the advancing edge of the lattice and two free vortex separately follow the overtaking flow from the two ends of the lattice's advancing edge and extend out towards infinity. Each control point satisfies the flow boundary conditions. It can solve the linear algebraic equation and obtain the wing's circulation coefficient  $\gamma_j$  distribution. With the circulation coefficient

distribution, we can obtain the circulation coefficient rate of change of the circulation coefficient along the wingspan. At the same time, we can obtain the  $(\Delta C_p)_j$  from the  $\gamma_j$  and after summation we obtain the wing's  $C_{ylift}$  lift coefficient.

## 2. Calculation of the Wing's Induced Drag Coefficient

If the wing is in  $V_{\infty}$ , then the definite load distribution on the wing can be produced. This type of flow field is called the forward flow field. When similar plane form wings are further located in  $-V_{\infty}$ , if it is able to produce a similar load distribution to the normal flow field then it is called the reverse flow field corresponding to the above mentioned forward flow field. From reference [3] we know that the wing's induced drag of the forward flow field and reverse flow field are equal.

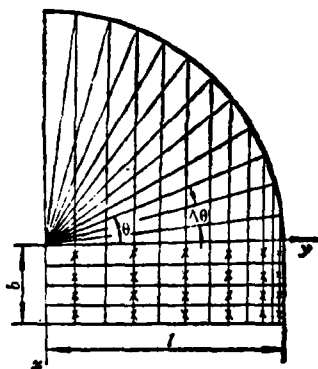


Fig. 1. Lattice Division and Location of Control Point

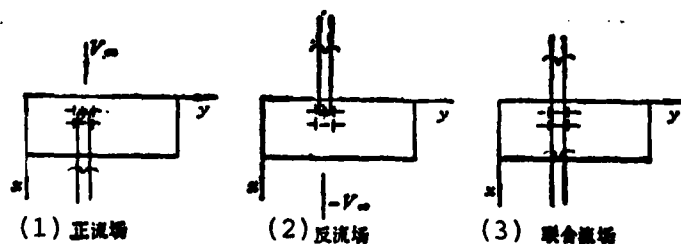


Fig. 2.

Fig. 2. The Forward Flow Field, Reverse Flow Field and Combined Flow Field

- Key: 1. Forward Flow Field  
 2. Reverse Flow Field  
 3. Combined Flow Field

The combined flow field is the superposition of the forward flow field and reverse flow field. In the combined flow field, because the directions of the forward flow field and reverse flow field appended horse shoe vortex in the lattice are opposite, they counteract each other. Only the two free vortex extending into infinity are left in front and in back. At this time, the calculation of the wing's downwash speed only requires the calculation of the produced effects of the free vortex. The induced drag of the wing in the combined flow field is twice that when it is either in forward flow or reverse flow. Therefore, the calculated induced drag must be decreased by half.

In the combined flow field, the circulation coefficient of each lattice free vortex is a known value which is the  $\gamma_j$  in the advancing forward flow field. With the circulation coefficient distribution, we can obtain the normal wash  $D_j$  of the entire free vortex in each control point location. After the summation of each lattice, we obtained the induced drag coefficient of the wing:

$$C_{xi} = \frac{1}{2SV_\infty} \sum_{j=1}^{M \times N} (\Delta C_p)_j D_j (\Delta S)_j \quad (3)$$

$(\Delta C_p)_j$  is the load coefficient in the positive flow field and is a known value.

If the relative value of  $\Delta$  is taken to indicate the  $C_{xj}$ , the induced drag form factor is:

$$\Delta = \frac{C_{L1}}{\left(\frac{C_y^2}{\pi\lambda}\right)} \quad (4)$$

### 3. Analysis of the Calculation Method

In order to test the applicability of the calculation method, we calculated the  $\Delta$  values of four types of rectangular wings with different aspect ratios and compared them with the values of reference [4]. The comparative values are listed in table 1.

	$\lambda = 2$	$\lambda = 4$	$\lambda = 6$	$\lambda = 10$
(1) $\Delta$ (本文)	1.00085	1.00623	1.01642	1.04218
(2) $\Delta$ (文献[4])	1.0007	1.0070	1.0160	1.0420

Table 1

Key: 1. This paper  
2. Reference [4]

It can be seen from the comparison in table 1 that the relative accuracy of the theoretical values found in reference [4] are extremely close to the calculation results of this method and that the accuracy is effective and satisfactory. Furthermore, the use of a constant roll-angle to divide the spanwise lattice and a relatively dense wing tip lattice can better reveal the circulation change of the wing tip area. There is not a great change in the wing tip form and the reaction of the  $\Delta$  value is relatively acute. Therefore, when making a comparison we can use this method to calculate the lift and drag characteristics of wings with different winglets.

### III. Discussion of the Calculation Results

In order to economize on calculation time, we calculated 50 lattices on half wings and  $M \times N$  was  $5 \times 10$ . On 709 aircraft, each calculation of the conditions of a winglet took about 5-6 minutes.

At first, we took the measured wings with winglets shown in fig. 3 as calculation examples and calculated the aspect ratio as  $\lambda = 6.375$ . The wing area used was  $S = 2 \times 8 \times 25.5$  and in an  $\alpha = 0.1$  (arc degree) situation the lift and drag characteristics of rectangular wings with different winglets were calculated.

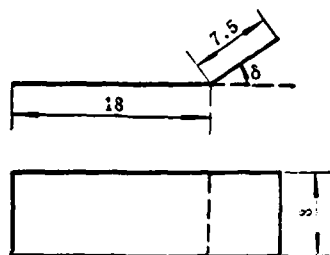


Fig. 3. The Measurements of a Rectangular Wing With a Winglet

#### 1. The Lift and Drag Characteristics of Rectangular Wings With Upward Turning Winglets

When the upward turned angle  $\delta$  on the winglet is  $0^\circ$ ,  $30^\circ$ ,  $45^\circ$ ,  $75^\circ$  and  $90^\circ$ , the calculated wing lift and drag characteristics are as listed in table 2.

$\delta$	$C_y$	$C_{x1}$	$\Delta$
$0^\circ$	0.129548	0.009385	1.018685
$30^\circ$	0.411652	0.009117	1.077522
$45^\circ$	0.386130	0.008574	1.151774
$75^\circ$	0.328177	0.007243	1.346800
$90^\circ$	0.329244	0.007601	1.401237

Table 2

Table 2 The Various  $\delta$  Values of the Lift and Drag Characteristic of Rectangular Wings

It can be seen from table 2 that the larger the  $\delta$  the larger the  $\Delta$  value.  $\Delta$  represents the ratio value of the induced drag and the minimum induced drag. The smaller this value the better the induced drag characteristic and the closer to the minimum induced drag. Therefore, the comparison of the  $\delta \neq 0^\circ$  rectangular wing and  $\delta = 0^\circ$  condition not only causes the block type winglet upward turning to be able to decrease the actual span length of the rectangular wing but the induced drag characteristic can also have some advantages. The greater the upward turning angle the greater the difference of the induced drag characteristic.

In order to analyze the reasons, we drew fig. 4 with the  $\gamma$  and  $\frac{d\gamma}{dy}$  of two rectangular wings being  $\delta = 0^\circ$  and  $\delta = 75^\circ$  for

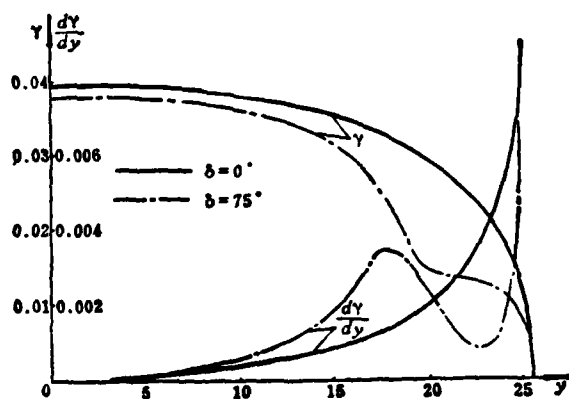


Fig. 4. The  $\gamma$  and  $\frac{d\gamma}{dy}$  Distribution of Rectangular Wings of  $\delta = 0^\circ$  and  $\delta = 75^\circ$

It can be seen from fig. 4 that the  $\gamma$  distribution of  $\delta = 0^\circ$  is relatively close to elliptical distribution and the  $\gamma$  value of the  $\gamma$  distribution of  $\delta = 75^\circ$  in the vicinity of the of the wing and winglet boundary line has a sudden drop. Moreover, the  $\gamma$  values in each location were all smaller than the value when  $\delta = 0^\circ$ . Therefore, the  $C_y$  value of the  $\delta = 75^\circ$  was smaller than when the value was  $\delta = 0^\circ$ . Because the  $\gamma$  distributions are different, their  $\frac{d\gamma}{dy}$  value the stronger the exerted vortex. When  $\delta = 0^\circ$ , there is a strong exerted vortex on the wing tip and when  $\delta = 75^\circ$  there is not only a strong exerted vortex on the wing tip of the winglet but there is also a swelling of the  $\frac{d\gamma}{dy}$  in the vicinity of the winglet's and wing's boundary line. There is also a relatively strong exerted vortex at this location. This then increases the induced downwash on the wing and furthermore causes the spoilage of the induced drag characteristics.

## 2. The Lift and Drag of Rectangular Wings With Patterned Winglets

As regards the lift and drag characteristics of rectangular wings with upward turned winglets discussed above, the winglet is a whole flat plate. If we equally divide the winglet into five horizontal narrow lines chordwise, when each line has a different upward turned angle, then a type of patterned winglet is formed. Starting calculation from the leading edge the upward turned angle of each narrow line on the winglet is  $\delta_1$ ,  $\delta_2$ ,  $\delta_3$ ,  $\delta_4$ , and  $\delta_5$ . The results of the calculations of the lift and drag characteristics of rectangular wings with various patterned winglets are listed in table 3.

N <sub>o</sub>	( $\delta_1, \delta_2, \delta_3, \delta_4, \delta_5$ )	$C_y$	$C_{xi}$	$\Delta$
①	(0°, 0°, 0°, 0°, 0°)	0.429548	0.009385	1.018065
②	(-50°, -50°, 70°, 70°, 70°)	0.453810	0.012075	1.174282
③	(70°, 70°, 70°, -50°, -50°)	0.447306	0.011373	1.138361
④	(0°, 20°, 40°, 60°, 80°)	0.521052	0.015679	1.156575
⑤	(80°, 60°, 40°, 20°, 0°)	0.429515	0.008649	0.938963
⑥	(60°, 45°, 30°, 15°, 0°)	0.445285	0.009315	0.940880
⑦	(0°, 15°, 30°, 45°, 0°)	0.491092	0.011530	0.957503
⑧	(0°, 45°, 30°, 15°, 0°)	0.455304	0.009211	0.889895
⑨	(0°, 60°, 40°, 20°, 0°)	0.452066	0.009135	0.895231
⑩	(0°, 75°, 50°, 25°, 0°)	0.448295	0.015583	1.552973
⑪	(0°, 30°, 20°, 10°, 0°)	0.453312	0.009279	0.904366
⑫	(0°, 45°, 35°, 25°, 15°)	0.445599	0.008798	0.887387
⑬	(0°, 30°, 0°, 30°, 0°)	0.455909	0.009768	0.941150
⑭	(30°, 15°, 0°, 30°, 15°)	0.449585	0.009848	0.975789
⑮	(20°, 0°, 20°, 0°, 20°)	0.449668	0.009740	0.964855

Table 3 The Lift and Drag Characteristics of Rectangular Wings With Various Patterned Winglets

From table 3 we can conclude the following few points:

(1) Plan ① is a rectangular wing of  $\delta^0 = 0^\circ$  and we took it as the criterion state for comparison. If the wing tip section is divided into a patterned wing tip, although this can fundamentally raise the  $C_y$  value, yet some of the  $\Delta$  values have large changes while some change only slightly.

(2) Yet there is the possibility of the patterned winglet causing  $\Delta < 1$  for the rectangular wing and the winglet can also cause its induced drag to be smaller than the minimum induced drag value of the rectangular wing with an aspect ratio of  $\lambda = 6.375$ .

Therefore, the rectangular wings with patterned winglets are different from rectangular wings with upward turned winglets. We can clearly improve the induced drag characteristics of the rectangular wings by manifesting the superiority of rectangular

wings with patterned winglets.

(3) By comparing the 15 plane listed in table 3 we can see that the  $\Delta$  in plan ⑧ ( $0^\circ$ ,  $45^\circ$ ,  $30^\circ$ ,  $15^\circ$  and  $0^\circ$ ) and plan ⑫ ( $0^\circ$ ,  $45^\circ$ ,  $35^\circ$ ,  $25^\circ$ ,  $15^\circ$ ) are relatively small and their  $C_y$  values are larger than those of plan ①. Therefore, as for improving the lift and drag characteristics, they are good plans worthy of recommendation. In order to analyze the mechanism of the patterned winglet being able to improve the lift and drag characteristics of the wing, each line of the  $\gamma$  distribution for plans ① and ⑧ are drawn in fig. 5 and each line of the  $\frac{dy}{dy}$  distribution for plan ⑧ is drawn in fig. 6.

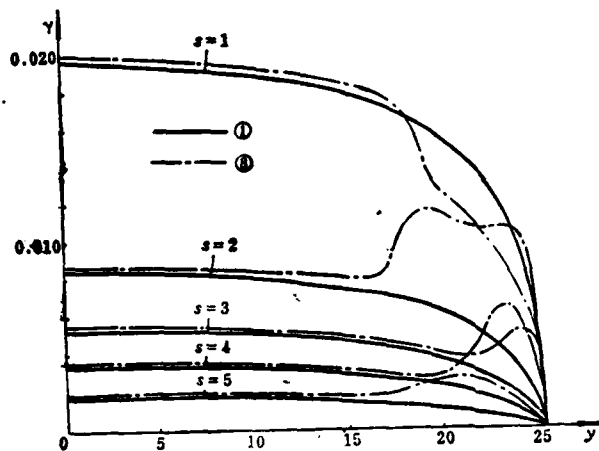


Fig. 5. The  $\gamma$  Distribution for Each Line of the Rectangular Wing in Plans ① and ⑧.

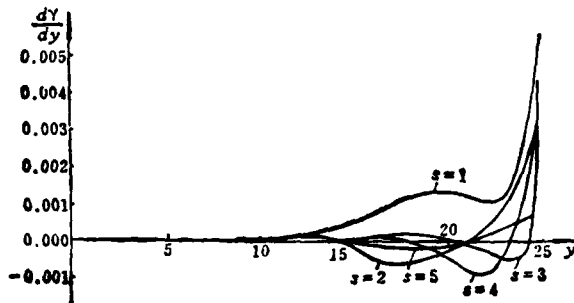


Fig. 6. The  $\frac{dy}{dy}$  Distribution for Each Line of the Rectangular Wing in Plan ⑧

It can be seen from fig. 5 that each line of the  $y$  distribution in plans ① and ⑧ are noticeably different. For the  $y$  values in plan ⑧, besides the winglet section having a sudden drop smaller than plan ①, the  $y$  values of  $s=2,3,4,5$  are all greater than plan ①. There is relatively large swelling in the winglet section and therefore the  $C_y$  value of plan ⑧ is greater than the value of plan ①. Each line of the  $y$  distribution in plan ① is progressively decreasing and therefore each line only has the  $\frac{dy}{dy}$  maximum value in the wing tip area. However, there is a relatively strong exerted vortex on the wing tip. The  $\frac{dy}{dy}$  of plan ⑧ are all negative values in the four lines of  $s=2,3,4,5$  and moreover the minimum value point of the existing  $\frac{dy}{dy}$  is shown at these points to have a relatively strong reverse exerted vortex. The reverse exerted vortex produces induced upwash on the wing and thus causes a decrease of the induced drag.

It can clearly be seen from fig. 6 that plan ⑧ still has a positive  $\frac{dy}{dy}$  maximum value in each line of the pointed end of the winglet yet because the  $s=2,3,4$  lines of the winglet turn upwards one degree these forward exerted vortex are not again in the  $x-y$  plane but shift a distance in the  $z$  direction. This

also decreased the z direction induced downwash weight on the wing and was partially favorable to decreasing the induced drag.

In order to further observe the wing tip exerted vortex of plan ⑧ we drew schematic fig. 7.



Fig. 7. Schematic Chart of the Wing's Wing Tip Exerted Vortex of Plan ⑧

It can be seen from the chart that in the wing's wing tip and its vicinity there not only appears a relatively strong forward exerted vortex but there also appears a relatively strong reverse exerted vortex. At the same time, the winglet has dispersion and upwards shift of the vortex. Therefore, the winglet in plan ⑧ has noticeable vortex elimination and is able to improve the induced drag characteristics of the wing.

### 3. The Lift and Drag Characteristic of Upward Turning and Downward Turning Winglets

In order to compare the effects of the upward turning and downward turning of winglets on the lift and drag characteristics of wings we made the following few group plan comparative calculations (see table 4).

№	( $\delta_1, \delta_2, \delta_3, \delta_4, \delta_5$ )	( $\delta_1, \delta_2, \delta_3, \delta_4, \delta_5$ )
①	(30°, 30°, 30°, 30°, 30°)	(-30°, -30°, -30°, -30°, -30°)
②	(75°, 75°, 75°, 75°, 75°)	(-75°, -75°, -75°, -75°, -75°)
③	(80°, 60°, 40°, 20°, 0°)	(-80°, -60°, -40°, -20°, 0°)
④	(0°, 20°, 40°, 60°, 80°)	(0°, -20°, -40°, -60°, -80°)
⑤	(0°, 15°, 30°, 45°, 0°)	(0°, -15°, -30°, -45°, 0°)
⑥	(0°, -45°, -35°, 25°, 15°)	(0°, 15°, 35°, -25°, -15°)

Table 4 Comparative Plan of the Upward Turning and Downward Turning of the Winglet

Results showed that the calculated  $C_y$ ,  $C_{xj}$  and  $\Delta$  values of the upward turning plan and downward turning plan were totally identical. This explained that only if there was symmetrical upward turning then the lift and drag characteristics would be identical to the upward turning. It can be seen from table 4 that the combined upward and downward turning of the wing tip only needed an unchanging turning angle increase or decrease. At the same time, the included angle adjacent to the winglet does not change so that its lift and drag characteristics also do not change.

#### 4. The Induced Drag Characteristics of Different Sized Winglets

The previously calculated lift and drag characteristic values were all concerned with the reference area as the wing area after the winglet was flattened for the  $a=0.1$  (arc degree). Now we will discuss another situation, that is, using the  $\lambda=4.5$  rectangular wing of plan ① as the basic wing. When without a winglet the wing's reference area is  $S=2 \times 8 \times 18$ . If different sized and different patterned winglets are added on

to this basic wing and use plans ②, ③, ④ and ⑤, although the lengths of each of the added winglets of these four plans is different yet their actual projections on the half wingspan length on the y axis are all close to 20.8 (see fig. 8).

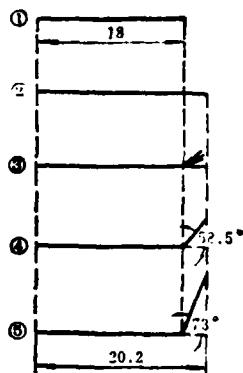


Fig. 8. The Plan of Different Sized Winglets

If plans ②, ③, ④ and ⑤ all use the reference area of plan ①, their aspect ratios all use  $\lambda = 4.5$  and the same  $C_y$  values of plan ① are comparable to their  $C_{xj}$  values. This then requires that the original lift and drag values of plans ②, ③, ④ and ⑤ be converted into conversion values. The conversion values of each plan are listed in table 5.

№	$(\delta_1, \delta_2, \delta_3, \delta_4, \delta_5)$	小翼长	$\alpha$ (弧度)	$C_y$	$C_{xi}$	$\Delta$	$\Delta C_{xi}(\%)$
		(1) (厘米)	(2)				
①	$(0^\circ, 0^\circ, 0^\circ, 0^\circ, 0^\circ)$	0	0.1	0.379347	0.010265	1.008454	0
②	$(0^\circ, 0^\circ, 0^\circ, 0^\circ, 0^\circ)$	2.2	0.085214	0.379347	0.008172	0.802918	20.3818
③	$(0^\circ, 45^\circ, 30^\circ, 15^\circ, 0^\circ)$	2.2	0.081428	0.379347	0.007865	0.77273	23.3719
④	$(58.5^\circ, 58.5^\circ, 58.5^\circ, 58.5^\circ, 58.5^\circ)$	4.2	0.081335	0.379347	0.007675	0.75404	25.2282
⑤	$(73^\circ, 73^\circ, 73^\circ, 73^\circ, 73^\circ)$	7.5	0.083632	0.379347	0.006755	0.663623	34.1941

Table 5 The Conversion Values of Each Plan

Key: 1. Winglet length (centimeters)  
2.  $\alpha$  (arc degree)

It can be seen from the comparison in table 5 that:

(1) The added 2.2 length of patterned winglet plan ③ has a 23.37% decrease in induced drag as compared to plan ① which does not add a winglet. This is better than the aspect ratio of plan ② which has an induced drag decrease of 20.38%.

(2) The 7.5 added length simple upward turning winglet plan ⑤ reduced the induced drag by 34.19% more than plan ① and is better than plans ②, ③ and ④. Although these plans have the most decreases in induced drag yet the winglets' measurements are large, are heavy in weight and the winglets' y direction lateral force can greater enlarge the bending moment of the wing root. When selecting plans, we should synthesize each aspect's good and bad points and make the choice by means of an overall comparison.

#### References

1. An Jiguang, The Problem of the Spanwise Locations of Control Points and Induced Drag in the Finite Fundamental Solution Calculation Method for Subsonic Wings, Journal 7210, 1977-1.
2. Raghuveera padakannaya, Effect of wing tip configuration on the strength and position of a rolled-up vortex, NASA CR 66916.
3. Robert T. Jones and Doris Cohen, Aerodynamic Components of Aircraft at High Speeds, 1957 P52-56.
4. Aerodynamics of Wings and aerofoil sections subsonic lift-dependent drag due to the trailing vortex wake for wings without camber or twist, Engineering sciences data 74035.

THE CALCULATION OF LIFT AND DRAG  
CHARACTERISTICS OF SUBSONIC WINGS WITH  
WINGLETS

*Zhou Renliang*

*(Nanjing Aeronautical Institute)*

**Abstract**

In order to calculate the lifts of rectangular wings with different winglets at subsonic speeds, we have adopted the finite element method which divides spanwise lattice and determines spanwise locations of control points by means of a constant roll-angle method. The induced drags are also calculated by using combined flow field method.

As the results of calculating various configuration of a winglet, we have found out some rules affecting the lift and drag characteristics of wings with winglets and picked out a favourable configuration from them. The aerodynamic mechanism of winglets is also discussed.

A NEW MODEL FOR PREDICTING OVERLOAD RETARDATION EFFECT IN  
FATIGUE CRACK PROPAGATION

by He Qingzhi

(Beijing Institute of Aeronautics and Astronautics)

Abstract

Based on the concept of effective residual compressive stress and considering the residual compressive stress relaxation in basic circulation, we calculated a formula for the propagation speed of cracks after overload:

$$\left(\frac{da}{dN}\right)_t = u^n \left(\frac{da}{dN}\right)_0$$

In the formula,  $\left(\frac{da}{dN}\right)_0$  is the propagation speed of cracks without the effects of overload;  $u = 1 + (1-a) \lambda - (1-a) \times \frac{\Delta K_{\text{res}}}{\Delta K_b}$ ; the stress relaxation coefficient is:

$$u = 1 - \frac{1 - \frac{\Delta K_{\text{res}}}{\Delta K_b}}{r_s - 1}$$

The method in this paper was used to calculate some specimens of LY12, 2024, 7075 aluminum alloys, Ti-6Al-4V titanium alloy and a stiffened plate under different loading conditions. By putting in the coefficient  $n=4$ , we discovered that the calculated results were in good agreement with the test results.

## I. Preface

Given an alternating circulation loading component, after exerting single or multiple high peak loads (overload), the crack propagation speed decreases noticeably, after a period of circulation, the crack propagation speed then gradually returns to normal. Fig. 1 (a) shows loading conditions and fig. 1 (b) is a schematic chart showing the crack propagation characteristic points after overloading. The above mentioned phenomenon was previously given attention and a great deal of research work was carried out. [1-6] Many theories were proposed to clarify the physical quality of this phenomenon. Among them, the most notable are the theory of the residual compressive stress in the plastic zone [1, 3] and the crack closure theory [9]. Wheeler [7] and Willenborg [8] separately proposed models for calculating the retardation period. These models which were used to estimate the load spectrum of the retardation period under loading were relatively successful, yet they did not predict the retardation effects of single overload very satisfactorily.

This paper uses the concept of effective residual compressive stress to propose a new model which can accurately predict the retardation effects after a single elongated overload.

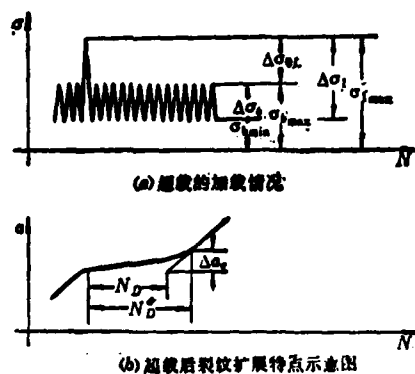


Fig. 1.

Fig. 1.

- Key: (a) Loading conditions of overload  
(b) Schematic chart of the crack propagation characteristic points after overloading

## II. Model and Calculation Formula

After a single elongated overload, there is residual compressive stress in the plastic zone produced by the overload. Based on the hypothesis found in reference [8], this compressive stress is equivalent to an externally added compressive stress  $\sigma_r$  on the specimen:

$$\sigma_r = \sigma_{ap} - \sigma_{bmax} \quad (1)$$

In the formula,  $\sigma_{ap}$  is the circulation stress peak value required for this instantaneously caused retardation effect loss. Its value is:

$$\sigma_{ap} = \frac{\sigma_{y1} \sqrt{C\pi} \sqrt{R_{y1} - \Delta a}}{Y(a)} \quad (2)$$

See the appendix for the deduction of formula (2) and for the definitions of each of the symbols.

Taking the hypothesis a step further, in basic circulation (low load circulation) when the stress drops from the peak value  $\sigma_{bmax}$  to the valley  $\sigma_{bmin}$ , there are changes in the stress field of the crack tips. At the same time, the crack propagates forward a micro- $\delta a$  and there is local relaxation of the residual compressive stress in the overload plastic zone; because of this, the equivalent externally added compressive stress also decreases,

that is, it drops from  $\sigma_r$  to  $a\sigma_r$ . It is

$$\begin{aligned} (\sigma_r)_{\max} &= \sigma_{sp} - \sigma_{b\max} \\ (\sigma_r)_{\min} &= a(\sigma_{sp} - \sigma_{b\max}) \end{aligned} \quad (3)$$

In the formula,  $a$  is the compressive stress relaxation coefficient whose value will be determined below.

Because of the action of an equivalent residual compressive stress, the peak value load and valley load effective values of the basic circulation (see chart 1(a)) are separately:

$$\begin{aligned} (\sigma_{b\max})_{eff} &= \sigma_{b\max} - \sigma_r \\ (\sigma_{b\min})_{eff} &= \sigma_{b\min} - a\sigma_r \end{aligned} \quad (4)$$

We can obtain the effective stress amplitude value from formulas (3) and (4):

$$(\Delta\sigma_b)_{eff} = (\sigma_{b\max})_{eff} - (\sigma_{b\min})_{eff} = \Delta\sigma_b - (1-a)(\sigma_{sp} - \sigma_{b\max}) \quad (5)$$

In the formula,  $\Delta\sigma_b = \sigma_{b\max} - \sigma_{b\min}$ . Formula (5) can also be written as:

$$(\Delta K_b)_{eff} = \Delta K_b - (1-a)(K_{sp} - K_{b\max}) \quad (6)$$

In the formula:  $(\Delta K_b)_{eff} = Y(a)(\Delta\sigma_b)_{eff}$

$$\Delta K_b = Y(a)\Delta\sigma_b$$

$$K_{sp} = Y(a)\sigma_{sp}$$

$$K_{b\max} = Y(a)\sigma_{b\max}$$

$Y(a)$  is the coefficient of the crack's characteristic length  $a$  and the geometrical shape of the component.

When the two ends of formula (6) are divided by  $\Delta K_b$ , we obtain:

$$u = \frac{(\Delta K_b)_{eff}}{\Delta K_b} = 1 + (1 - \alpha) \lambda - (1 - \alpha) \frac{K_{ap}}{\Delta K_b} \quad (7)$$

In the formula:

$$\lambda = \frac{K_{bmax}}{\Delta K_b} = \frac{1}{1 - R}, \text{ 及 } R = \frac{\sigma_{bmin}}{\sigma_{bmax}} = \frac{K_{bmin}}{K_{bmax}} \text{ 为应力比。 (1)}$$

1. is the stress ratio

It is very easy to prove that when  $u \ll 1$ ,  $u$  is the reduced coefficient of the stress strength factor amplitude value after overload.

Formula (7) can be written as:

$$(\Delta K_b)_{eff} = u \Delta K_b \quad (8)$$

If the crack propagation rate is expressed by the Paris formula, then

$$\frac{da}{dN} = C_1 (\Delta K)^n$$

It can be seen that the effective value  $(\Delta K_b)_{eff} = u(\Delta K_b) \ll \Delta K_b$  of the crack propagation's stress strength factor amplitude is caused after overload and therefore the cracking propagation speed will decrease after overload.

Below we will seek the compressive stress relaxation coefficient  $\alpha$ .

It can be seen from formula (22) that when  $\Delta \alpha = 0$  (that is, just after overload),  $K_{ap}$  has a maximum value.

$$(K_{ap})_{max} = \sigma_{y1} \sqrt{C_1} \sqrt{R_{y1}} = K_{1max} \quad (9)$$

We know from formula (6) that at this time  $(\Delta K_b)_{\text{eff}}$  has a minimum value

$$\begin{aligned} (\Delta K_b)_{\text{eff min}} &= \Delta K_b - (1 - \alpha)(K_{1\text{max}} - K_{b\text{max}}) \\ &= \Delta K_b(1 - (1 - \alpha)(r - 1)) \end{aligned} \quad (10)$$

In the formula,  $r = \frac{\Delta \sigma_1}{\Delta \sigma_b} = \frac{\Delta K_1}{\Delta K_b}$  is the overload ratio<sup>F.N.1</sup>.

Many tests have proved that when overload ratio  $r$  is greater than a certain critical value  $r_c$  (the  $r$  value is related to the data and stress ratio  $R$ ; further, it increases in accordance with the increases of  $R$ ), crack propagation will be completely retarded [17,18]<sup>(F.N.1)</sup>. At this time,

$$(\Delta K_b)_{\text{eff min}} = \Delta K_b(1 - (1 - \alpha)(r_c - 1))$$

F.N.1: In references [17] and [18] the overload ratio is defined as  $r' = \frac{K_{1\text{max}}}{K_{b\text{max}}}$ . Naturally, between  $r$  and  $r'$  there is the following relationship,  $r = \frac{r' - R}{1 - R}$ .

Naturally, if

$$(\Delta K_b)_{eff\ min} \leq \Delta K_{th} \quad (11)$$

crack propagation will be completely retarded;  $\Delta K_{th}$  is the "threshold value" of the fatigue crack propagation. Using the conditions expressed in formula (11), we can obtain:

$$\alpha = 1 - \frac{1 - \frac{\Delta K_{th}}{\Delta K_b}}{r_s - 1} \quad (12)$$

When formula (12) is substituted into formulas (7) and (8), we obtain:

$$(\Delta K_b)_{eff} = \left( 1 + \frac{1 - \frac{\Delta K_{th}}{\Delta K_b}}{r_s - 1} \lambda - \frac{1 - \frac{\Delta K_{th}}{\Delta K_b}}{r_s - 1} \frac{K_{op}}{\Delta K_b} \right) \Delta K_b = u(\Delta K_b) \quad (13)$$

During the retardation period following overload, the crack propagation speed is:

$$\begin{aligned} \left( \frac{da}{dN} \right)_r &= C_1 (\Delta K_b)_{eff}^m, \quad \text{如 } (\Delta K_b)_{eff} > \Delta K_{th} \\ \left( \frac{da}{dN} \right)_r &= 0 \quad (2) \text{ 如 } (\Delta K_b)_{eff} \leq \Delta K_{th} \\ \text{或 (3)} \quad \left( \frac{da}{dN} \right)_r &= u^m \cdot C_1 (\Delta K_b)^m = u^m \left( \frac{da}{dN} \right)_0 \end{aligned} \quad (14)$$

Key: 1. If  
2. If  
3. Or

In the formula,  $\left(\frac{da}{dN}\right)_0$  is the crack propagation speed corresponding to  $\Delta K_b$  without being affected by overload and  $n$  is a coefficient.

Integral formula (14) can obtain the circulation number  $N_D^*$  required to penetrate the overload retardation zone.

$$N_D^* = \int_0^{\Delta a_c} \frac{d\Delta a}{u^n \left(\frac{da}{dN}\right)_0} \quad (15)$$

$\Delta a_c$  is the length of the overload retardation zone and its value can be obtained by putting in  $u = 1$  from formula (7):

$$\Delta a_c = \frac{1}{C\pi\sigma_y} (K_{I_{max}}^2 - K_{I_{min}}^2) \quad (16)$$

The comparison of retardation zone length  $\Delta a_c$  and crack characteristic length  $a$  is very small and when  $\Delta\sigma_b$  is the constant, we can consider the  $\Delta K_b$  and  $\left(\frac{da}{dN}\right)_0$  as the constants. At this time, formula (15) can be written as:

$$N_D^* = \frac{1}{\left(\frac{da}{dN}\right)_0} \int_0^{\Delta a_c} \frac{d\Delta a}{u^n} \quad (17)$$

Below we will study the changes of the crack speed after overload. It can be seen from formulas (7) and (22) that the  $u$  value increases in accordance with the increases of the  $\Delta a$  and when it reaches  $\Delta a = \Delta a_c$ ,  $u = 1$ . The minimum values of  $u$  and  $\left(\frac{da}{dN}\right)$  are:

$$u_{\min} = 1 - (1 - \alpha)(r - 1) \quad (18)$$

and

$$\left(\frac{da}{dN}\right)_{\min} = u_{\min}^n \left(\frac{da}{dN}\right)_0 \quad (19)$$

### III. Results and Discussion of Calculations

Applying the previously deduced formulas, we separately calculated the overload retardation period of some specimens of LY12, 2024-T3, 2024-T351, 7075-T6, 7075-T73 aluminum alloys, Ti-6Al-AV titanium alloy and a stiffened plate under different loading conditions. The  $\Delta K_{th}$  and  $r_c$  data are separately taken from references (12,13,18,19,20).

In the calculations, we used the coefficient  $n = 4$ . The calculation results of  $N_D^*$  are listed in table 1 and the calculation results of  $\left(\frac{da}{dN}\right)_{\min}^D$  are listed in table 2. Both tables list the corresponding test values.

材 料 (1) (厚度毫米)	$\Delta K_b$ $\frac{MN}{m^{\frac{3}{2}}}$	R	超载比 (3) r	$(\frac{da}{dN})_0$ 毫米/周 (4)	$C_D$ (7)	$N_D^*$ (周) (5)		(6) $\frac{\Delta b}{N_D}$ (计算) $N_D$ (实验) (9)
						计算值 (8)	实 验 值	
LY12	9.4	0.1	2.0	$16.5 \times 10^{-6}(11)$	1.0	30000	32000 <sup>(11)</sup>	0.94
(4)	10.2	0.1	2.0	$18.0 \times 10^{-6}(11)$	1.0	33000	36000 <sup>(11)</sup>	0.92
2024-T3 (1.6)	9.0	0.1	1.5	$8.0 \times 10^{-6}(4)$	1.0	3800	7000 <sup>(10)</sup> 8000	0.51
	9.0	0.1	2.0	$8.0 \times 10^{-6}(4)$	1.0	42000	40000 <sup>(10)</sup> 45000	0.99
	15.0	0.1	1.5	$15.0 \times 10^{-6}(10)$	1.0	5400	5000 <sup>(10)</sup>	1.08
	15.0	0.1	2.0	$15.0 \times 10^{-6}(10)$	1.0	124000	120000 <sup>(10)</sup>	1.03
	15.0	0.05	1.5	$15.0 \times 10^{-6}(10)$	1.0	6700	7000 <sup>(10)</sup>	0.96
2024-T3 (3.2)	15.0	0.05	1.5	$29.5 \times 10^{-6}(6)$	1.0	6300	6500 <sup>(6)</sup>	0.97
	16.5	0.286	1.5	$53.0 \times 10^{-6}(6)$	1.0	4600	5000 <sup>(6)</sup>	0.92
	16.5	0.286	2.0	$53.0 \times 10^{-6}(6)$	1.0	50000	46000 <sup>(6)</sup>	1.09
	16.5	0.5	2.0	$80.0 \times 10^{-6}(6)$	1.0	43000	47000 <sup>(6)</sup>	0.92
	19.8	0	1.5	$41.0 \times 10^{-6}(4)$	1.0	4500	8000 <sup>(10)</sup>	0.57
	19.8	0.05	2.0	$41.0 \times 10^{-6}(4)$	1.0	87000	104000 <sup>(10)</sup> 133000	0.74
	23.1	0	1.5	$56.0 \times 10^{-6}(4)$	1.0	9100	9000 <sup>(10)</sup>	1.01
	23.1	0	2.0	$56.0 \times 10^{-6}(4)$	1.0	210000	245000 <sup>(10)</sup>	0.86
2024-T351 (10)	13.1	0.01	2.0	$37.7 \times 10^{-6}(14)$	1.5	22800	20500 <sup>(14)</sup>	1.11
	14.9	0.01	2.0	$40.0 \times 10^{-6}(14)$	1.2	47500	41000 <sup>(14)</sup>	1.15
	18.0	0.01	2.0	$62 \times 10^{-6}(14)$	1.0	52900	53800 <sup>(14)</sup>	0.98
	13.5	0.1	2.0	$32.0 \times 10^{-6}(14)$	1.3	38800	16000 <sup>(14)</sup>	2.4
	15.7	0.1	2.0	$53.2 \times 10^{-6}(14)$	1.1	40600	41600 <sup>(14)</sup>	0.98
	20.2	0.1	2.0	$118 \times 10^{-6}(14)$	1.0	39000	32000 <sup>(14)</sup>	1.2
Ti-6Al-4V (1.6)	14	0	2.0	$7.6 \times 10^{-6}(16)$	1.0	18000	15000 <sup>(21)</sup>	1.2
	14	0	2.36	$7.6 \times 10^{-6}(16)$	1.0	24000	30500 <sup>(21)</sup>	0.8
	14	0	2.40	$7.6 \times 10^{-6}(16)$	1.0	28000	30000 <sup>(21)</sup>	0.93
	16.7	0.1	2.11	$17.8 \times 10^{-6}(16)$	1.0	10300	11200 <sup>(16)</sup>	0.92
	16.7	0.1	1.78	$17.8 \times 10^{-6}(16)$	1.0	8260	8200 <sup>(16)</sup>	1.01
	17.4	0.1	2.11	$22.8 \times 10^{-6}(16)$	1.0	8800	10100 <sup>(16)</sup>	0.88
	25.2	0.1	1.55	$63.0 \times 10^{-6}(16)$	1.0	1650	2400 <sup>(16)</sup>	0.70
	25.8	0.1	1.55	$63.5 \times 10^{-6}(16)$	1.0	1500	2500 <sup>(16)</sup>	0.62
(2) A型加劲板 <sup>(22)</sup> (1.5)	9.6	0.43	2.48	$20.0 \times 10^{-6}(23)$	1.0	73000	6800 <sup>(2)</sup>	1.07
7075-T6 (1.6)	7.32	0.1	2.11	$8.89 \times 10^{-6}(20)$	1.0	12900	12500 <sup>(20)</sup>	1.03
	10.0	0.1	2.11	$20.3 \times 10^{-6}(20)$	1.0	13000	10000 <sup>(20)</sup>	1.3
7075-T73 (1.6)	7.61	0.1	2.11	$6.6 \times 10^{-6}(20)$	1.0	24000	25000 <sup>(20)</sup>	0.96
	10.0	0.1	2.11	$13.72 \times 10^{-6}(20)$	1.0	26900	20000 <sup>(20)</sup>	1.34

(10)<sup>①</sup> 根据参考文献[10]数据推算得到;  
(11)<sup>②</sup> 北航503实验数据。

Table 1

Table 1

- Key: 1. Material (thickness in millimeters)  
 2. A model stiffened plate  
 3. Overload ratio  
 4. Millimeters/cycle  
 5. (Cycles)  
 6. (Calculation)  
 7. Calculated value  
 8. Test value  
 9. Test  
 10. ① Calculation based on data from reference [10]  
 11. ② Data of 503 tests at the Beijing Institute of Aeronautics and Astronautics

材 料 (1) (厚度毫米)	$\Delta K_0$ $MN/m^{3/2}$	R	超载比 (2) r	$(\frac{da}{dN})_{min} / (\frac{da}{dN})_0$ (3) (计算)	$(\frac{da}{dN})_{min} / (\frac{da}{dN})_0$ (4) (实验)①	$(\frac{da}{dN})_{min}$ (计算)(5) $(\frac{da}{dN})_{min}$ (实验)(6)
2024-T351 (10)	13.1	0.01	2.0	2.56%	1.65%	1.55
	14.9	0.01	2.0	2.20%	1.59%	1.38
	18.0	0.01	2.0	1.83%	1.45%	1.26
	13.5	0.1	2.0	2.45%	1.5%	1.55
	15.7	0.1	2.0	2.09%	1.32%	1.58
	20.2	0.1	2.0	1.66%	2.54%	0.66
2024-T3 (3.2)	19.8	0.05	2.0	1.67%	1.5%	1.11

(7)① 数据取自参考文献[14及4]。

Table 2

- Key: 1. Material (thickness in millimeters)  
 2. Overload ratio  
 3. (Calculation)  
 4. (Test)  
 5. (Calculation)  
 6. (Test)  
 7. ① Data taken from references [14] and [4]

The comparison of  $N_D^*$  (calculation) and  $N_D^*$  (test) is shown in fig. 2.

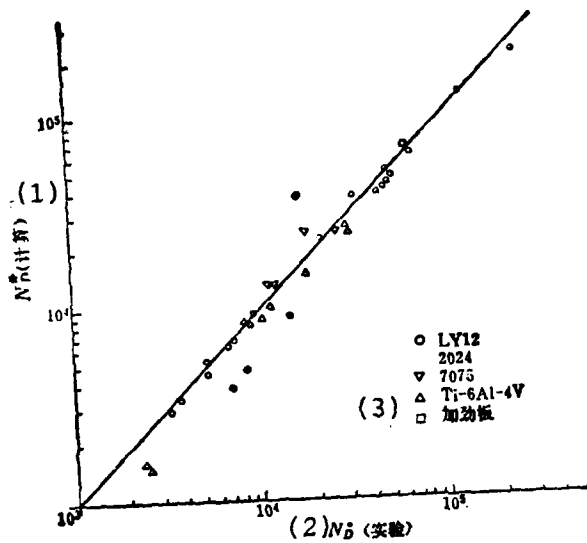


Fig. 2.

Key: 1. (Calculation)  
 2. (Test)  
 3. Stiffened plate

After the above analysis and calculations, we can make the following conclusions:

(1) Coefficient  $n = 4$  can be used for the LY12, 2024, 7075 aluminum alloys and Ti-6Al-4V titanium alloy;

(2) The overload retardation period  $N_D^*$  obtained from the

calculations of the proposed model used in this paper were in good agreement with the test results. When considering the dispersity of the crack propagation speed  $\left(\frac{da}{dN}\right)_0$  and the  $N_D^*$  test data, we found that using the method in this paper to calculate the retardation period was quite satisfactory;

(3) The crack minimum propagation speed  $\left(\frac{da}{dN}\right)_{\min}$  after overload calculated by means of this method was generally slightly greater than the test values. Moreover, when occurring just after overload, this speed was not in agreement with the test results.

#### Appendix

The deduction of formula (2):

Based on the concept proposed in reference [8], we have (see fig. 3):

$$a_1 + R_{y,sp} = a_0 + R_{y_1} \quad (20)$$

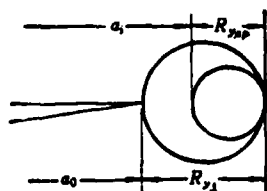


Fig. 3.

In the formula,  $R_{y1} = \frac{1}{C\pi} \left( \frac{K_{1max}}{\sigma_{ys}} \right)^2$  - Plastic zone diameter produced by overload;

$R_{yap} = \frac{1}{C\pi} \left( \frac{K_{ap}}{\sigma_{ys}} \right)^2$  - the plastic zone diameter derived from the added circulation stress peak value  $\sigma_{ap}$  of a certain instantaneous and hypothetically caused overload effect loss;

C - the constant of the Irwin plastic zone

C = 1 is the situation for plane stress;

C = 3 is the situation for plane strain;

C =  $\frac{3}{1+2s}$  is the situation for the combined model, s is the proportion occupied by the inclined fracture on the break fracture (shearing model).

From formula (20):

$$\frac{1}{C\pi} \left( \frac{K_{I,II}}{\sigma_{ys}} \right)^2 = R_{y1} - (a_1 - a_0)$$

If  $\Delta a = a_i - a_o$  is the crack propagation quantity after overload, the

$$K_{op} = \sigma_{op} \sqrt{C\pi} \sqrt{R_{y1} - \Delta a} \quad (21)$$

or

$$\sigma_{op} = \frac{K_{op}}{Y(a)} = \frac{\sigma_{op} \sqrt{C\pi} \sqrt{R_{y1} - \Delta a}}{Y(a)} \quad (22)$$

#### References

- (1) Schijve, J and Broek, D., The Results of Test Programme based on a Gust Spectrum With Variable Amplitude Loading. Aircraft Engineering 1962. p. 314.
- (2) Hudson, C.M. and Hardrath, H.F., Investigation of the Effects of Variable Amplitude loading on Fatigue Crack Propagation Pattern. NASA TN-D-1803 (1963).
- (3) Hudson, C.M. et al, Effects of Changing Stress Amplitude on the Rate of Fatigue Crack Propagation of Two Aluminum Alloys. NASA TN-960 (1961).
- (4) Von Euw, et. al, Delay Effects in Fatigue Crack Propagation. ASTM STP 513 (1972).
- (5) Corbly, D.M., On the Influence of Single and Multiple Peak-load on Fatigue Crack Propagation in 7075-T6511 Aluminum Alloy. Eng. Fract. Mech. (1973).

- (6) Trebule, V.W. Jr. et al, Effect of Multiple Overload on Fatigue Crack Propagation in 2024-T3 Aluminum Alloy ASTM STP 536(1972).
- (7) Wheeler, O.E., Spectrum Loading and Crack Growth. Paper 71-Met-X ASTM (1971).
- (8) Willenborg, J. et al, A Crack Growth Retardation Model Using an Effective Stress Concept AFFDL-TM-71-1 FBR(1971).
- (9) Elbew, W., The Significance of Crack Closure ASTM STP 486(1971).
- (10) Mills, M.J. et al, The Effect of Sheet Thickness on Fatigue Retardation in 2024-T3 Aluminum Alloy. Eng. Fract. Mech. 1975 No. 4.
- (11) Gu Mingda, Zhang Shijie and Yan Minggao: The Effects of Overload on Fatigue Crack Propagation Speed in LY-12 Alloy Plate. Aeronautics Data, no. 6(1979).
- (12) Bathias, C. et al, Mechanism of Overload Effect on Fatigue Crack Propagation in Aluminum Alloy. Eng. Fract. Mech. 1978 No. 2.
- (13) Chen Hu, Cai Qigong et al: Engineering Fracture Mechanics (vol. 1), p. 434.
- (14) Rangunathan, N., et al, A Contribution to the Study of Fatigue Crack Retardation in Vacuum. Eng. Fract. Mech. Vol. 11, No. 4.
- (15) Bucci, B.J. et al, Fatigue Threshold of Crack Propagation in Air and Dry Argon for Ti-6AL-4V Alloy. ASTM STP513.
- (16) Jones, R.E., Fatigue Crack Growth Retardation After Single-cycle Peak Load in Ti-6AL-4V Titanium Alloy. AFML-TR-72-163.
- (17) Probst, E.P. and Hillberry, B.M., Fatigue Crack Delay and Arrest Due to a Single Peak Tensile Overload. AIAA Journal, March, 1974.
- (18) Himmelein, M.K. and Hillberry, B.M., Effect of Stress Ratio and Overload Ratio on Fatigue Delay and Arrest. ASTM STP 590.
- (19) Gray, T.D. and Gallapher, J.P., Predicting Fatigue Crack Retardation Following a Single Overload Using a Modified Wheeler Model. ASTM STP 590.

- (20) Chanani, G.R. Fundamental Investigation of Fatigue Crack Growth Retardation in Aluminum Alloys. AFML-TR-76-156.
- (21) Walker, K., Effects of Environment and Complex Load History of Fatigue Life. ASTM STP462.

# A NEW MODEL FOR PREDICTING OVERLOAD RETARDATION EFFECT IN FATIGUE CRACK PROPAGATION

*He Qingzhi*

*(Beijing Institute of Aeronautics and Astronautics)*

## Abstract

The effect of the residual compressive stress in the overload plastic zone is equivalent to an effective stress  $\sigma_r$ , and as proposed by Willenborg

$$\sigma_r = \sigma_{sp} - \sigma_{b \max}$$

where

$$\sigma_{sp} = \frac{\sigma_{ys} \sqrt{C\pi} \sqrt{R_{y1} - \Delta\sigma}}{Y(a)}$$

In the present paper it is further assumed that  $\sigma_r$  is not constant during one baseline cycle, but it varies from  $\sigma_r$  at  $\sigma_{b \max}$  to  $\alpha\sigma_r$  at  $\sigma_{b \min}$ ,  $\alpha$  is a relaxation factor. Then

$$(\sigma_{b \max})_{eff} = \sigma_{b \max} - \sigma_r$$

$$(\sigma_{b \min})_{eff} = \sigma_{b \min} - \alpha\sigma_r$$

so the effective stress range  $(\Delta\sigma_b)_{eff}$  during the baseline cycle is

$$(\Delta\sigma_b)_{eff} = (\sigma_{b \max})_{eff} - (\sigma_{b \min})_{eff} = \Delta\sigma_b - (1 - \alpha)(\sigma_{sp} - \sigma_{b \max})$$

Or alternatively the above equation may be written in the following form

$$(\Delta K_b)_{eff} = \Delta K_b - (1 - \alpha)(K_{sp} - K_{b \max})$$

It is easy to show that the maximum value of  $K_{sp}$  during the transient period following the overload will be

$$(K_{sp})_{\max} = K_{1 \max} \text{ at } \Delta\sigma = 0, \text{ so}$$

$$(\Delta K_b)_{eff \min} = \Delta K_b [1 - (1 - \alpha)(r - 1)]$$

where the overload ratio  $r = \frac{K_1}{K_b}$ .

Many investigators have found that when the overload rate increases to some critical value  $r_c$ , the crack will cease to propagate at all after the overload. It is reasonable to assume that when  $r$  reaches  $r_c$ ,  $(\Delta K_b)_{eff \min}$  will decrease to a value  $(\Delta K_b)_{eff \min} = \Delta K_{rb}$ , so the crack will cease to propagate. Using this condition, we get

$$\Delta K_b [1 - (1 - \alpha)(r_c - 1)] = \Delta K_{rb}$$

or

$$\alpha = 1 - \frac{1 - \frac{\Delta K_{rb}}{\Delta K_b}}{r_c - 1}$$

If the crack propagation rate is expressed by Paris formula

$$\frac{da}{dN} = C_1 (\Delta K_b)^n$$

then the reduced rate of crack propagation following an overload will be

$$\left(\frac{da}{dN}\right) = C_1 [(\Delta K_b)_{eff}]^n = C_1 (u \Delta K_b)^n = u^n \left(\frac{da}{dN}\right)_0$$

where  $u = \frac{(\Delta K_b)_{eff}}{\Delta K_b} = 1 + (1 - \alpha) \lambda - (1 - \alpha) \frac{K_{op}}{\Delta K_b}$

$$\lambda = \frac{K_{b \max}}{\Delta K_b}$$

$\left(\frac{da}{dN}\right)_0 = C_1 (\Delta K_b)^n$  the unretarded rate of crack propagation corresponding to  $(\Delta K_b)_0$ .

The retarded number of cycle  $N_D^*$  can be calculated by

$$N_D^* = \int_0^{\Delta a} \frac{d\Delta a}{u^n \left(\frac{da}{dN}\right)_0}$$

where  $\Delta a$  is the length of the retarded zone.

The retarded number of cycle of some specimens of LY12, 2024, 7075 aluminium alloys, Ti-6Al-4V titanium alloy and a stiffened plate under different loading conditions are predicted by the present method. By putting the coefficient  $n = 4$ , we find that the agreement between the predicted values and the tested values is good, as shown in fig. 2 of this paper.

J-INTEGRAL EXPERIMENTAL CALIBRATION OF SHEET SPECIMENS WITH  
SINGLE EDGE NOTCH

Lui Ligeng, Chen Xianxi and Cai Qigong  
(Central Iron and Steel Research Institute)

Zheng Minzhung  
(Aircraft Strength Research Institute)

Abstract

The J-integral of a sheet notched specimen has a very simple form when the notched surface has been taken as the integral contour, i.e.

$$J = \int W dy = \int_{-\pi/2}^{\pi/2} W(\theta) \rho \cos\theta d\theta$$

It can be further simplified into:

$$J = A \rho W_0$$

where

$$A = 2 \int_0^{\pi/2} \varphi(\theta) d\theta$$

and

$$\varphi(\theta) = \frac{W'(\theta)}{W_0} \cos \theta$$

For two types of specimens with single edge notch (the notch root curve radius is divided into 20 millimeters and 9 millimeters), this paper determined the strain distribution  $\varepsilon(\theta)$  of the notched surface, then after stress-strain curve was converted to form deformation work density distribution  $W(\theta)$  there was finally numerical integration and we obtained coefficient A. The test results were compared with the linear elasticity fracture mechanics method of Weiss's correction of the plastic zone.

#### I. Preface

When analyzing the strength and predicting the lifespan of the notch specimen, it is necessary for people to determine the relationship between the outer load, specimen and notch geometrical parameters, and the notch root's maximum strain  $\varepsilon_0$ , the maximum stress-strain product  $\varepsilon_0 \sigma_0$  and the maximum deformation work density [1-3]  $W_0 = \int \sigma d\varepsilon$ . It is well known that when the notch root is located in an elastic sphere,  $\varepsilon_0 = K_t \varepsilon_g$ ,  $\varepsilon_0 \sigma_0 = K_t^2 \frac{\sigma_g^2}{E}$  and  $W_0 = \frac{1}{2} \varepsilon_0 \sigma_0 = \frac{1}{2} K_t^2 \frac{\sigma_g^2}{E}$ . In this equation,  $\varepsilon_g$  and  $\sigma_g$  are the distant mean strain and stress, and K is the theoretically elastic concentration coefficient. After the notch root entered into an elastoplastic state, it went through the commonly used Neuber relationship, that is  $K_\varepsilon K_\sigma = K_t^2$ , and obtained

$$\varepsilon_0 \sigma_0 = \varepsilon_t \sigma_t = K_t^2 \frac{\sigma_g^2}{E}$$

Based on the J-integral full quantity theory, in reference [4] Cai Qigong proved that, under the conditions of a hardened

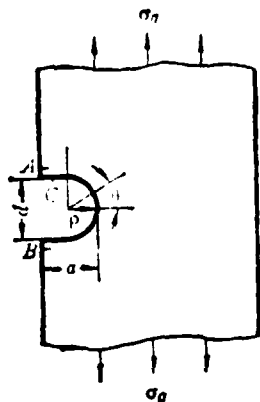
material of an assumed power and when the notch root strain distribution satisfies the  $\xi(\theta) = \xi_0 \cos^m \theta$ , the Neuber relationship is still established under a type I load. He also calculated the A in  $J/\rho = AW_0$  when in the 0.8-1.2 range.

Therefore, after J-integral direct experimental calibration of the notch specimen, we measured the  $\xi(\theta)$  and  $W(\theta)$  and experimentally determined coefficient A. Thus, we used the fracture mechanics parameters to describe the maximum deformation work density W of the notch root.

## II. Specimen and Experimental Method

### 1. Specimen

The specimen was taken from hot rolled sheet of aluminum alloy LY12 with a 50 millimeter thickness of  $\sigma_{0.2} = 11.2$  kilograms/millimeter<sup>2</sup>. The measurements of the sheet specimen with a single edge notch was: length 400 millimeters, width 150 millimeters, thickness 30 millimeters. See fig. 1 for the specimen number and notch measurements.



① 试样号	a	p	d
Q <sub>20a</sub>	10	20	10
Q <sub>20b</sub>	10	20	10
Q <sub>0</sub>	10	9	18

Fig. 1. Measurement of Specimen Notch

Key: 1. Specimen number

The following formula can be used to indicate the stress-strain curve of the measured LY-12.

$$\epsilon = \frac{\sigma}{E} + a\sigma^n \quad (1)$$

In the formula,  $a=3.537 \times 10^{-13}$ ,  $n=9.25$  and  $E=7000$  kilograms/millimeter<sup>2</sup>.

## 2. Test Method

The test was carried out on a 200 ton East German ZDM200TPU type material test machine. The two ends of the specimen were each fixed on a plate with 6 bolts and the plate used dowels to connect the connecting rod to the test machine. In the test, specimen Q<sub>20b</sub> was directly clamped.

There were 1x1 millimeter and 2x3 millimeter resistance strain pieces pasted on the inner surface of the specimen notch. Their model numbers and resistance values were PBJ<sub>1</sub>-A<sub>3</sub> (R=60 ohm) and PBJ<sub>3</sub>-A<sub>3</sub> (R=120 ohm). The resistance strain pieces were separately pasted on the 0°, 10°, 20°, 30°, 45°, 60°, 75° and 90° curvature central arguments of the corresponding notches (see fig. 2.)

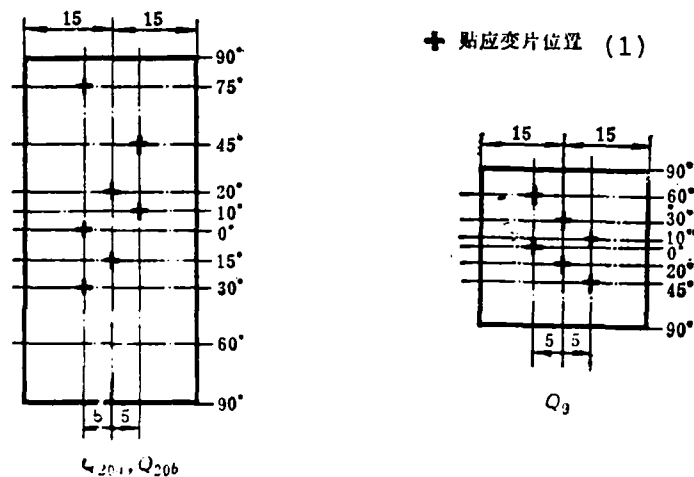


Fig. 2. Developed Distribution Chart of the Strain Piece on the Inner Surface of the Notch

Key: 1. Location of pasted strain piece

At the time of the test, there was gradual loading so as to maintain the load and measure the strain value up until the strain piece lost effectiveness when it reached the maximum strain area at about 9000 microstrain.

### III. Test Results

#### 1. The Strain Distribution of the Notch Root

Figs. 3-5 present the distribution of the strain along the notch surface under different load levels. In two specimens with relatively large curvature radii, there was a strain distribution form similar to: a specimen with a curvature radius of  $p=9$  millimeters had an obvious widening of the strain concentration region.

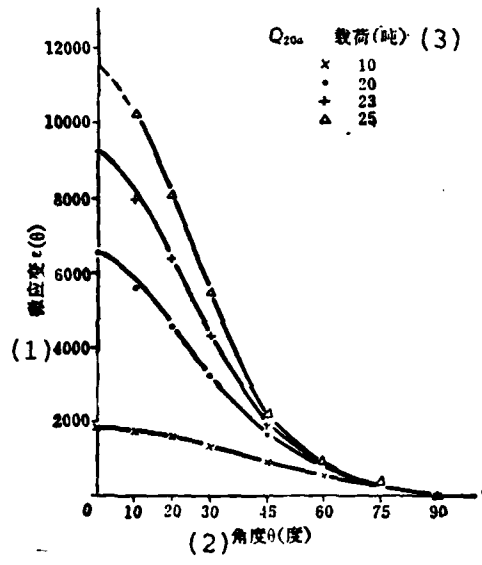


Fig. 3. The Strain Distribution of Specimen Q<sub>20a</sub> Under Different Load Levels

Key: 1. Microstrain (θ)  
 2. Angle θ (degrees)  
 3. Load (tons)

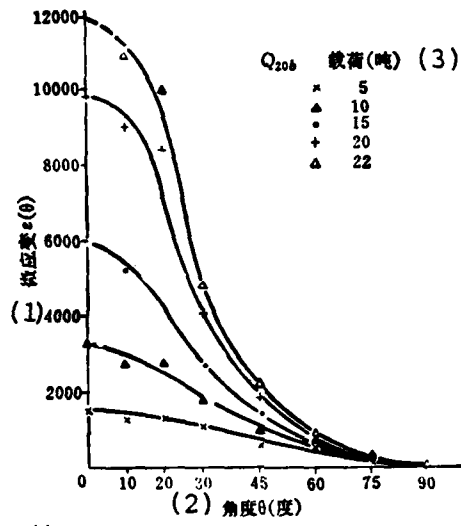


Fig. 4. The Strain Distribution of Specimen  $Q_{20b}$  Under Different Load Levels

Key: 1. Microstrain ( $\theta$ )  
 2. Angle  $\theta$  (degrees)  
 3. Load (tons)

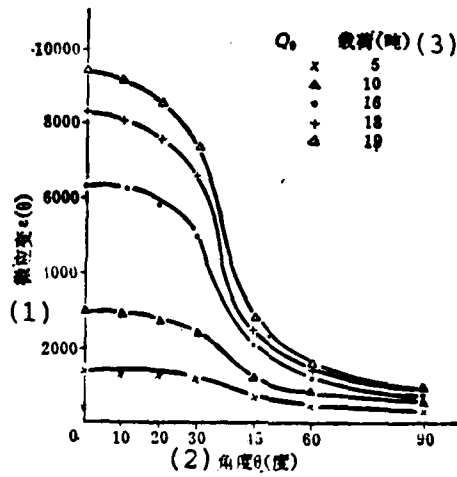


Fig. 5.

Fig. 5. The Strain Distribution of Specimen Q<sub>g</sub> Under Different Load Levels

- Key: 1. Microstrain ( $\theta$ )  
 2. Angle  $\theta$  (degrees)  
 3. Load (tons)

The tests also found that when three specimens were in the  $\theta=90^\circ$  area and the A, B and C areas (see Fig. 1.) on the outer side of the notch, they all appeared in the compressive stress region and the strains were all negative values.

2. The Deformation Work Density Distribution of the Notch Root

The conditions of the plane stress was  $\sigma_r = \sigma_z = 0$ . Because of this, the deformation work density was:

$$W(\theta) = \int_0^{\epsilon(\theta)} \sigma d\epsilon \quad (2)$$

In the formula and afterwards, the  $\sigma$  and  $\epsilon$  were separately indicated as  $\sigma_\theta$  and  $\epsilon_\theta$ .

The conditions of the plane strains were  $\epsilon_r = 0$ ,  $\epsilon_z = \frac{\sigma_\theta}{2}$ .

$\epsilon_x = 0$  and  $\epsilon_r = -\frac{1}{2}\epsilon_\theta$ . If the material's equivalent stress and strain curves can be approximately indicated by the following formula

$$\sigma_x = \sigma_y \left( \frac{\epsilon_x}{\epsilon_y} \right)^n \quad (3)$$

then

$$W(\theta) = \left(\frac{2}{\sqrt{3}}\right)^{1+m} \int_0^{\epsilon(\theta)} \sigma d\epsilon \quad (4)$$

The deformation work density under mixed conditions can be written as:

$$W(\theta) = f(m) \int_0^{\epsilon(\theta)} \sigma d\epsilon \quad (5)$$

Therefore, based on the material's stress-strain relationship, we can convert the strain distribution  $\epsilon(\theta)$  of the notch root into the equivalent deformation work density distribution which is  $W(\theta)/f(m)$  (see fig. 6.).

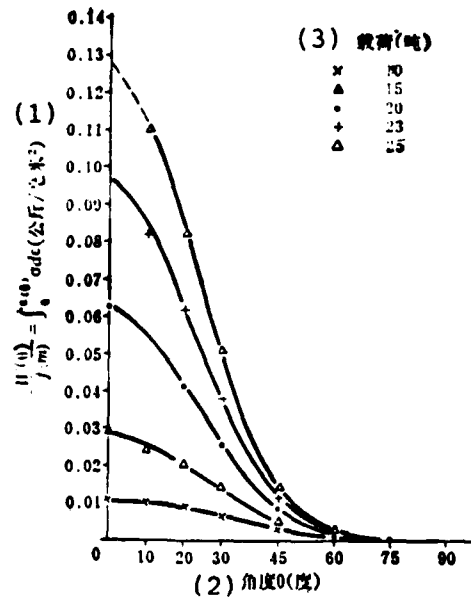


Fig. 6.

Fig. 6. The Deformation Work Density Distribution of Special Q20a Under Different Load Levels

Key: 1. Kilograms/millimeter<sup>2</sup>  
2. Angle  $\theta$  (degrees)  
3. Load (tons)

In the specimen with a  $\rho=20$  millimeter notch, the  $W(\theta)$  can be approximately indicated as:

$$W(\theta) = W_0 \cos^2 \theta \quad (6)$$

For the specimen with a  $\rho=9$  millimeter notch, then:

$$W(\theta) = W_0 \cos^2 \theta \quad (7)$$

### 3. Determining Coefficient A

Based on the definition and characteristics of the J-integral, we can take the notch surface as the integral contour at which time:

$$J = \int_{\Gamma} W dy = \int_{-\pi/2}^{\pi/2} W(\theta) \rho \cos \theta d\theta = A \rho W_0 \quad (8)$$

In the formula

$$A = 2 \int_0^{\pi/2} \varphi(\theta) d\theta \quad (9)$$

In the formula,  $\varphi(\theta) = \frac{W(\theta)}{W_0} \cos \theta$ . When formulas (6) and (7) are separately substituted into formula (9) we can analytically obtain coefficient A.

A=0.91 when  $\rho=20$  millimeters or  $a/\rho=2$

A=1.18 when  $\rho=9$  millimeters or  $a/\rho=4.4$

Based on fig. 6, we can also convert the  $W(\theta)/f(m)$  figure into a  $\varphi(\theta)$  figure (see fig.7.). We can obtain the A value by numerical integration (see table 1).

試件 (1)	$\epsilon_0$ (微應變) (2)	A
Q <sub>200</sub>	1649	1.10
	3554	0.98
	6495	0.91
	≥9230	0.87
Q <sub>100</sub>	1517	1.06
	3252	0.93
	≥5950	0.89
Q <sub>0</sub>	1443	1.21
	≥3004	1.20

Table 1 The A Value Obtained by Numerical Integration

Key: 1. Specimen  
2. (Microstrain)

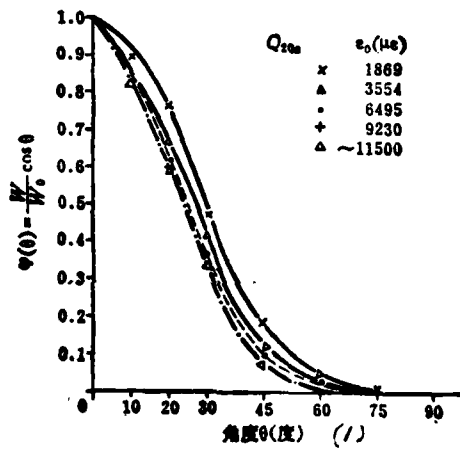


Fig. 7. The  $\phi(\theta)$  Function of Sample  $Q_{20a}$  Under Different Load Levels.

Key: (1) Angle  $\theta$  (degrees)

#### IV. Analysis and Discussion

(1) In the direct ratio of the notch root's maximum deformation work density  $W_0$  to parameter  $J/\rho$  (formula 8), the proportionality coefficient  $A$  is approximately 1, for a specimen of  $a/\rho=2, A \approx 1$  and for a specimen of  $a/\rho=4.4, A \approx 1.2$ .

Specimen  $Q_{20b}$  is directly clamped but because it is not clamped firmly the specimen slips in the clamp hold. When measured from the auxiliary strain piece, we can see that the specimen endures a relatively large bending moment. Even though this be the case, the  $\varphi(\theta)$  and  $A$  values of the  $Q_{20b}$  are close to those of the  $Q_{20a}$ .

Besides this, tests initially proved that the  $A$  value tends to increase following the increases of the  $a/\rho$ . Further, we can infer that  $A$  is related to the hardening characteristics of the material. Yet, when applied in engineering,  $A$  can be viewed as a constant approximately equal to 1.

(2) When the specimen notch is still in a small range yield condition, we can use the calculation of the stress strength factor to obtain the  $J$ -integral value. Thus, when establishing an external load, the specimen and notch geometrical size are related to the notch root's maximum deformation work density.

If we assume that this experimental calibration is in a plane stress situation, then after using Weiss's correction of the plastic zone in the calculation of  $K_1$  we can obtain consistent results (see table 2).

试 样 (1)	$\sigma_g$ (2) (公斤/毫米 <sup>2</sup> )	$\epsilon_0$ (3) (微应变)	$W_0$ (4) (公斤/毫米 <sup>2</sup> )	$J^*$ (5) (公斤/毫米)	$J$
Q20a	1.11	897	0.0028	0.054	0.056
	2.22	1869	0.011	0.22	0.22
	3.33	3554	0.029	0.60	0.58
	4.44	6495	0.063	1.31	1.26
	5.11	9230	0.097	1.97	1.94
	5.56	~11500	0.128	2.54	2.56
Q <sub>6</sub>	1.11	1443	0.007	0.054	0.076
	2.22	3004	0.023	0.024	0.25
	3.11	5119	0.047	0.53	0.50
	3.56	6437	0.062	0.74	0.66
	4.00	8334	0.037	1.01	0.94
	4.22	9424	0.100	1.16	1.08
	4.67	~11400	0.127	1.54	1.37

Table 2.

- Key:
1. Specimen
  2. (kilograms/millimeter<sup>2</sup>)
  3. (Microstrain)
  4. (Kilograms/millimeter<sup>2</sup>)
  5. (Kilograms/millimeter)

$$J = \frac{K_t^2}{E} = \frac{\gamma^2 \sigma_g^2}{E} \left\{ a + \frac{\rho}{4} \left[ \left( \frac{\sigma_m}{\sigma_{0.2}} \right)^2 - 1 \right] \right\} \quad (10)$$

In the formula:

- $\gamma$  is the geometrical form factor of the single edge crack drawn specimen stress strength factor;
- $\sigma_m$  is the maximum theoretically elastic stress concentration stress  $\sigma_m = K_t \sigma_g$  of the notch root;
- $K_t$  is the actually measured elastic stress concentration coefficient;
- $\sigma_g$  is the distant mean stress.

In this paper, for  $Q_{20a}$ ,  $K_t=5.66$ ; and for  $Q_9$ ,  $K_t=8.18$ .  
 By substituting this into formula (10), we can obtain the J-integral value recorded as  $J^*$  (table 2). At the same time, from formula (8) we can obtain the J-integral value recorded as  $J$  (table 2) when  $A=1.0$  is used for  $Q_{20a}$  and  $A=1.2$  is used for  $Q_9$ .

Actually, experimental calibration is not an ideal plane stress condition as the  $W_0$  in  $J^*=A\rho W_0$  should be  $f(m) \int \sigma d\varepsilon$ . In this formula,  $f(m)$  is in the area of 1.0-1.2. Therefore:

$$W_0 = J/\rho = \frac{\gamma^2 \sigma_{\xi}^2}{E} \left\{ \frac{a}{\rho} + \frac{1}{4} \left[ \left( \frac{\sigma_m}{\sigma_{0.2}} \right)^2 - 1 \right] \right\}$$

It is also only an approximate engineering calculation method.

#### References:

1. Cai Qigong, Metal Journal, vol. 12, no. 1(1976), p.45
2. Shen Huiwang, "Analysis of the Low Cycle Fatigue of High Temperature Nickel Alloy and Its Crack Mechanics".
3. Cai Qigong "On the Neuber Relation  $K_0 K_{\xi} = K_t^2$  — the Application of the J-Integral Full Quantity Theory in the Analysis of the Notch Apex Elastoplastic Stress-Strain Field", Metallic Materials, no. 1(1977), p.77.

# J-INTEGRAL EXPERIMENTAL CALIBRATION OF SHEET SPECIMENS WITH SINGLE EDGE NOTCH

*Luo Ligeng, Chen Xianxi and Cai Qigang*

*(Central Iron and Steel Research Institute)*

*Zheng Minzhung*

*(Aircraft Strength Research Institute)*

## Abstract

J-integral of sheet notched specimen has the simplest form when the notched surface has been taken as the integral contour, i. e.

$$J = \int W dy = \int_{-\pi/2}^{\pi/2} W(\theta) \rho \cos\theta d\theta$$

it can be still simplified

$$J = A\rho W_0$$

where

$$A = 2 \int_0^{\pi/2} \varphi(\theta) d\theta$$

and

$$\varphi(\theta) = \frac{W(\theta)}{W_0} \cos\theta$$

it can be seen that the ratio of J-integral to radius of curvature  $\rho$  is proportional to the maximum deformation work density  $W_0$  at notch root.

The specimens were cut from hot rolled sheet of aluminium alloy LY12 with yield strength  $\sigma_{0.2} = 11.2 \text{ kgf/mm}^2$ . The specimen sizes are: thickness  $B = 30\text{mm}$ , width  $W = 150\text{mm}$ , notch depth  $a = 40\text{mm}$ , and the radiuses of notch curvature  $\rho = 20\text{mm}$  and  $9\text{mm}$ , respectively. The resistance strain gauges of 1 by 1mm were adhibited on the inner surface of notch at angles  $\theta$  being  $0^\circ$ ,  $10^\circ$ ,  $20^\circ$ ,  $30^\circ$ ,  $45^\circ$ ,  $60^\circ$ ,  $75^\circ$  and  $90^\circ$ , respectively. And then, the measurement of strain distribution  $\varepsilon(\theta)$  at various load levels was made and deformation work density distribution  $W(\theta)$  was derived from stress-strain curve. The value  $A$ , at last, has been determined by means of numerical integration and the approximation function, and varied in a range of 0.9 to 1.2.

Owing to the limitation of the experimental accuracy and the difficulty in determining exact degree of plane strain, the agreement of experimental calibration of J-integral in the present work with  $J$  converted from equivalent stress intensity factor  $K_{eff}$  considering Weiss's correction of plastic zone can be considered as an approximation for engineering.

## ON THE DESIGN OF TRANSONIC TURBINE CASCADE BY HODOGRAPH METHOD

Ling Zhiguang  
(Institute of Engineering Thermophysics Academia Sinica)

Xin Shaokang and Zhu Shican  
(Fudan University)

### Abstract

The design and realization of a transonic turbine cascade with a low energy loss coefficient is one of the crucial problems for raising the performance of transonic turbines. This paper deals with the inverse design problem of the transonic turbine cascade in the hodograph plane by the finite area method. In the first part of this paper, the governing equation is transformed into a symmetrical form which can be adopted to obtain the upstream singular solution. The boundary condition connected with the existing discontinuity in the hodograph plane is also analyzed and afterwards verified by numerical tests. The next part describes in detail the method of solving the stream function field by means of the finite area method, including the integral transformation of the governing equation, the finite area scheme and the particular corner finite area scheme. The accuracy of the solution is also briefly analyzed. The worked out equation is quite simple and quick-acting. Calculation results prove that the solution is quite stable and it is not necessary to modify the mesh near the sonic line or other places. Calculations also show that the choice of the position of the critical point on the sonic line has a definite effect on the flow field and the blade type molded line

---

Translator's Note: Subscript oo should be read as ∞.

form should be given careful attention in design.

## I. Preface

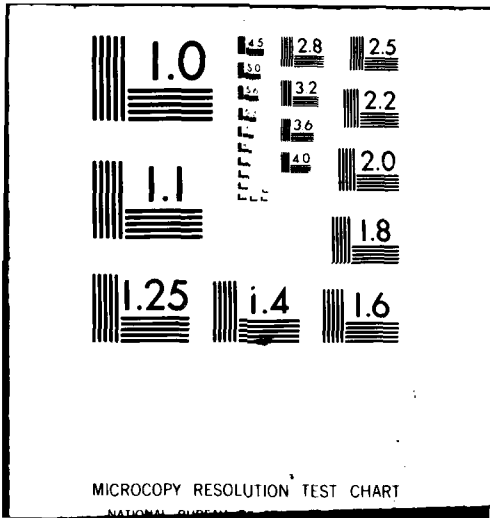
The transonic turbine has great potential for raising efficiency and one of the crucial problems is the molding and designing of a highly efficient transonic turbine cascade. Aerodynamic flow around body calculation methods such as the time correlation method and relaxation method are all forward solutions for various existing transonic turbine cascades. In order to attain a transonic cascade with a low energy loss coefficient, if there are only repeated improvements of the blade type molded lines based on aerodynamic positive calculations, the goal will still not necessarily be able to be attained. This is because the sonic line position and its front and rear flow fields are all able to directly affect the efficiency and performance of the shock wave component and transonic cascade. Sometimes the application of artificial viscosity methods such as the time-correlation method are considered for the calculation of shock wave discontinuity and the resulting shock wave position is a region from which it is difficult to more accurately determine a corrected and improved direction. The test research initially revealed: if we could cause uniformity in front and behind the transonic turbine cascade sonic line, especially in the throat section flow, rationally control the speed gradient and outlet flow field and rationally design a molding line, then it is possible to decrease the viscosity shock wave loss, realize a weak shock wave and even a transonic wing and cascade without shock wave[1-3]. Because of this, we have reason to believe that the transonic turbine cascade is not very appropriate for arbitrary analytical curve modelling resembling the subsonic turbine cascade but should adopt a general position in accordance with the predetermined profile flow velocity distribution and sonic line and use the inverse problem method for the molding design. After obtaining the initial molded lines, the

direct problem method is then used for further computation checking. This type of inverse problem is carried out repeatedly and hopefully obtains a highly efficient transonic turbine cascade series.

The hodograph method takes the speed component or speed molded length and velocity vector direction as the independent variable whereby we obtain the dominant equation of a linear partial differential equation which simplifies the solution. There are already many results[4-7]attained on this aspect of the transonic wing. In recent years, G.Karadimas and D.E. Hobson[8] have carried out effective work in extending the above results to the transonic cascade.

As for the inverse problem, the method provided for the predetermined profile velocity is directly related to the equation and solution. If we use the velocity distribution on the given pressure surface and suction surface along the x axis:  $\lambda_p = f_p(x)$  and  $\lambda_s = f_s(x)$ ,  $\lambda$  is the dimensionless velocity  $V/A_{cr}$ . There is also a given distribution along the arc length direction. This type of supply method is relatively intuitive and seems to be advantageous to the formulation of the control and load of the boundary layer loss. Yet, this is also conditioned because the profile form and curvature are unknown. Therefore, it seems to be insufficient to guarantee that the gas emission angle for the transonic turbine cascade be able to regulate the sonic line location form and a fixed level. The hodograph method takes  $V$  and the velocity vector direction as the independent variables and supplies the relationship of the profile velocity and profile inclination. Aside from simplifying the equation and the other mentioned advantages, when seeking the solution, the sonic line acts as one of the supplied boundaries. Thus, we could also prepare beforehand a fixed control for the sonic line location form. After gaining experience, we could make some restraints beforehand to guarantee the gas emission angle.





Yet, the supplied  $V$  and  $\theta$  distribution on the velocity surface form a solution region and its geometrical shape has a certain arbitrariness and complexity. There are two types of methods used for this: one is to transform this solution region to another conversion velocity surface causing it to become a rectangular region (see appendix 1). The other is even more effective and uses the finite volume method (binary is the finite area method). At present, the finite volume method has attained to very good application for solving the wing and flow around the cascade. For example, Jameson used it to solve the wing's transonic potential flow[11] and McDonald and Denton separately used it to solve the time-correlation relation of the cascade.[12-13] The finite volume method showed the conservation equation as an integration pattern causing the form to be concise and thus raising the stability of the solution. At the same time, a small volume unit component mesh could be conveniently deployed and divided in a rational smooth solution area wherein we obtained a relatively good discrete approximation which was advantageous to the calculation of the complex geometric shape. Because of this, we applied the finite area method to the transonic turbine cascade and even to solving the inverse problem of the sonic line's velocity surface.

## II. Dominant Equation and Boundary Conditions

### 1. Dominant Equation

If the shock wave in the cascade is very weak, the effect on the boundary layer is also very small. We can write mass discrete and irrotational equations for the plane, irrotational and permanent flows:

$$\frac{\partial}{\partial x} (\rho V_x) + \frac{\partial}{\partial y} (\rho V_y) = 0 \quad (1)$$

$$\frac{\partial}{\partial y} V_x - \frac{\partial}{\partial x} V_y = 0 \quad (2)$$

Now, the independent variable changes to  $V$  and  $\theta$  and introduces stream function  $\psi$  and potential function  $\Phi$  :

$$\begin{aligned} d\Phi &= V_x dx + V_y dy \\ d\psi &= -\rho V_x dx + \rho V_y dy \end{aligned}$$

Held on the physical surface:

$$dz = \frac{e^{i\theta}}{V} \left( d\Phi + \frac{i}{\rho} d\psi \right)$$

After arrangement, the separate derivations of  $\theta$  and  $V$  on the velocity surface are:

$$\frac{\partial \Phi}{\partial \theta} = \frac{V}{\rho} \frac{\partial \psi}{\partial V} \quad (3)$$

$$V \frac{\partial \Phi}{\partial V} = \frac{1}{\rho} \left( 1 + V \frac{\partial \ln \rho}{\partial V} \right) \frac{\partial \psi}{\partial \theta} \quad (4)$$

After merging and becoming nondimensionalized, we can obtain:

$$L(\psi^*) = \frac{\partial}{\partial \theta} \left( P \frac{\partial \psi^*}{\partial \theta} \right) + \frac{\partial}{\partial \lambda} \left( Q \frac{\partial \psi^*}{\partial \lambda} \right) = 0 \quad (5.1)$$

In the formula

$$\begin{aligned} \psi^* &= \rho_{-1} V_{-1} t \cos \theta_{-1}, \quad P = -\frac{1}{\lambda} \frac{1-\lambda^2}{(1-B\lambda^2)^{2+1}}, \\ Q &= \frac{\lambda}{(1-B\lambda^2)^c}, \quad B = \frac{\kappa-1}{\kappa+1}, \quad c = \frac{1}{\kappa-1}, \quad t \text{ 为栅距。} \end{aligned} \quad (1)$$

Key: 1.  $t$  is the blade pitch

Formula (5) is the linear partial differential equation needed for the solution.

Formula (5) can be further transformed into a symmetrical form. Letting  $\bar{\Phi} = \rho_{-1} \Phi$  and  $\Omega = \frac{(1-B\lambda^2)^2}{(1-B)}$  =  $f(\lambda)$ , after using the new equivalent independent variable  $\lambda'$  to substitute for  $\lambda$ , we obtain:

$$\frac{\partial \bar{\Phi}}{\partial \theta} = W \frac{\partial \psi^*}{\partial \lambda'} \quad (6)$$

$$\frac{\partial \bar{\Phi}}{\partial \lambda'} = -W \frac{\partial \psi^*}{\partial \theta} \quad (7)$$

In the formula

$$W = \frac{\sqrt{1-M^2}}{\Omega},$$

and

$$\lambda' = \int \frac{\sqrt{1-M^2}}{\lambda} d\lambda,$$

which is

$$\lambda' = \frac{1+B}{1-B} \log \left[ \left( \frac{\sqrt{1-\lambda^2} - \sqrt{1-B\lambda^2}}{\sqrt{1-\lambda^2} + \sqrt{1-B\lambda^2}} \right)^{1/2} / \left( \frac{B\sqrt{1-\lambda^2} - \sqrt{B(1-B\lambda^2)}}{B\sqrt{1-\lambda^2} + \sqrt{B(1-B\lambda^2)}} \right)^{1/2} \sqrt{B} \right] + C$$

Thus, formula (5) becomes:

$$L(\psi^*) = \frac{\partial}{\partial \theta} \left( W \frac{\partial \psi^*}{\partial \theta} \right) + \frac{\partial}{\partial \lambda'} \left( W \frac{\partial \psi^*}{\partial \lambda} \right) = 0 \quad (8)$$

## 2. Boundary Conditions

After utilizing the stream function from figure 1, the boundary conditions of  $\Psi_s^* = 0$  on the suction surface along the blade surface,  $\Psi_p^* = 1$  on the pressure surface and  $\psi_c = f(\theta)$  on the sonic line can be determined by using the singular solution of a mixed type equation [6].

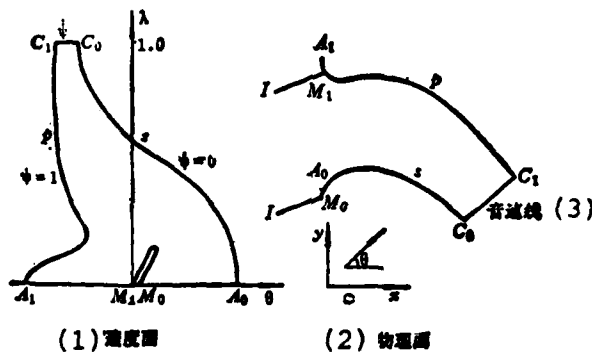


Fig. 1.

Fig. 1.

- Key: 1. Velocity surface  
2. Physical surface  
3. Sonic line

Up to the present, the difference between the various singular solutions lie in the accuracy of their compression functions. Other approximate hypotheses were all the same but in the area of the sonic line the differences of the compressibility functions were very small. When we used Germain's [10] solution, which shows that there is a critical single point  $\theta_c$  nozzle on the throat part, then

$$\psi_s = \frac{(\theta_r - \theta_s)^{1/3} - (\theta - \theta_s)^{1/3}}{(\theta_r - \theta_s)^{1/3} - (\theta_p - \theta_s)^{1/3}}$$

The upstream boundary conditions are the distant overtaking flows  $\lambda_{oo}$  and  $\theta_{oo}$  which forms single point I on the velocity surface from the cycling of the flow. Further, after selecting the blade's "geometric" stagnation points  $A_1$  and  $A_o$ , we can then determine the solution area  $IM_1 A_1 C_1 C_o A_o M_o I_o$  on the velocity surface. To sum up, the problem is the solution of "degenerated" elliptic equation (5)<sup>F.N.1</sup> or equation (8).

Because the equation is linear, its solution can be obtained from a combination of the regular solution and singular solution, which is  $\gamma^* = \gamma' + \gamma_{oo}$ . In this equation,  $\gamma'$  is the regular solution and  $\gamma_{oo}$  is the singular solution near the upstream I point. Therefore, the solution equation changes to:

F.N.1: Because it is necessary to directly solve the singularity sonic line.

$$L(\psi') = I(\psi^*) - L(\psi_\infty) = -L(\psi_\infty) \quad (9)$$

We used an approximation  $\frac{I}{\lambda}$  of  $W = \frac{\sqrt{1-M_\infty^2}}{Q_\infty}$  in formula (8) and formula (8) changed in the Laplace equation. From this, we could directly attain the Fenain results:

$$\psi_\infty = \frac{\omega}{2\pi} - \frac{\text{tg}\theta_\infty}{2\pi\sqrt{1-M_\infty^2}} \log R + C \quad (10)$$

In the formula

$$R = \sqrt{\frac{(\lambda - \lambda_\infty)^2}{\lambda_\infty^2} + \frac{(\theta - \theta_\infty)^2}{1 - \lambda_\infty^2}}, \quad \omega = \text{tg}^{-1} \left( \frac{\lambda - \lambda_\infty}{\lambda_\infty} / \sqrt{1 - \lambda_\infty^2} \right)$$

Now, the solution area is  $A_1 C_1 C_0 A_0 M_0 M_1 A_1$  and the boundary conditions are:  $\psi' = -\psi_\infty$  for  $\widehat{A_0 C_0}$ ;  $\psi = 1 - \psi_\infty$  for  $\widehat{A_1 C_1}$ ; and

$\psi' = \psi_c - \psi_\infty$  for  $\widehat{C_1 C_0}$ . It is necessary to further discuss the  $A_1 M_1 M_0 A_0$  line because the  $M_1 M_0$  area function is non-continuous.

It jumps from the  $\psi^* = 1$  in the  $M_1$  area to the  $\psi^* = 0$  in the  $M_0$  area and is also on the  $\lambda = 0$  line:  $\psi' = -\psi_\infty$  for  $\widehat{A_1 M_1}$ ;  $\psi = 1 - \psi_\infty$

for  $\widehat{A_0 M_0}$ . In order to maintain a continuous  $\psi$  on the solution area boundary it is necessary to establish  $\psi'|_{M_1} = \psi'|_{M_0}$ . This



arbitrary value such as 0.5 etc. (see fig. 2). From this comes the corresponding C value and given  $\omega_A$ . Numerical tests proved that no matter what the value of  $\psi'|_{M_0} = \psi'|_{M_1}$ , the results were the same. We could also understand why the final result was

$\psi^* = \psi' + \psi_{\infty}$ . The above result was obtained assuming IM was obtained in a straight line. Actually, IM represents the upstream flow field and any  $\omega$  origin can be selected along IM.

### III. Solution Method

We used the finite area method to solve the boundary value problem of formula (9).

#### 1. Transformation of Equation

In order to be appropriate for solving the finite area method, the integral of formula (9) was:

$$\iint_D \left[ \frac{\partial}{\partial \theta} (P\psi'_\theta) + \frac{\partial}{\partial \lambda} (Q\psi'_\lambda) \right] d\theta d\lambda = \iint_D f_1(\theta, \lambda) d\theta d\lambda$$

In the formula,  $f_1(\theta, \lambda) = L(\psi_{\infty})$ . After applying the Green formula:

$$\oint_{\partial D} (P\psi'_\theta d\lambda - Q\psi'_\lambda d\theta) = \oint_{\partial D} (P\psi'_\theta n_\lambda + Q\psi'_\lambda n_\theta) ds = \iint_D f_1(\theta, \lambda) d\theta d\lambda \quad (11)$$

In order to simplify calculations below,  $\psi'$  is written as  $\psi$ .

#### 2. Treatment of Format

Using a non-equidistant  $\lambda = \text{const}$  line (actually it is not absolutely necessary to use an equal  $\lambda$  line, yet because  $\lambda=0$  and  $\lambda=1$  are boundaries, the use of an equal  $\lambda$  line is more convenient) and an equally separated point joining line along the

$\lambda = \text{const}$  line, we cut up the solution area into an arbitrary tetrahedron. The stream function  $\Psi$  was defined in each format center area. For each tetrahedron mesh in the solution area, the peripheral integrals in formula (11) can be changed into line integral sums on the four sides.

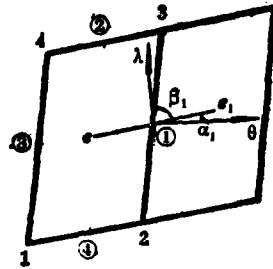


Fig. 3.

For example, the 2-3 side in figure 3 has:

$$\begin{aligned} I_{\alpha} &= \int_2^3 (P\psi_0 n_0 + Q\psi_{\lambda} n_{\lambda}) ds \approx \bar{P}\bar{\psi}_0 \int_2^3 n_0 ds + \bar{Q}\bar{\psi}_{\lambda} \int_2^3 n_{\lambda} ds \\ &= \bar{P}\bar{\psi}_0 (\lambda_3 - \lambda_2) + \bar{Q}\bar{\psi}_{\lambda} (\theta_2 - \theta_3) \end{aligned}$$

In the formula,  $\bar{P}$ ,  $\bar{Q}$ ,  $\bar{\psi}_0$  and  $\bar{\psi}_{\lambda}$  are all mean values in the integration area. We took point P and Q values in the area as  $\bar{P}$  and  $\bar{Q}$ . Because  $\Psi$  was only defined in the format center areas, it was necessary to provide the expression of derivatives  $\bar{\psi}_0$  and  $\bar{\psi}_{\lambda}$ . Using the directional derivative:

$$\frac{\partial \psi}{\partial l} = \frac{\partial \psi}{\partial \theta} \frac{\partial \theta}{\partial l} + \frac{\partial \psi}{\partial \lambda} \frac{\partial \lambda}{\partial l} = \psi_0 l_0 + \psi_{\lambda} l_{\lambda}$$

If for point ① of the 2-3 side in fig.3 we take the l direction as

the  $ee_1$  direction and 2-3 direction, then:

$$\frac{\psi_{e_1} - \psi_e}{\Delta r_{ee_1}} = \psi_{e_1} \cos \alpha_1 + \psi_{e_2} \sin \alpha_1$$

$$\frac{\psi_3 - \psi_2}{\Delta s_{32}} = \psi_{e_1} \cos \beta_1 + \psi_{e_2} \sin \beta_1$$

In the formula,  $\Delta s_{32}$  is the distance between the two adjoining points; and  $\Delta r_{ee_1}$  is the distance between the two adjoining format centers.  $\psi_{e_1}$  is the point ① area  $\psi_{e_2}$  and  $\psi_e$  is the point ① area  $\psi_e$  (see fig. 4). When  $a_1=0$  (using the equal  $\lambda$  line to divide the mesh), we can obtain

$$\psi_{e_1} = \frac{\psi_{e_1} - \psi_e}{r_{ee_1}}$$

$$\psi_{e_2} = \frac{\psi_3 - \psi_2}{\Delta s_{32} \sin \beta_1} - \text{ctg} \beta_1 \psi_{e_1} \quad (12)$$

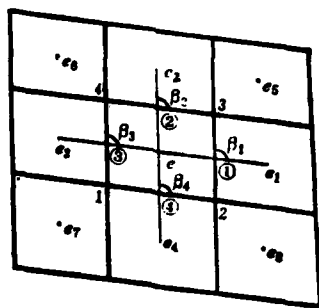


Fig. 4.

Taking  $\psi_3 = \frac{1}{4} (\psi_e + \psi_{e_1} + \psi_{e_5} + \psi_{e_2})$  and  $\psi_2 = \frac{1}{4} (\psi_e + \psi_{e_1} + \psi_{e_4} + \psi_{e_8})$ , then

$$\psi_{\lambda, \theta} = \frac{\psi_{\sigma_3} + \psi_{\sigma_2} - \psi_{\sigma_4} - \psi_{\sigma_3}}{4\Delta s_{32} \sin \beta_1} - \frac{\psi_{\sigma_1} - \psi_{\sigma_2}}{r_{\sigma\sigma_1}} \operatorname{ctg} \beta_1$$

Therefore, the 2-3 side can be written as:

$$I_{\theta} = P(\lambda_e) \frac{\psi_{\sigma_1} - \psi_{\sigma_2}}{\Delta r_{\sigma\sigma_1}} (\lambda_3 - \lambda_2) + Q(\lambda_e) \left[ \frac{\psi_{\sigma_3} - \psi_{\sigma_2} - \psi_{\sigma_4} - \psi_{\sigma_3}}{4\Delta s_{12} \sin \beta_1} - \operatorname{ctg} \beta_1 \frac{\psi_{\sigma_1} - \psi_{\sigma_2}}{\Delta r_{\sigma\sigma_1}} \right] (\theta_2 - \theta_3)$$

Here,  $\lambda_3$ ,  $\theta_3$ ,  $\lambda_2$  and  $\theta_2$  are the  $\lambda$  and  $\theta$  values of points 3 and 2, and  $P(\lambda_e)$  and  $Q(\lambda_e)$  are the P and Q values of the  $\lambda = \lambda_e$  area.

Similarly, point ④ of the 1-2 side has:

$$\psi_{\theta, \lambda} = \frac{\psi_2 - \psi_1}{\Delta s_{12}} = \frac{\psi_{\sigma_8} + \psi_{\sigma_1} - \psi_{\sigma_7} - \psi_{\sigma_3}}{4\Delta s_{12}}$$

$$\psi_{\lambda, \theta} = \frac{\psi_{\sigma_2} - \psi_{\sigma_4}}{\Delta r_{\sigma\sigma_4} \sin \beta_4} - \operatorname{ctg} \beta_4 \frac{(\psi_{\sigma_8} + \psi_{\sigma_1} - \psi_{\sigma_7} - \psi_{\sigma_3})}{4\Delta s_{12}}$$

Because  $\lambda_1 = \lambda_2$ , therefore

$$I_3 = Q \left( \frac{\lambda_e + \lambda_{e_4}}{2} \right) \left( \frac{\psi_e - \psi_{e_4}}{\Delta r_{ee_4} \sin \beta_e} - \operatorname{ctg} \beta_e \frac{\psi_{e_3} + \psi_{e_1} - \psi_{e_2} - \psi_{e_3}}{4 \Delta s_{12}} \right) (\theta_2 - \theta_1)$$

$I_2$  and  $I_3$  are analogous. When the four sides are added together we obtain:

$$\sum_1^4 I = I_x + I_y + I_z + I_4 = \sum_i a_i \psi_{ei} = f_1(\lambda_e, \theta_e) \frac{\Delta s_{1e} + \Delta s_{12}}{2} \Delta s_1 \sin \beta_1$$

In the formula,  $a_{1i}$  is the coefficient of  $\psi_e$  and  $\psi_{e_i}$ .

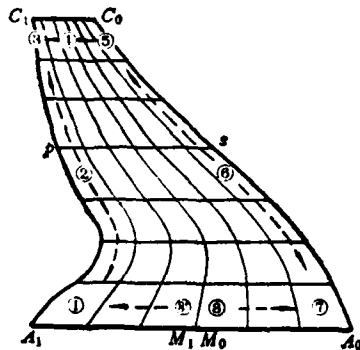


Fig. 5.

The boundary infinitesimal has eight types of different situations (Fig. 5) wherein it is necessary to treat and write out their integration formulas. For example, for situation ③, from Fig. 6,  $\Psi = 1 - \Psi_{00}$  on the 1-4 side, and  $\Psi = \Psi_c(\theta) - \Psi_{00}$  on the 3-4 side. Therefore

$$\psi_{00} = \frac{\psi_c(\theta_3) - \psi_{-2} - (1 - \psi_{-4})}{\Delta s_{34}}$$

$$\psi_{10} = \frac{\psi_c(\theta_3) - \psi_{-2} - \psi_{-4}}{\left(\frac{\Delta s_{23} + \Delta s_{41}}{4}\right) \sin \beta_2} - \operatorname{ctg} \beta_2 \frac{\psi_c(\theta_3) - \psi_{-2} - (1 - \psi_{-4})}{\Delta s_{34}}$$

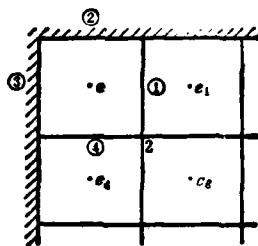


Fig. 6.

Thus

$$I_2 = Q(1)(\theta_3 - \theta_4) \left[ \frac{\psi_e(\theta_3) - \psi_{-2} - \psi_e}{\left(\frac{\Delta s_{33} + \Delta s_{41}}{4}\right) \sin \beta_3} - \operatorname{ctg} \beta_2 \frac{\psi_e(\theta_3) - \psi_{-2} - (1 - \psi_{-2})}{\Delta s_{34}} \right]$$

and

$$\psi_{e3} = \frac{\psi_e - (1 - \psi_{-2})}{\left(\frac{\Delta s_{34} + \Delta s_{12}}{4}\right)}$$

$$\psi_{e3} = \frac{\psi_{-1} - \psi_{-2}}{\Delta s_{41} \sin \beta_3} - \operatorname{ctg} \beta_3 \frac{\psi_e - (1 - \psi_{-2})}{\left(\frac{\Delta s_{34} + \Delta s_{12}}{4}\right)}$$

Therefore

$$I_3 = P(\lambda_e) \frac{\psi_e - (1 - \psi_{-2})}{\left(\frac{\Delta s_{34} + \Delta s_{12}}{4}\right)} (\lambda_1 - \lambda_4) + \theta(\lambda_e) \left[ \frac{\psi_{-1} - \psi_{-2}}{\Delta s_{41} \sin \beta_3} - \operatorname{ctg} \beta_3 \frac{\psi_e - (1 - \psi_{-2})}{\left(\frac{\Delta s_{34} + \Delta s_{12}}{4}\right)} \right] (\theta_4 - \theta_1)$$

Finally, the related simultaneity of the infinitesimal mesh defines the linear algebraic system of first order equations in each format center  $\Psi$  and then the solution is carried out.

### 3. Annotation of Several Points

(1) For the most part, the finite area method is carried out for a system of first order equations. For example: equation (5) can also be written to form a system of first order equations

$$\begin{aligned} \frac{1}{Q} \frac{\partial \bar{\Phi}}{\partial \theta} - \frac{\partial \psi}{\partial \lambda} &= 0 \\ \frac{\partial \bar{\Phi}}{\partial \lambda} + P \frac{\partial \psi}{\partial \theta} &= 0 \end{aligned}$$

After integration

$$\begin{aligned} \oint \left( \frac{1}{Q} \bar{\Phi}_{n_1} - \psi_{n_1} \right) ds &= 0 \\ \oint \left( \bar{\Phi}_{n_1} - P \psi_{n_1} \right) ds &= 0 \end{aligned} \tag{13}$$

At this time, the mean values of the two adjoining mesh format centers are used for the value on the infinitesimal area boundary. The presently used equation (5) has direct integration and utilizes the derivative value on the boundary. The coordinates of the four angle nodal points use the mean values of the four

mesh format center. The accuracy is raised and some are similar to the Lax format. The use of the 4 point means is also advantageous to stability. Aside from this, the use of a system of first order equations can also save on the machine's storage quantity.

(2) In the solution, the first order derivative  $\psi_n$  approximation uses the difference quotient alternate approximation of the  $\lambda$  and  $\theta$ -directions and the accuracy is in the first to second order range. When the mesh degenerates to a square it has second order accuracy equal to the central difference. From Fig. 3, when  $B_i = 90^\circ$ ,

$$\begin{aligned} \frac{\partial \psi_f}{\partial n} \Big|_{i, j+1/2} &= \frac{\psi_{f,i+1,j} - \psi_{f,i,j}}{\Delta \lambda} \\ \frac{\partial \psi_f}{\partial n} \Big|_{i+1/2, j} &= \frac{\psi_{f,i+1,j} - \psi_{f,i,j}}{\Delta \theta} \end{aligned}$$

(3) We can also use the weighted residue method of taking the weight function as 1 for the integration of formula (8). If the weight function acts as the form function, mathematically speaking, this corresponds to the finite element method.

(4)  $\psi_{\infty}$  is the singular solution "near" the upstream infinity area. We continued the use of the method in reference [1] and employed it for the whole solution area; although this method was much more convenient to use than the hypergeometric function for seeking the effects of the upstream single point, yet the approximation was larger. Therefore, in the next step, we calculated the problem of the first category

boundary value conditions in carrying out a direct solution of formula (8) or (5) on a fractured surface.

#### IV. Calculations and Discussion

Based on the above mentioned method worked out on a computer program, we obtained the  $\Psi$  field in the solution's linear algebraic series of equations. After obtain the  $\Psi^*$  field we used numerical integration to directly calculate the s surface, p surface, and x and y sonic line coordinates. The coordinate origin was taken on the intersecting point of the s surface and sonic line. For the supersonic part we continued the use of the characteristic line solution method.

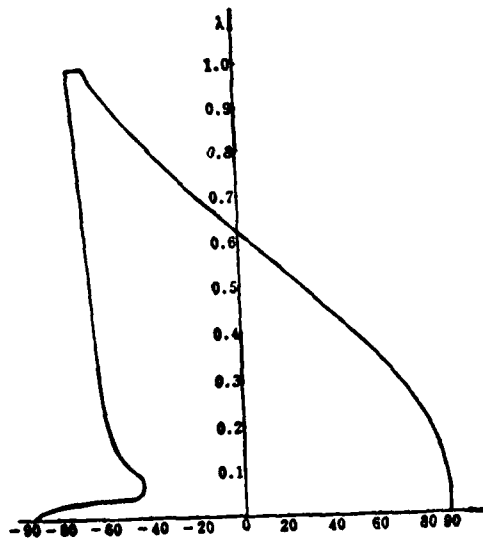


Fig. 7(a) The Relationship of the  $\lambda - \theta$  Distribution System

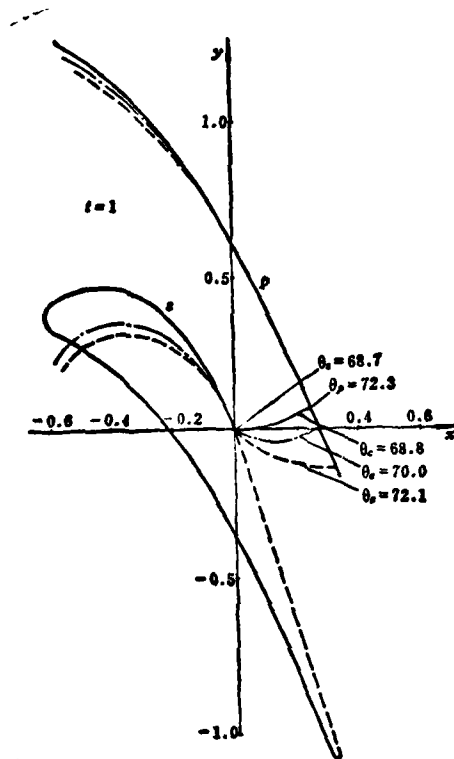


Fig. 7(b) Profile Calculation Example

Fig. 7 is the calculation results. The cascade nodal distance  $t$  is taken as 1, the upstream overtaking flow is  $M_{\infty} = 0.15$ , the axis gas intake is  $\alpha_0 = 90^\circ$  and the gas emission angle is  $\alpha_{1.0} \approx 15^\circ$ . Fig. 7(a) gives the  $\lambda - \theta$  distribution and Fig. 7(b) is the sought transonic turbine guide blade profile.

(1) In the relationship of the given velocity distributions, at the sonic line  $\lambda = 1$  area,  $\theta_p = 72.3^\circ$  and  $\theta_s = 68.7^\circ$ . The calculations practically proved that the selection of the critical

single point  $\theta_c$  was not only related to the performance of the supersonic part form but the effect on the profile of the front surface of the sonic line and the form and position of the sonic line was rather great and quite sensitive. Fig. 7(b) shows the results created by three types of  $\theta_c$  values wherein  $\theta_c = 68.8^\circ$  is taken as relatively good. It can be seen from this that when we want to obtain a uniform flow in the throat area, the subsonic line form is very important. After providing pressure surface  $p$  and the  $\lambda - \theta$  relationship of the suction surface, following adjustment the  $\theta_c$  can obtain a relatively good value. Concrete calculation examples have also showed that in a certain overtaking flow M number sphere, the  $\theta_c$  point near the back arc will cause the sonic line to become even more level and straight. This is equal to causing the exit back arc to approach a straight line shape.

(2) After the  $\psi^*$  field is known, the return physical surfaces  $x$  and  $y$  require separate integration formulas for the  $p$  and  $s$  surfaces:

$$x_1 - x_0|_{p,s} = \bar{c} \int_0^1 \frac{1}{\lambda} \left[ P + Q \left( \frac{d\theta}{d\lambda} \right)^2 \right] \frac{\partial \psi^*}{\partial \theta} \cos \theta d\lambda \quad (14)$$

$$y_1 - y_0|_{p,s} = \bar{c} \int_0^1 \frac{1}{\lambda} \left[ P + Q \left( \frac{d\theta}{d\lambda} \right)^2 \right] \frac{\partial \psi^*}{\partial \theta} \sin \theta d\lambda \quad (15)$$

For the sonic line

$$x_i - x_o|_e = \bar{c} \int_0^i \left[ \frac{\partial \psi}{\partial \lambda} \cos \theta - \frac{\partial \psi^*}{\partial \theta} \sin \theta \right] d\theta \quad (16)$$

$$y_i - y_o|_e = \bar{c} \int_0^i \left[ \frac{\partial \psi}{\partial \lambda} \sin \theta + \frac{\partial \psi^*}{\partial \theta} \cos \theta \right] d\theta \quad (17)$$

In the formulas, the  $\bar{c} = \frac{P_{00}}{P_{cr}} \lambda_{00} \cos \theta_{00}$  is obtained from the given overtaking flow conditions. In order to satisfy the profile seal condition there should be

$$(x_n - x_o)|_e + (x_m - x_o)|_e = (x_n - x_{op})|_e$$

In the formula,  $n$  indicates the integration end points of the  $p$  and  $s$  surfaces,  $m$  is the end point of the sonic line,  $x_{op}$  and  $y_{op}$  are the coordinates of the  $p$  surface integration beginning points and  $x_{op} = x_{mo}$ . If  $i$  is used to indicate the flow points on the  $p$  or  $s$  surfaces, then the blade thickness distribution can be shown as:

$$\delta_i = t + (y_i - y_o)|_e - (y_i - y_{op})|_e - (y_m - y_o)|_e$$

During the actual calculation procedure, it was necessary to repeatedly adjust and modify the original data (the  $\lambda - \theta$  distribution of pressure surface  $p$  and suction surface  $s$ ) or consider the relationship of the profile's form velocity and

inclination changes so as to obtain a relatively good seal and to satisfy the thickness distribution of the profile. After gaining a certain amount of experience, this was not difficult. Because the function P value had singularity, when there was actual integration, we could try to shift to the upper half of the mesh. Although this caused the leading edge to have a small number of breaks, this problem did not have a very large effect when there were many mesh nodal points.

(3) When using the finite area method for solution, it was necessary to divide the mesh for the solution area and solve the mesh's central values. The mesh was divided in detail and solution accuracy was raised. As regards the solution results, if a relatively rough mesh was used, the results were completely stable near the  $\lambda = 1$  area. The same holds true for the  $\lambda = 0$  area. In this way, it was not necessary to have relaxation difference solution in some places. For example, with the use of under-meshing near the sonic line, the mesh was finer in the  $\lambda$  direction or a mesh with an undetermined value was used. This also used the special characteristics of the finite area method and was one of the advantages.

#### V Brief Summary

(1) This paper presented the use of the finite area method on the velocity surface for the solution of the transonic turbine cascade as well as the inverse problem results of the sonic line, a concrete description of the treatment of the equation, the solution method steps and the handling of the format. It also discussed the accuracy of the solution. After using this method for numerical calculation and analysis, the program was concise and calculation time was short which could be appropriate for a complex area form. Moreover, it was not necessary to have more meticulous treatment near the sonic line. This point is an improvement over the method found in reference [1].

(2) Calculations showed that the selection of critical single points of the throat's sonic line which have a rather great effect on the sonic line form and profile form should be given careful attention in modelling design calculations.

Appendix The Transformation of the Solution Area on the Velocity Surface

In taking  $\xi = \frac{\theta - \theta_p}{\theta_s - \theta_p}$  and  $\eta = y$  as the transformation of the coordinates on the velocity surface (Fig. 8), we had:

$$\frac{\partial}{\partial \theta} = \frac{1}{\theta_s - \theta_p} \frac{\partial}{\partial \xi}, \quad \frac{\partial}{\partial \lambda} = \frac{\partial}{\partial x} \frac{\partial x}{\partial \lambda} - \frac{\partial}{\partial y}$$

Letting  $g = \frac{\partial x}{\partial \lambda}$ , we obtained from the relationship in the coordinates:

$$g = \frac{(\theta - \theta_p)\theta'_p - (\theta_s - \theta_p)\theta'_s}{(\theta_s - \theta_p)^2}$$

In the formula  $\theta'_p$  and  $\theta'_s$  are the  $\theta_p$  and  $\theta_s$  partial derivatives for  $\lambda$ . In the same way, we can obtain:

$$g' = \frac{\partial^2 x}{\partial \xi^2} = (\theta_p'(0\theta_r + \theta_p\theta_r - \theta_p\theta - \theta_r^2) + \theta_r'(-\theta\theta_r + \theta_p\theta_r + \theta_p\theta - \theta_r^2) + 2\theta_p'\theta_r'(\theta_r - 2\theta + \theta_p) + 2\theta_p'^2(\theta - \theta_r) + 2\theta_r'^2(\theta - \theta_p)) / (\theta_r - \theta_p)^3$$

Letting  $g_y = \frac{\partial Q}{\partial y}$  and  $Q_y = \frac{\partial Q}{\partial y}$ , on the converted velocity surface, equation (5) becomes:

$$\left[ \frac{P}{(\theta_r - \theta_p)^2} + Q_x^2 \right] \frac{\partial^2 \psi}{\partial \xi^2} + Q \frac{\partial^2 \psi}{\partial \eta^2} + 2Q_x \frac{\partial^2 \psi}{\partial \eta \partial \xi} + (gg'Q + g_y Q + gQ_y) \frac{\partial \psi}{\partial \xi} + Q_y \frac{\partial \psi}{\partial \eta} = 0 \quad (5')$$

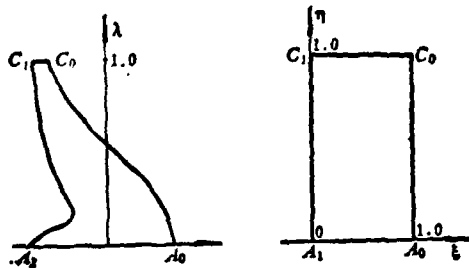


Fig. 8.

## References

1. G. Karadimas, "Trace des aubages de turbine transsoniques par la methods de l'hodograph" VKI LS-59.
2. G.E.Nieuland & B.M. Spee, "Transonic shock-free flow, factor or fiction" AGARD CP-35.
3. J.W. Boerstael & R. Uijenhoet, "Lifting airfoils with super-critical shock-free flow" NLR.MP-7015U.
4. D.G. Korn, "Computation of shock-free transonic flows for air-foil design" PB 186124.
5. G.Y. Nieuland, "Transonic potential flow around a family of quasielliptical airfoil section" NLR.TR.172
6. P. Germain, "Problems mathmatiques poses par l'application de la methode de l'hodographe a l'etude des ecoulements transoniques" Symposium Transonicum Aachen 1962.
7. M.S. Cahn & M. Andrew, "Determination of subsonic drag arise by hodograph plane analysis" AIAA 67-4.
8. D. Hobson, "Hodograph method for the design of transonic turbine blade" CUED/A-Turbo/TR.40.
9. F. Fenain, "Methodes numerique de resolution des problems d'ecoulement mixte autour de profils" N.T.ONERA 4/128 AN-Juiller 1969.
10. P. Germain, "Recherche sur une equation du type mixte" La Recherche Aeronautique 1951 No. 22.
11. A. Jameson & D.A. Caughey, "A Finite volume method for transonic potential flow calculations" AIAA 77-635.
12. J.D.Denton, "A time marching method for two and three dimensional blade to blade flows" ARC R&M No. 3775.
13. P.W. McDonald, "The computation of transonic flow through two-dimensional gas turbine cascades" ASME paper 71-GT-89.

THREE DIMENSIONAL STRESS ANALYSIS FOR A SHROUDED AIR-COOLED  
TURBINE BLADE

Shung Changbing and Ziao Junxiang  
(Beijing Institute of Aeronautics and Astronautics)

Abstract

Up to now, there are still no accurate and reliable methods for computing the stress field of a shrouded air-cooled turbine blade because the cooled blade with a complex figuration works under high temperatures and centrifugal loads; moreover, the distribution of aerodynamic loads is rather non-uniform. Generally, such problems which occur in practice are handled by means of experiments of statistics.

In attempting to solve these problems, we applied the high order three dimensional isoparametric elements for describing the complex configurations of blades. In order to solve the high order linear system of equations, we have used the frontal method with high accuracy and considerable economy of main memory space. The high order bicubic Coons interpolation function is also used to fit the space curved surface. In order to verify the present method and the reliability of the given program, we have compared the results of numerical computations with those obtained from experiments on the revolution of the real blades at high speeds, and the comparison confirms the adaptability and the satisfactory accuracy of the present method.

This method is appropriate for various blades such as solid

or hollow blades, shrouded or unshrouded blades, blades with or without a shank root, and at high or normal temperatures.

## I. Preface

The analysis and calculation of the high temperature fields and stress fields of shrouded air-cooled hollow blades is a major research topic brought forth by related departments in China. When used by an engine, it can improve the performance parameter greatly and raise its lifespan. At present, there are already many types of advanced engines making use of it. After the appearance of the finite element method, references [1] and [4] had calculated the temperature field and thermal stress for the shrouded hollow blade. Yet, the three dimensional blade was simplified into the handling of the problem of the plane. Naturally, there is a great difference between this and the real situation.

A few of the major characteristics of this type of blade are: firstly, it is composed of an irregularly shaped shroud, possesses a special profile and a warped blade body as well as various special types of cooling holes and shank roots. Because of this, it is very difficult to disperse on the curve side element, to fit on the special form and to automatically produce on the nodal point coordinates. Secondly, the blade works under a complex load. Its tangent velocity generally reaches to 250-300 meters/second and therefore the centrifugal load is very great. Moreover, the barycentric shifts of each tangent surface produce added moment. When the unevenly distributed aerodynamic load is along the arc direction and radial direction, it is extremely difficult to simulate the boundary conditions. The working temperature of the air-cooled blade (in front of the turbine) reaches to over 1500K, there is very great thermal stress produced on the side of the cooling hole and the high temperature area often has burning. Thirdly, testing and

measuring are difficult. When the blade works under high temperature and high rotational speed, it is impossible to directly measure the required temperature and stress distribution of each point. Moreover, it is even more difficult to simulate the engine's various working conditions in a laboratory. Fourth, theoretical calculations are difficult. There are many load types that require calculation for the blade and this is very difficult. For example, at present, the temperature boundaries and aerodynamic boundary conditions are being studied, yet the calculation of the temperature field and stress field depend on the accuracy of giving these conditions. Furthermore, the order of the series of equations is also an outstanding problem.

## II. Basic Method

At present, the three dimensional curved side isoparametric element method is one effective method that can solve the calculation of the complex blade's temperature and stress. We selected a high order 20 nodal point three dimensional element. The external form of the blade is shown in fig. 1., and fig. 2. is the employed element.

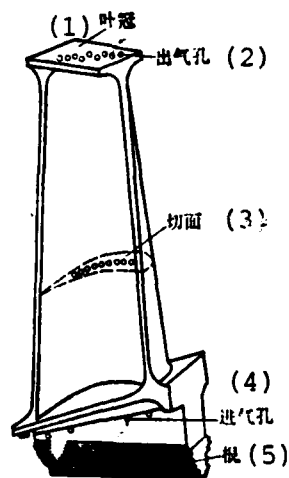


Fig. 1.

Fig. 1. External Form of the Shrouded Air-Cooled Blade

- Key: 1. Shroud  
 2. Gas emission hole  
 3. Tangent plane  
 4. Gas intake hole  
 5. Root

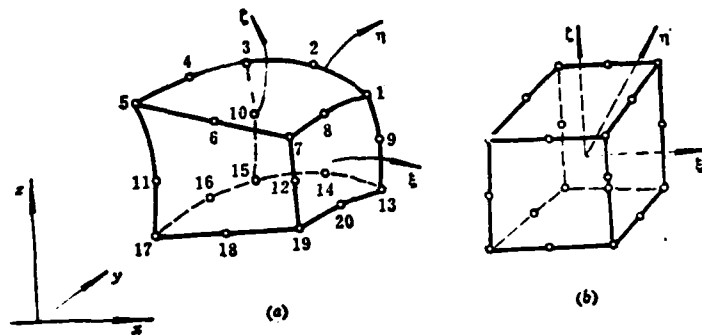


图 2  
 (a) 整体坐标  $(x, y, z)$ , (b) 局部坐标  $(\xi, \eta, \zeta)$ 。

Fig. 2

- Key: (a) Integral coordinate  $(x, y, z)$ ;  
 (b) Local coordinate  $(\xi, \eta, \zeta)$

The form function of the 20 nodal points on the indicated element is:

$$\left\{ \begin{array}{l}
 N_i = \frac{1}{8}(1 + \xi_0)(1 + \eta_0)(1 + \zeta_0)(\xi_0 + \eta_0 + \zeta_0 - 2) \\
 \qquad \qquad \qquad (i = 1, 3, 5, 7, 13, 15, 17, 19) \\
 N_i = \frac{1}{4}(1 - \xi^2)(1 + \eta_0)(1 + \zeta_0) \\
 \qquad \qquad \qquad (i = 2, 6, 18, 14) \\
 N_i = \frac{1}{4}(1 - \eta^2)(1 + \zeta_0)(1 + \xi_0) \\
 \qquad \qquad \qquad (i = 4, 8, 20, 16) \\
 N_i = \frac{1}{4}(1 - \zeta^2)(1 + \xi_0)(1 + \eta_0) \\
 \qquad \qquad \qquad (i = 9, 10, 11, 12)
 \end{array} \right. \quad (1)$$

In the formulas,  $\xi_0 = \xi_i \xi$ ,  $\eta_0 = \eta_i \eta$ ,  $\zeta_0 = \zeta_i \zeta$ , and  $\xi_i$ ,  $\eta_i$  and  $\zeta_i$  are local coordinate values of the  $i$  nodal points.

We know from the elastic theory that for the geometric equation of the three dimensional problem the matrix is used to indicate it as:

$$\{\varepsilon\} = [B]\{\delta\} \quad (2)$$

In the formula

Key:  $[B]$  is the matrix of the relationship of the strain and displacement;

$\{\delta\}$  is the displacement vector;

$\{\varepsilon\}$  is the strain vector

Its physical equation, when there is initial strain  $\{\varepsilon_0\}$ , is:

$$\{\sigma\} = [D](\{\epsilon\} - \{\epsilon_0\}) \quad (3)$$

In the formula

Key:  $\{\sigma\}$  is the stress vector;  
 $\{\epsilon_0\} = aT \{111000\}$  ;  
 $T$  is the temperature;  
 $a$  is the material's linear expansion coefficient;  
 $[D]$  is the elastic matrix.

The element has volume force and surface force in simultaneous action and the initial load functional equation caused by the temperature difference is:

$$\Pi^e(u, v, w) = \frac{1}{2} (\{\delta\}^e)^T [K]^e \{\delta\}^e - (\{\delta\}^e)^T \{F\}^e \quad (4)$$

For the whole area, then we have

$$\Pi = \sum_e \Pi^e = \sum_e \left[ \frac{1}{2} (\{\delta\}^e)^T [K]^e \{\delta\}^e - (\{\delta\}^e)^T \{F\}^e \right] \quad (5)$$

In the formula

$\{F\}^e = \{F_0\}^e + \{F_v\}^e + \{F_s\}^e$	is the element's external load (5a) vector;
$\{F_0\}^e = \iiint_{V^e} [B]^T [D] \{\epsilon_0\} dV$	is the element's initial load (5b) vector;
$\{F_v\}^e = \iiint_{V^e} [N]^T \{p\} dV$	is the element's volume force; (5c)
$\{F_s\}^e = \iint_{A^e} [N]^T \{q\} dV$	is the element's surface force; (5d)
$[K]^e = \iiint_{V^e} [B]^T [D] [B] dV$	is the element's stiffness matrix; (5e)

$\{\delta\}$  is the nodal point shift vector;  
 $\{N\} = \{IN_1, \dots, IN_n\}$  etc.

When functional  $\Pi$  uses an extreme value of  $\delta_{\Pi} = 0$ , then we obtain the series of equations required for solution.

### III. Temperature Field

In order to calculate the element's thermal load and thermal stress, it is necessary to calculate the three dimensional temperature field on the blade. Based on the experimental data found in reference [12] concerning geometrical correction along the arc length and mathematical interpolation along the blade height for a certain type of blade we obtained its boundary value. When the boundary conditions were of the first category and third category, the temperature field's elliptic equation and boundary conditions were:

$$\begin{cases} \frac{\partial^2 T}{\partial x^2} + \frac{\partial^2 T}{\partial y^2} + \frac{\partial^2 T}{\partial z^2} = 0 & \text{(in volume V)} \\ T = T_0(x, y, z) & \text{(on surface } A_1) \\ \frac{\partial T}{\partial n} + \eta_0(x, y, z) = q(x, y, z) & \text{(on surface } A_2) \end{cases} \quad (6)$$

In the formula

$A = A_1 + A_2$  is the entire boundary condition;  
 $T_0$  is the known temperature distribution;  
 $\frac{\partial T}{\partial n}$  is the external normal derivative;  
 $\eta_0$  and  $q$  are boundary parameters.

Using the Gauss divergence theorem, we can transform the elliptic equation into a functional extreme value condition:

$$\begin{aligned} \delta\Pi &= \sum_e \{ (\delta T)^T (K_v + K_s) \{T\} - (\delta T)^T \{F\} \} \\ &= \{ \delta T \}^T ( \{K\} \{T\} - \{F\} ) = 0 \end{aligned} \quad (7)$$

In the formula

$$\begin{aligned} \{K_v\}^e &= \iiint_V \{C\}^T (\{J\}^{-1})^T \{J\}^{-1} \{C\} dV && \text{is the volume element contribution to "total stiffness";} \\ \{K_s\}^e &= \iint_A \{N\} \{N\}^T \eta_0 dA && \text{is the surface element contribution to "total stiffness";} \\ \{F\}^e &= \iint_A \{N\} q dA && \text{is the surface element contribution to the right end.} \end{aligned}$$

Due to the arbitrariness of  $\{ \delta T \}$ , formula (7) is equivalent to

$$\{K\} \{T\} - \{F\} = 0 \quad (8)$$

This then is an algebraic system of equations for the element's nodal point temperature.

#### IV. Frontal Solution Method

This is a variation of the Gauss method and its greatest advantages are that its solution accuracy is high and its time is fixed. Moreover, its programming is ingenious so that it can decrease internal memory and make full use of external memory. Its special characteristics in operation are that it both accumulates and eliminates, it does not require the formation of total stiffness and the results after elimination are sent to the external memory and does not occupy internal memory space.

By using fig. 3, it is even easier to explain its solution process. In the fig., when elements ①-⑦ are already accumulated,

element ⑧ is in the process of being carried out and elements ⑨ - ⑮ have not yet accumulated; nodal points with a "\*" symbol have already been eliminated, nodal points with a "0" symbol are in internal memory which is equivalent to the tape width, and nodal points with a "Δ" symbol have still not begun action. Therefore, the activity variable "0" in the solution procedure forms a "wave surface" that continuously advances forward. This is the origin of the frontal method.

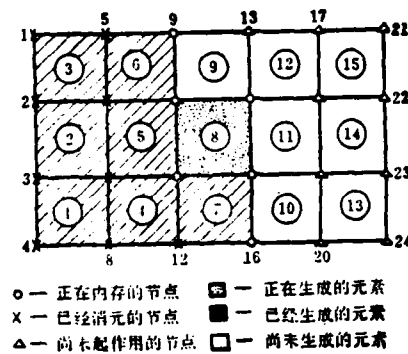


Fig. 3. Schematic Diagram of the Frontal Method

- is a nodal point in the internal memory
- x is a nodal point already eliminated element
- Δ is a nodal point which still has not begun action
- ▨ is an element being produced
- is an element which has already been produced
- is an element which has not yet been produced

It is easy to prove that the internal memory of the frontal method mainly depends on the width of the wave surface and because of this it can economize the internal memory better than the band width method and divided piece tape width method. Tests have proven its obvious advantages for high order systems of equations and high order elements. Its shortcomings are that the program is too complex and when operating, the repetition

of internal and external memory exchange wastes time.

## V. Fitting and Automatic Mesh Division of the Profile's Curved Surface

### 1. Fitting of the Profile's Curved Surface

The body of the blade is surrounded by two skewed space curved surfaces. The contour of the curved surface must be accurate otherwise this will affect aerodynamic performance and engine efficiency.

The divided three dimensional curved surface element must not only have the curved surface strictly coincide with the profile but the element's nodal point coordinate must also accurately fall on the curved surface.

We have test tried a new method proposed in recent years by Coons and Forest [13] using a type of structured curved surface for the fitting of the space curved surface. If the profile is composed of many small curved surface pieces and the interpolation function's second order derivative is continuous in each of the curved surface pieces (as shown in fig. 4), the domain of the bivariable interpolation function  $x(u,w)$  is:  $0 \leq u \leq 1$  and  $0 \leq w \leq 1$ . If we now fix a certain parameter in the  $x(u,w)$  then we obtain the common single variant interpolation function.

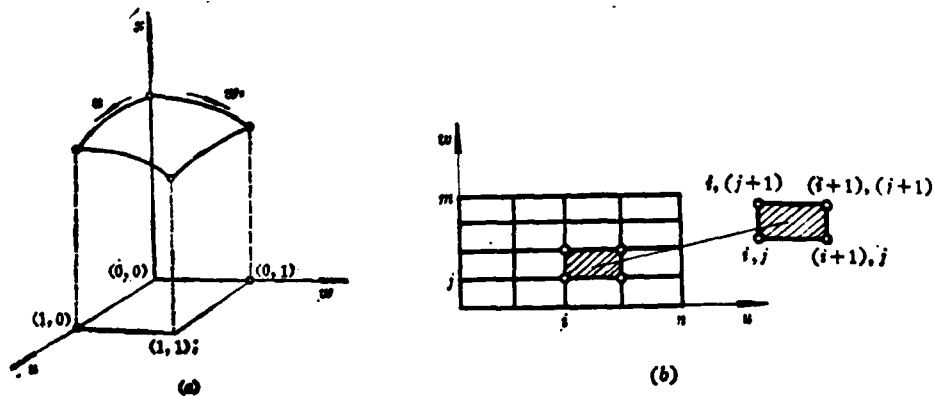


Fig. 4.

Fig. 4. Curved Surface Pieces

When formulating the partial derivative of the second order continuity in the boundary, we write the matrix as:

$$x(u, w) = [F_0(u) \quad G_0(u) \quad F_1(u) \quad G_1(u)]$$

$$\times \begin{pmatrix} x(0, 0) & x_w(0, 0) & x(0, 1) & x_w(0, 1) \\ x_u(0, 0) & x_{uw}(0, 0) & x_u(0, 1) & x_{uw}(0, 1) \\ \hline x(1, 0) & x_w(1, 0) & x(1, 1) & x_w(1, 1) \\ x_u(1, 0) & x_{uw}(1, 0) & x_u(1, 1) & x_{uw}(1, 1) \end{pmatrix} \begin{pmatrix} F_0(w) \\ G_0(w) \\ F_1(w) \\ G_1(w) \end{pmatrix} \quad (9)$$

In the formula, the variable in the 0-1 area is second order continuity and the related symbols are:

$$\begin{cases} F_0(0) = F_1(1) = 1 \\ F_0(1) = F_1(0) = F'_0(0) = F'_0(1) = F'_1(0) = F'_1(1) = 0 \\ G'_0(0) = G'_1(1) = 1 \\ G_0(0) = G_0(1) = G_1(0) = G_1(1) = G'_0(1) = G'_1(0) = 0 \end{cases} \quad (10)$$

$$x_u = \partial x / \partial u \text{ 等 } \quad (11)$$

Key: 1. Etc.

We further define the  $x(u, w)$  in the rectangular area as:  
 $0 \leq u \leq n$ ,  $0 \leq w \leq m$ , and  $n, m$  is the positive integer. Furthermore, taking the  $u_i$  and  $u_j$  values in formula (9) wherein  $i=0, 1, \dots, n, j=0, 1, \dots, m$ , then

$$uw = P(u)B, q^T(w) \quad (12)$$

In the formula:

$$B_x = \begin{array}{|c|c|c|c|c|c|c|} \hline 00 & 00_w & 01 & 01_w & \dots & 0m & 0m_w \\ \hline 00_ & 00_w & 01_ & 01_w & \dots & 0m_ & 0m_w \\ \hline 10 & 10_w & 11 & 11_w & \dots & 1m & 1m_w \\ \hline 10_ & 10_w & 11_ & 11_w & \dots & 1m_ & 1m_w \\ \hline \dots & \dots & \dots & \dots & \dots & \dots & \dots \\ \hline n0 & n0_w & \dots & \dots & \dots & nm & nm_w \\ \hline n0_ & n0_w & \dots & \dots & \dots & nm_ & nm_w \\ \hline \end{array} \quad (13)$$

$$P_k(u) = \begin{cases} F_0(a_i), & (k = i) \\ G_0(a_i), & (k = i + 1) \\ F_1(a_i), & (k = i + 2) \\ G_1(a_i), & (k = i + 3) \\ 0, & \text{其他 (1)} \end{cases} \quad q_l(w) = \begin{cases} F_0(b_l), & (l = j) \\ G_0(b_l), & (l = j + 1) \\ F_1(b_l), & (l = j + 2) \\ G_1(b_l), & (l = j + 3) \\ 0, & \text{其他 (2)} \end{cases} \quad (14)$$

Key: 1. Other  
2. Other

Moreover, there is:

$$\begin{cases} k = 1, 2, \dots, 2n + 2, & l = 1, 2, \dots, 2m + 2, \\ i = 2(u) + 1, & a_i = u - (u), \\ j = 2(w) + 1, & b_j = w - (w), \end{cases}$$

Formula (12) is then the divariant interpolation function defined on the rectangular area of the unit square mesh. Each order of the partial derivative in the  $B_x$  matrix is very difficult to give. Here, we use the smallest second power method to seek  $B_x$  [14].

## 2. Automatic Mesh Division

The form and nodal point coordinate of the element both

utilize automatic mesh division (this only requires the input of a small amount of information). Its process is divided into two steps: first is to determine any transverse tangent plane and divide it into tetrahedrons according to any type of standard, and second is to join the vertical direction to make hexahedron elements.

The cutting up of the transverse tangent plane depends on the shape and position of the cooling holes; for a solid blade, we can cut equally or according to proportion along the arc length; for a hollow circular holed profile, we can use the center of the circle as the basic standard to cut along the circumference; for a specially shaped holed profile, we can make a curved surface fitting similar to that of the outer form because the inner walls of the holes also have curved surfaces. Fig. 5. contains examples of various types of transverse tangent planes.

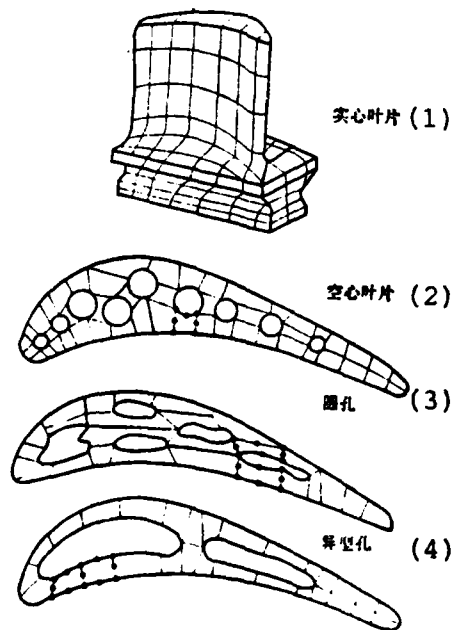


Fig. 5.

Fig. 5. Cut on Profile's Transverse Tangent Plane

- Key: 1. Solid blade  
2. Hollow blade  
3. Circular holes  
4. Specially shaped holes

## VI. Calculation Results

### 1. Assessment of Examples

(1) Using a trapezoidal sheet with varying thickness as the example, we calculated its centrifugal force and aerodynamic distribution load; using a hollow cylinder as the example, we calculated its temperature field and thermal stress; they all had analytical solutions. When we compared it with the calculation results of this method the patterns and data all tallied and satisfied the engineering requirements.

(2) When comparing the calculations of the large twisted blade with the tests, using the semi-solution analytic method of reference [5], this method's error for the large twisted ( $>20^\circ$ ) blade was relatively large. When tested at  $n=17000$  revolutions/minute, we used the direct measurement method yet the surface measured point was not the same as the principal stress direction and thus there was also an error.

As shown in fig. 6., the calculation results of this paper basically fall within the tests and semi-analytic method. Moreover, this method's curve is smooth and is therefore considered believable.

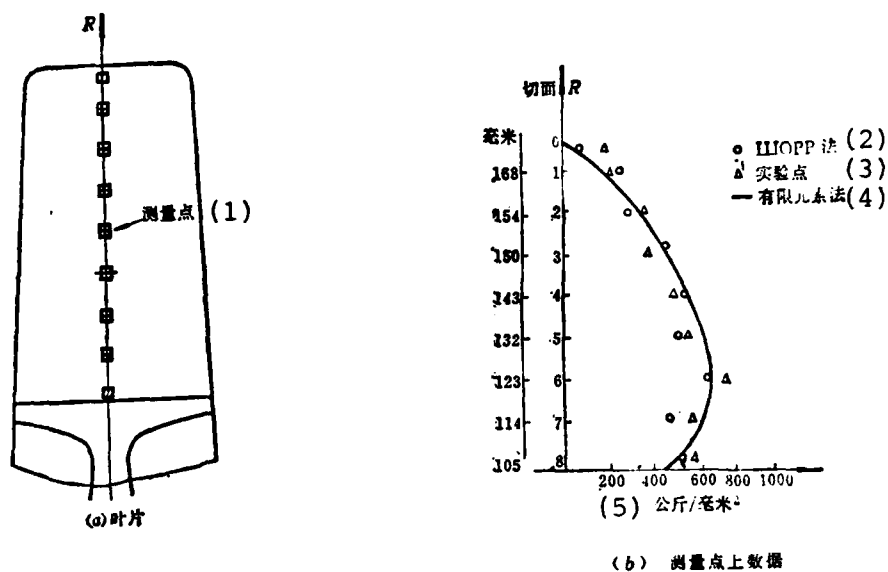


Fig. 6. Test and Calculation Curve of a Large Twisted Blade

- Key: (a) Blade  
 (b) Data on measured points  
 1. Measured point  
 2. Method  
 3. Test point  
 4. Finite element method  
 5. Kilograms/millimeter<sup>2</sup>

## 2. Shrouded Hollow Air-Cooled Blade

### (1) Calculation of centrifugal force

For the calculated objects shown in fig. 1., in order to economize on the internal memory, we used a four holed tangent plane to carry out research. For the stress distribution on this blade's II and IV tangent planes see fig. 7. The high stress area is on the tail edge of the tangent plane and here, besides having a centrifugal force, there is also added a centrifugal bending moment. The stress distribution of the 2,3,4 points on each transverse tangent plane along the blade's high speed direction, as shown in fig. 8., coincides with the results of most

calculation methods. The stress gradients along the sides of each hole are not large. This is because the axis line of the cooling holes are basically the same as the direction of the centrifugal force and the added bending moment is very small. Naturally, the stress value near the small holes is greater than that of the large holes. The stress value on the shroud is then very small and the shroud is equivalent to adding a concentrated mass load on the wingtip.

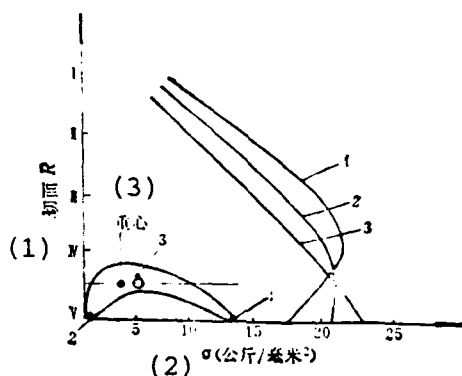


Fig. 8. Stress Distribution Along Blade Height

Key: 1. Tangent plane R  
 2. (Kilograms/millimeter<sup>2</sup>)  
 3. Center of gravity

(2) Aerodynamic force

The blade's stress distribution caused by aerodynamic force is basically identical to the stress distribution pattern on a varying thickness blade. Yet, in an actual turbine cascade, the aerodynamic force changes the blade's leading and trailing edges as well as the blade height direction. It requires the use of a three dimensional flow field for calculation because it is difficult to accurately give the aerodynamic boundary value. This, then, effects the accuracy of stress calculations.

(3) Here, we will only give the temperature field for the II and IV tangent planes as shown in fig. 9. As regards the

temperature distribution of each cooling hole side, the cooling effect of the large holes is better than that of the small holes. The temperature changes along the periphery of each hole is not large, yet the normal temperature gradient changes on the side of the holes is large. The temperature difference between the side of the holes and the profile's outer surface is about  $300^{\circ}\text{C}$ . The high temperature area is on the leading edge of the profile and the tail edge location because the leading edge comes in direct contact with the gas flow and the tail edge's dissipation of heat is difficult; the heart shape of the blade becomes a low temperature area, the temperature on the outer surface is relatively high, the temperature field along the height of the blade is related to the temperature and flow quantity of the air-cooled gas flow, and the temperature on the side of the blade hole is close to the temperature of the air-cooling gas flow. The curves in fig. 10. are the temperature changes of points 1,3,2 from the blade root to the blade tip. Their temperature changes are all about  $250^{\circ}\text{C}$  and the shape of each line is similar; the temperature on the blade tip's tail edge is very high and this seems true for most turbine blades. Cracks and excessive thermal burning are often produced in this local position.

#### (4) Thermal stress

The changes of the thermal stress field are basically identical to the change patterns of the temperature differences. The thermal stress on each tangent plane in the side edge of the air-cooling holes and outer surface is very high. Although the temperature on the side of the hole is not high yet it very easily produces cracks. The temperature on the tail edge of the blade which is very high lowered the material's permissible stress value. In brief, a relatively high temperature gradient area causes the thermal stress gradient to also be relatively high.

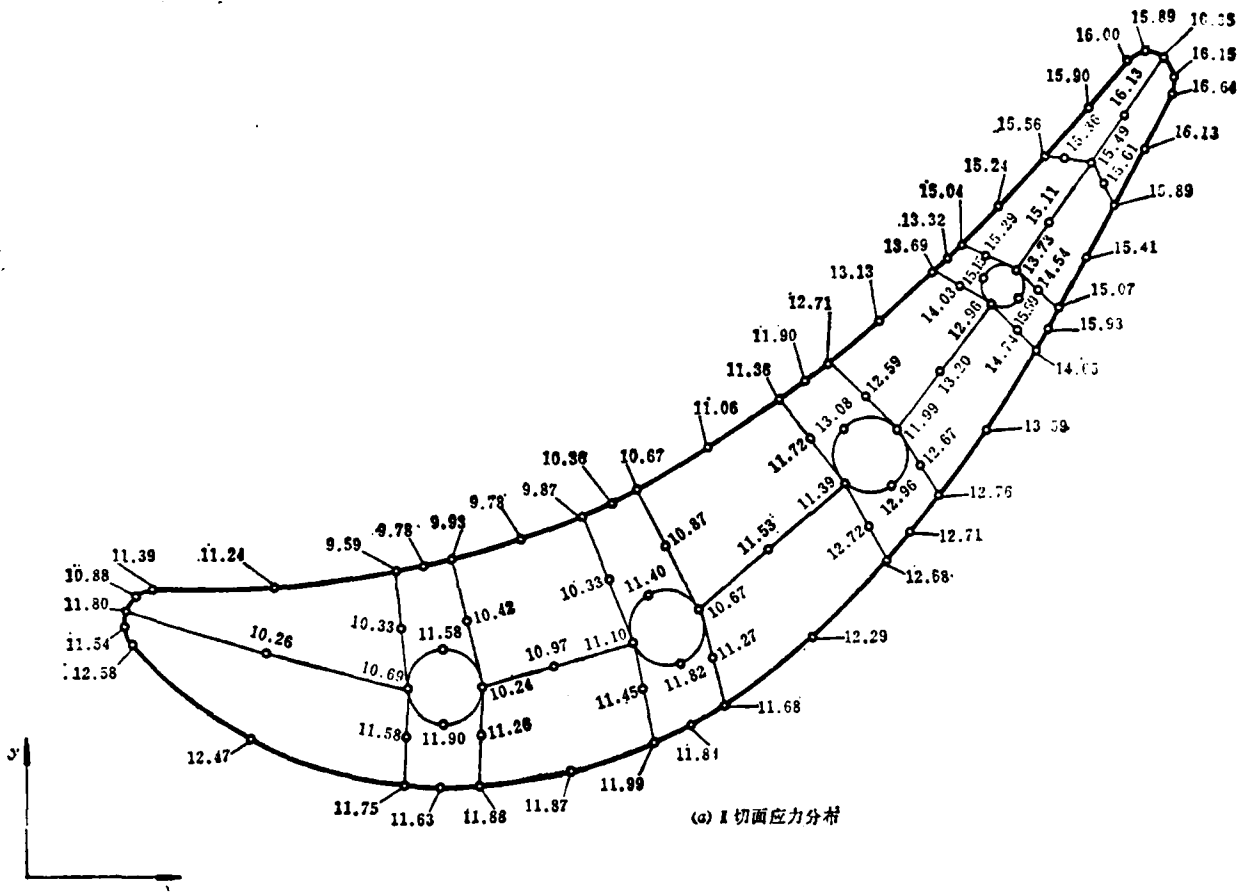
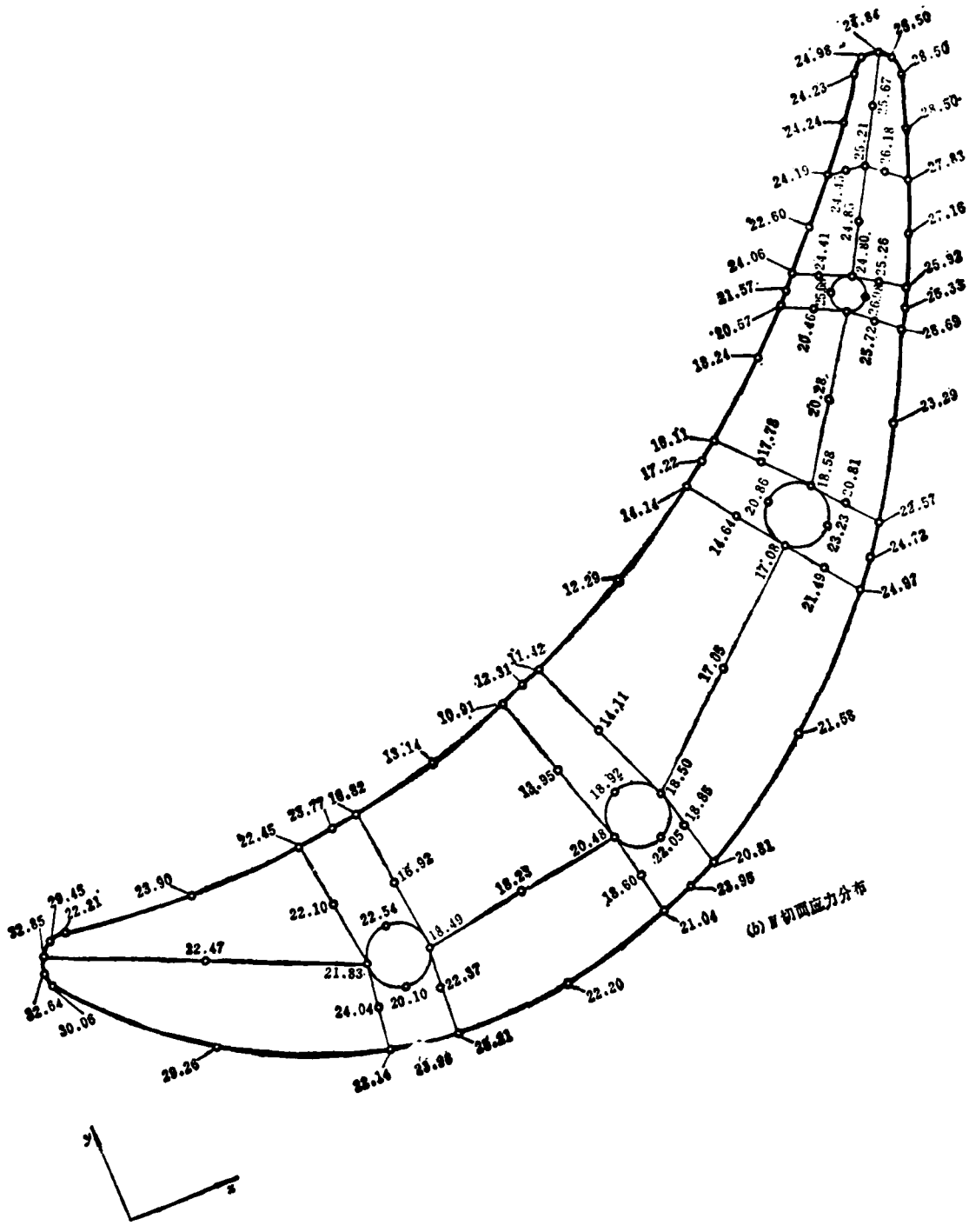


Fig. 7. Stress distributions of tangent planes I and IV  
 Key: (a) Stress distribution of tangent plane I.



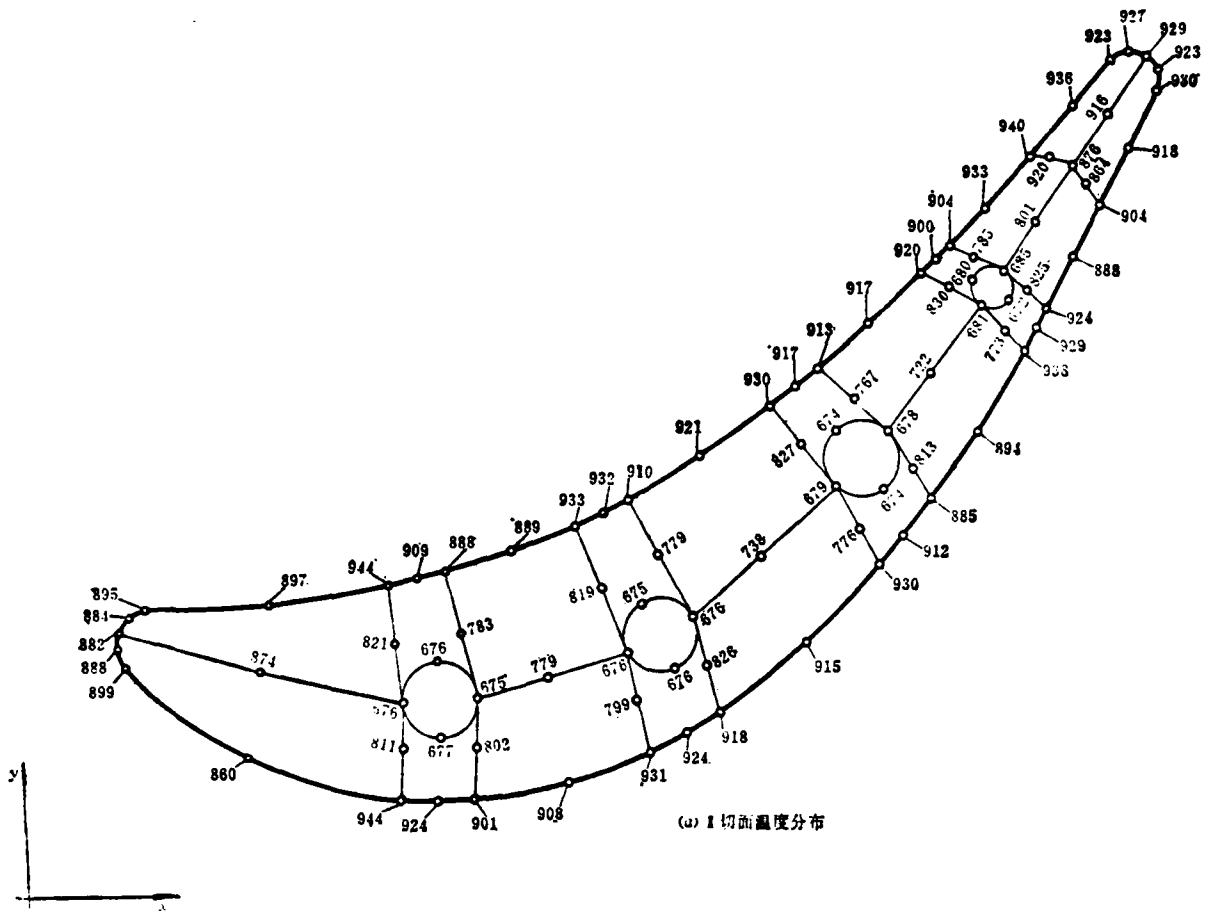


Fig. 9. Temperature distribution of tangent planes I and IV.  
 Key (a) Temperature distribution of tangent plane I.

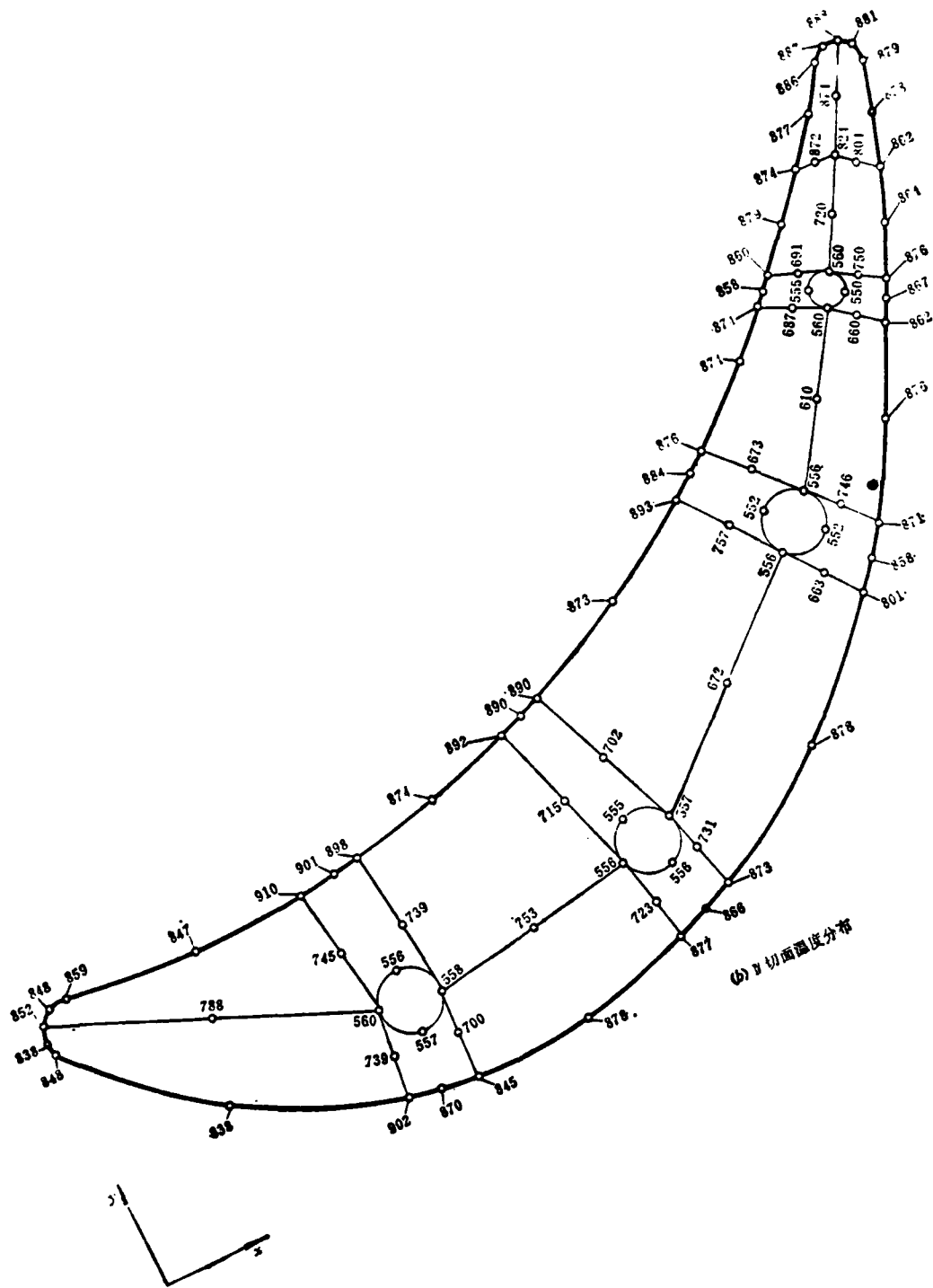


Fig. 9. Key:  
Key: (b) Temperature distribution of tangent plane IV.

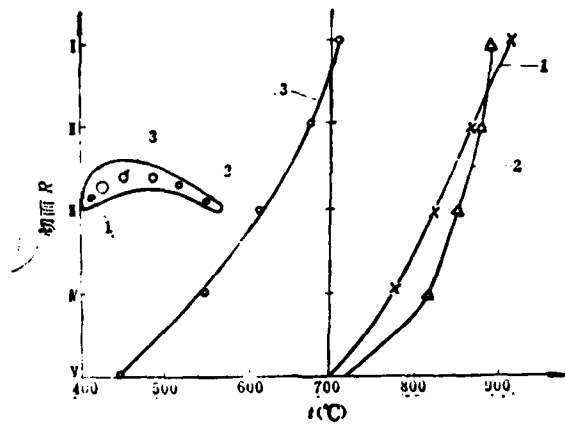


Fig. 10. Temperature Distribution Along Blade Height

Key: 1. Tangent plane R

#### References

1. O.C. Zienkiewicz, "The Finite Element Method in Engineering Science", McGraw-Hill New York, 1971
2. B.M. Irons, "A Frontal Solution Program for Finite Element Analysis", Int. J. for Num. Meth. in Engineering, Vol.2, p5-32, 1970.
3. Coons, AD-663504.
4. Shomatsu Shōri, "The Use of the Finite Key Factor Method for the Calculation of the Thermal Stress of an Air-Cooled Blade", NAL-TR-481, 1976.
5. E.F. Shorr, "Calculation of the strength of naturally twisted blades", MAI, 1954, 2.
6. C.W. Hayes, " Turbine Vane Ceramic and Wall", J. Aircraft, Vol.12, No. 4, 1975, 4.
7. M.T. Loferski, "Turbine Airfoil Life Prediction by Mission Analysis", J. Aircraft, Vol. 12, p400, 1975.
8. W. Johnson and P.B. Meyer, The Plastic Theory, Shanghai Scientific Publishers, 2965.
9. Tetsuma Shinka, "The Plastic Theory", Scientific Publishers, 1976.

References (continued)

10. Hua Dong Hydraulics College, "The Finite Element Method for the Problem of Elastic Hydraulics", Feb., 1977.
11. Dong Ping and J.N. Ruisaituosi (transliteration), tr. by Xiong Changbing etc., "The Finite Element Method - the Basic Technique and Calculation Method", 1979,8.
12. "Research Report on the High Temperature Turbine Air-Cooled Blade", Three Machine Bureau No. 628, Dec., 1973.
13. Chang, Gengzhe, "Introduction to the Coon's Curved Surface", Dec. 1977.
14. Xiao Junxiang and Yu Guoshan, "The Curved Surface Fitting and Numerical Control Processing of the Compressor Blade Space Form Surface, Science and Practice, 1976.
15. Fang Dezhi, "Differential Geometry", People's Education Publishers, 1964.
16. Xiong Changbing and Ziao Junxiang, "Three Dimensional Stress Analysis For a Shrouded Hollow Air-Cooled Blade", Beijing Institute of Aeronautics and Astronautics Research Grant", 1979,9.
17. "Three Dimensional Stress Analysis Program Specification for a Shrouded Hollow Air-Cooled Blade", Science and Practice, 1979.

## A STUDY OF THE METHODS FOR MEASURING RADAR'S ECCM PERFORMANCE

Li Nengjing  
(PLA Air Force Laboratory)

### Abstract

This article reviews the methods for measuring radar's ECCM capabilities and points out a set of commonly used measuring formulas. The basic parts of these formulas which are composed from the radar's principal technical parameters represent the radar's potential ECCM capabilities. The supplementary parts of the formulas which are composed from the indices of the radar's various ECCM technical measures represent the quality level of these ECCM measures. The use of this set of formulas can calculate the expressed numerical values of the radar's anti-passive jamming capabilities, anti-active jamming capabilities and integrated ECCM capabilities. This paper gives examples and discusses the application of the calculation results for radar systems analysis and overall design.

### I. Preface

Radar's ECCM capability is one of the most important functions of radar yet up to the present there is still not a commonly used measuring method.

In the past, there were two commonly used means of expressing radar's ECCM capabilities. One was the listing of the radar's various ECCM technical measures and their performance indices. For example, whether the radar could quickly convert its

frequency, how wide is its frequency conversion band, whether the radar has moving target indication (MTI) and how much is its visible coefficient in the complex waves (SCV) etc. This type of expressed formula is not only overelaborate but the ECCM measure items and index itself are not able to accurately measure the radar's real ECCM capabilities. Taking the radar's anti-passive jamming capabilities as an example, it is related to the SCV value as well as the radar's resolution or pulse volume.

The second type of formula is the use of the level of the radar's check or measurement performance decline under specific interference backgrounds to show the radar's ECCM capabilities. For example, under a specific interference power spectrum density, how far the radar's defense was, how much the radar's tracking precision of a certain target decreased, etc. The numerical values obtained from this type of formula which are connected to the interference conditions and target characteristics cannot independently evaluate the radar's ECCM capabilities.

J. L. Johnston suggested the use of the ECCM improved factor EIF to indicate the radar's ECCM performance [1]. The definition of the EIF is

$$EIF = \frac{(S/J)_k}{(S/J)_o} \quad (1)$$

In the formula,  $(S/J)_o$  is the radar's output signal interference power ratio before adopting ECCM measures;  
 $(S/J)_k$  is the radar's output signal interference power ratio after adopting ECCM measures.

This formula is suitable for various types of interference and ECCM measures and its universality is relatively strong. Yet, it is only suitable for measuring the above type of radar ECCM measures on the integrated ECCM performances of several types

of ECCM measures but cannot measure the entire radar system's ECCM capabilities. Because of certain technical parameters of radar, for example the transmission power and antenna gain, they are obviously not able to belong to the radar's ECCM measures yet they determine the fundamental factors of the entire radar's ECCM capabilities.

Because of this, we attempted to find a new method to measure the radar's ECCM capabilities. The demands for this were: first, to only rely on the radar's technical parameters; second, having universality, it could measure the radar's capabilities to counter various major types of interference. Based on these demands, in 1978 for the first time I proposed an expression formula for radar integrated ECCM capabilities, that is:

$$P T_0 B_1 G F_A F_S [2] \quad (2)$$

In the formula

P is the radar's mean emission power;  
 $T_0$  is the radar's observation time of the target;  
 $B_1$  is the radar system's instantaneous band width;  
G is the radar antenna's gain;  
 $F_A$  is the radar antenna's quality factor;  
 $F_S$  is the radar signal's quality factor.

This paper will further prove and investigate this method.

## II. An Analysis of the Interference Type and the Fundamental Measures of Radar's ECCM to Bring Forth an Expression Method for Radar's ECCM Capabilities

In order to bring forth an expression method for radar's ECCM capabilities, we first observed the radar's fundamental ECCM measures. See table 1.

Table 1.

Type of Interference	Radar's Fundamental ECCM Measures
<p>1. Emission type interference (active jamming)</p> <p>(1) Inhibition such as noise interference or other modulation wave form interference.</p> <p>(2) Deceiving such as response jamming.</p>	<p>(a) Increase the radar's signal power.</p> <p>(b) Cause a difference between the radar's signal carrier frequency and interference - resolved from the frequency.</p> <p>(c) Raise the radar antenna's orientation - resolved from the space direction angle.</p> <p>(d) Have the generally best filter so as to find the greatest output signal interference power. Use a matching filter for white noise interference; then join the most effective filter of this type of interference wave form for the non-white noise interference - resolved from the signal wave form.</p> <p>(a) Design a complex radar signal so that the jammer finds it difficult to duplicate - resolved from signal wave.</p> <p>(b) Design a radar operations system so that the interrelation between the radar signal wave and space direction angle are smallest (dealing with angle deception response interference).</p>
<p>2. Reflection interference (passive jamming) such as interference tinsel cord and non-man made surface features, clouds and rain, and ocean waves.</p>	<p>(a) Use different speeds for the radar target and interference complex wave (the Doppler frequency), signal selected from complex waves - resolved from frequency.</p>

Type of Interference	Radar's Fundamental ECCM Measures
3. Absorbing interference such as electromagnetic absorption coating.	<p>(b) Raise the radar antenna orientation and reduce the radar signal time width so as to decrease the strength of the received complex wave, - that is, raising the resolution for the space direction angle and time.</p> <p>(a) Enlarge the radar signal power.</p>

From an analysis of the above brief table, besides the special demands for dealing with angle deception response interference with signal wave form and space direction angle, there are two basic radar measures for ECCM: one is power and the other is resolution. Because of this, it can be inferred that by using the radar's power parameter and resolution parameter, we can indicate the radar's fundamental ECCM capabilities.

To represent the radar power's technical parameters, we should use the radar's mean transmission power  $P$ .

The radar's resolutions, for example those mentioned in table 1, have the aspects of frequency, space directional angle, time and signal wave form. From the signal analysis theory it can be known that, in essence, the wave forms resolution is the resolve of the signal in the time domain and frequency domain. Because of this, the radar's resolution is mainly concerned with four areas of overall resolution: the time domain, frequency domain, space directional angle and angle of elevation.

Without the simple parameters, we can still express the

radar's integrated resolution. Yet, we know that the radar four dimension blur function brought forth by H. Urkowitz [3] can describe, on a relatively wide foundation, the integrated resolution of radar in space, time domain and frequency domain.

The function is:

$$A(t_d, f_d, \theta_d, \phi_d) = \iiint_{-\infty}^{\infty} U^*(f) U(f - f_d) F^*(\theta, \phi) F[(\theta - \theta_d) \times (\phi - \phi_d)] e^{-i2\pi t_d f} df d\theta d\phi \quad (3)$$

In the formula,

$U(f)$  is the radar signal's envelope complex frequency spectrum;

$F(\theta, \phi)$  is the radar antenna's direction figure;

$t_d$  and  $f_d$  are the time difference and frequency difference;

$\theta = \sin \alpha$  is the sine value of directional angle  $\alpha$ ;

$\phi = \sin \varepsilon$  is the sine value of elevation angle  $\varepsilon$ ;

$\theta_d$  and  $\phi_d$  are the difference of  $\theta$  and the difference of  $\phi$ .

When the antenna band width is far greater than the signal band width so that there is no apparent interaction between the antenna and signal,

$$A(t_d, f_d, \theta_d, \phi_d) = A(t_d, f_d) A(\theta_d, \phi_d) \quad (4)$$

This is the product of the four dimensional blur function which can be expressed as the signal blur function and the antenna direction blur function. Formula (4) is applicable for most

radar.

The signal blur function  $A(t_d, f_d)$  is:

$$\begin{aligned} &= \int_{-\infty}^{\infty} U^*(f)U(f-f_d)e^{-j2\pi f t_d} df \\ &= \int_{-\infty}^{\infty} u(t)u^*(t+t_d)e^{j2\pi f t_d} dt \end{aligned} \quad (5)$$

In the formula,  $u(t)$  is the signal's envelope time function.

The antenna direction blur function  $A(\theta_d, \phi_d)$  is:

$$= \iint_{-\infty}^{\infty} F^*(\theta, \phi)F((\theta-\theta_d), (\phi-\phi_d))d\theta d\phi \quad (6)$$

This function is the self correlation function of the antenna direction figure. Because most of the radar antenna direction figure is close to the  $\text{sinc}_c$  function, the self correlation function of the  $\text{sinc}_c$  function is still the  $\text{sinc}_c$  function. Because of this, the antenna direction figure is close to its self correlation function. We can use the antenna direction figure to substitute for the antenna direction blur function.

In order for the resolution to be able to be expressed by a parameter, we used the main peak of blur function modular value  $|A|$  when it decreased to a specified range. For example, when it decreased to the main peak and the highest value (after normalizing this value was 1) was -6 decibels, the width of the main peak (when the blur function is one dimensional), or the sectional area (when the blur function was two dimensional),

or sectioned volume (when the blur function is even more multi-dimensional) acts as the parameter. This parameter can be called the resolution unit.

We call the sectional area of the two dimensional blur function  $|A(t_d, f_d)|$  whose main peak decreased 6 decibels the radar signals distance and frequency integrated resolution unit. The sectional area of the antenna direction figure  $|F(\theta, \phi)|$  whose peak decreased 6 decibels is called the radar antenna's space angle resolution unit.

It is inferred from this that the four dimensional volume obtained when the four dimensional blur function  $|A(t_d, f_d, \theta_d, \phi_d)|$  main peak decreased 6 decibels can be defined as the radar's integrated resolution unit. When  $R_T$  is used to represent this value, the larger the  $R_T$ , the more error shown for the radar's integrated resolution. Therefore, the precise description of the radar resolution parameter is  $\frac{1}{R_T}$ .

Radar's basic measure for anti-passive jamming is raising the radar's resolution. Therefore, the description of the parameter of the radar's integrated resolution  $(\frac{1}{R_T})$  can be used to express the radar's basic anti-jamming capabilities.

Radar's basic methods for anti-inhibitory active jamming are to increase the energy of the target echo as much as possible, decrease the interference power coming in from the antenna as much as possible and filter out the interference that has already been transmitted in so that the power ratio of the output signal and interference will be maximal. To realize these, we must rely on radar with great emission power and at the same time depend on radar with high resolution. If the latter's emission power can be concentrated on the target, then both the

interference input and output will decrease. Therefore, the product of the power parameter and resolution parameter which is  $(P/R_T)$  can be used to express the radar's basic anti-active jamming capabilities.

As regards the response type interference, besides having specially interrelated demands, we can also depend on the radar's high resolution. As regards absorption interference, it is also necessary for the emission power to be concentrated on the target. This is identical to dealing with active jamming. From a wide general perspective, the product of the power and resolution parameter  $(P/R_T)$  can be used to express the radar's fundamental integrated ECCM capabilities in dealing with various types of interference.

Yet, the calculation of the  $R_T$  numerical value is complex and an inferred simplified formula should be substituted.

Firstly, we established formula (4) for most radar and because of this,

$$|A(t_s, f_s, \theta_s, \phi_s)| = |A(t_s, f_s)| |A(\theta_s, \phi_s)| \quad (7)$$

In this way,  $R_T$  is then equal to the four dimensional volume formed from the 3 decibel modular value sectional surface of the signal's blur function and the 3 decibel modular value sectional surface of the antenna direction blur function.

There are three types of radar signal blur function modular value forms (abbreviated as the three dimensional blur figure): nail board form, thumbtack form and knife-edge form [4-5].

When the radar signal is a pulse train, the three dimensional

blur figure of the signal is a nail board form. If this pulse train includes  $N$  pulses, the width during each pulse is  $r$ , frequency width is  $B_s$ , pulse repetition period is  $T$  and the pulse train's sustained time is  $T_0 = NT$ .

There are two forms of this type of signal blur function modular value with a 3 decibel sectional surface (abbreviated as the blur plane figure):

(1) The pulse itself is a simple pulse or phase coded pulse and signal plane blur figure as shown in fig. 1.

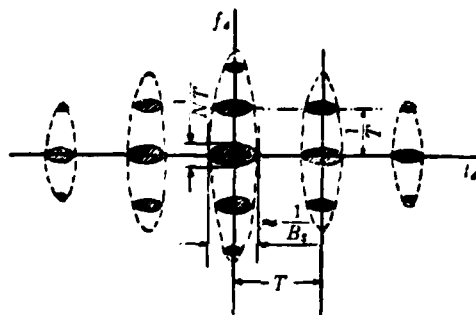


Fig. 1. Simple Pulse Train and Plane Blur Figure of Phase Coded Pulse Train

(2) The pulse itself is a linear frequency modulation pulse and signal plane blur figure as shown in fig. 2.

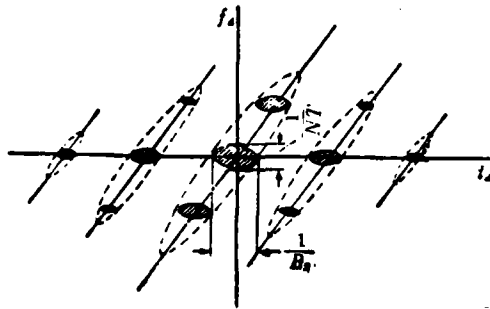


Fig. 2. Plane Blur Figure of Linear Frequency Modulation Pulse Train

We know from figures 1 and 2 that the approximate value of this type of signal blur function modular value main peak with a 3 decibel sectional area is:

$$\frac{\pi}{4} \frac{1}{NT} \frac{1}{B_s} = \frac{\pi}{4} \frac{1}{T_s B_s}$$

When the radar signal is formed by a single relatively long pseudohatted code, then the three dimensional blur function of this type of signal is a thumbtack form. Its plane blur figure is shown in fig. 3.

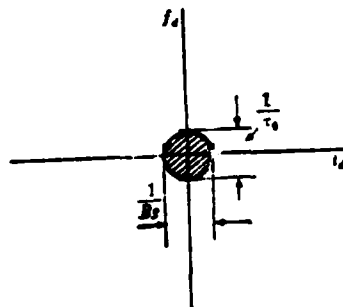


Fig. 3.

Fig. 3. Plane Blur Figure of a Single Pseudohatted Code Signal;  
 $\tau_0$  is the Total Length of the Signal

From fig. 3 we know that the approximate value of this type of signal blur function modular value main peak with a 3 decibel sectional area is:

$$\frac{3}{4} \frac{1}{\tau_0} \frac{1}{B_s} = \frac{3}{4} \frac{1}{T_0 B_s}$$

Given that at this time the signal's sustained time is  $T_0$ , then the total length of the code is  $\tau_0$ .

When the radar signal is a single linear frequency modulation pulse, the three dimensional blur figure of the signal is a knife-edge form. See fig. 4 for its plane blur figure.

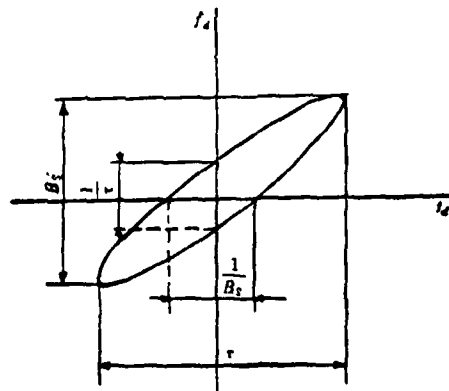


Fig. 4 Plane Blur Figure of a Single Linear Frequency Modulation Pulse

This type of signal can only accurately determine the combined value of an unknown target's distance and speed. This combined value is the oblique axis in the plane blur figure. Yet,

we cannot precisely know what the distance and speed are. Therefore, at the least, during actual application we must transmit a pair of linear frequency modulation signals. This pair of signals have opposite linear frequency modulation slopes as shown in fig. 5.

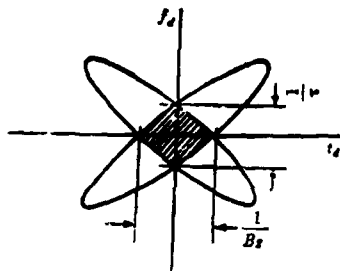


Fig. 5. Plane Blur Figure of a Pair of Linear Modulation Frequency Pulses

At this time, a target will produce two echos on the indicator; the intermediate value of the two echos is the accurate distance and the interval of the two echos represents the target's speed. The equivalent plane blur figure of the radar signal composed by this pair of linear frequency modulation pulses is the overlapping part of the two directional slope ellipse which is the oblique line part in fig. 5. This area is approximately equal to  $\frac{1}{2} \times \left( \frac{1}{T} \quad \frac{1}{B_s} \right)$ . When considering  $T_0 = 2T$ , then this area is equal to  $\frac{1}{T_0 B_s}$ .

We know from the above analysis that the value of the commonly used radar signal blur function modular value main peak with a 3 decibel sectional area is:

$$k \frac{1}{T_0 B_s}$$

(\*)

In the formula,  $k_A$  is the coefficient and its approximate value is  $3/4 \sim 1$ .

The antenna direction blur function can use the antenna direction figure for an approximation. Therefore, the approximate value of the antenna direction blur function modular value main peak with a 3 decibel sectional area is:

$$\frac{\pi}{4} \alpha_0 \varepsilon_0 \quad (9)$$

In the formula,  $\alpha_0$  and  $\varepsilon_0$  are the 3 decibel widths of the antenna direction figure's directional angle and elevation angle.

Thus, we can now obtain the approximate value of  $R_T$ :

$$R_T \approx \left( k_A \frac{1}{T_0 B_s} \right) \left( \frac{\pi}{4} \alpha_0 \varepsilon_0 \right) = \frac{\pi k_A}{4} \frac{\alpha_0 \varepsilon_0}{T_0 B_s} \quad (10)$$

Because the antenna gain  $G$  can be approximately expressed as:

$$G = \frac{\pi^2}{\alpha_0 \varepsilon_0} \quad (11)$$

Therefore

$$R_T \approx \frac{k_A}{4 \pi} \frac{1}{T_0 B_s G} \quad (12)$$

Because the constant coefficient is of no importance it can be eliminated in normalization and therefore the radar's integrated resolution parameter  $\left( \frac{1}{R_T} \right)$  can be simplified and expressed as  $T_0 B_s G$ .

Using  $\left(\frac{P}{R_T}\right)$ , the expressed radar fundamental integrated ECCM capabilities can be simplified as:

$$PT_B G \quad (13)$$

### III. The Expression of Radar Fundamental ECCM Capabilities Derived From the Signal's Interference Power

The expression of radar's fundamental ECCM capabilities obtained in the last section can also use another method which is derived from the radar's transmitted signal interference power ratio.

If  $\left(\frac{S}{C}\right)_i$  represents the power ratio of a radar target signal and passive jamming in a radar input area and  $\left(\frac{S}{C}\right)_o$  represents the power ratio of the radar's output signal and passive jamming, then

$$\left(\frac{S}{C}\right)_i = \frac{\sigma_t}{\sigma_c} \quad (14)$$

In the formula

$\sigma_t$  is the target's radar sectional area;

$\sigma_c$  is the radar sectional area of the passive jamming.

$$\sigma_c = \frac{1}{2} c^2 R_c^2 \Omega \eta_o \quad (15)$$

In the formula,

$c$  is the electric wave propagation speed;

$R_c$  is the distance from the passive jamming area center to the radar station;

$\Omega$  is the three dimensional angle value of the radar antenna direction figure;

$\eta_o$  is the reflex coefficient of the passive jamming.

Because

$$\Omega = \frac{4\pi}{G}$$
$$\tau \approx \frac{1}{B_s}$$

Therefore

$$\left(\frac{S}{C}\right)_i = \frac{\sigma_s B_s G}{2\pi c \eta_0 R_s^2} \quad (16)$$

and

$$\left(\frac{S}{C}\right)_o = I \left(\frac{S}{C}\right)_i \quad (17)$$

In the formula, I is the modified factor.

If the speed distribution of the interference object is basically uniform, its Doppler frequency band width is  $B_c$ , its signal frequency band width is  $B_s$ ,  $B_s \ll B_c$  and the two are overlapping, then the theoretical value of I is  $\frac{B_c}{B_s}$ . In

real situations, if the interfering frequency band and signal band are possibly not overlapping or not completely overlapping then we can define  $B_c$  as the equivalent interference band width which is:

$$B_s = IB_s \quad (18)$$

We already know that

$$B_s \approx \frac{1}{T_s} \quad (19)$$

and therefore

$$I = \frac{B_s}{B_s} \approx \frac{B_s}{\frac{1}{T_s}} = B_s T_s \quad (20)$$

Because of this

$$\left( \frac{S}{C} \right)_s = \frac{\sigma_t B_s T_s B_s G}{2\pi c \eta_0 R_c^2} = k_1 (T_s B_s G) \quad (21)$$

In the formula,

$$k_1 = \frac{\sigma_t B_s}{2\pi c \eta_0 R_c^2} \quad (22)$$

It is composed by the constant coefficient  $2\pi c$  and target parameter  $\sigma_t$  as well as the interference conditions  $\eta_0$  and  $R_c^2$ .

When deciding the size of the radar output signal-interference ratio in passive jamming, we also decided that the radar's technical parameter for the anti-passive jamming capabilities size is  $T_s B_s G$ . This is a simplification of the radar integrated resolution parameter  $\frac{1}{R_r}$  derived in the last section.

Let us take a further look at the situation of anti-inhibition active jamming.

Letting  $\left(\frac{S}{J}\right)_o$  represent the output signal interference power ratio when the radar receives active jamming and if the interference power spectrum is basically uniform (this is a relatively common interference condition), then the radar selected and signal matched receiver at this time is:

$$\left(\frac{S}{J}\right)_o = \frac{E_s}{P_{JR}/B_s} = \frac{E_s B_s}{P_{JR}} \quad (23)$$

In the formula,

$E_s$  is the energy of the target's echo signal;

$P_{JR}$  is the received interference power.

Therefore

$$E_s = \frac{PT_o G^2 \lambda^2 \sigma_t}{64\pi^3 R_t^4} \quad (24)$$

In the formula,

$\lambda$  is the radar's wavelength;

$R_t$  is the distance between the target and the radar station.

$$P_{JR} = \frac{P_J G_J A_r(\theta) Y_J}{(4\pi R_t^2)^2} \quad (25)$$

In the formula,

- $P_J$  is the jammer's reflection power;
- $G_J$  is the jammer's antenna gain;
- $A_r(\theta)$  is the radar antenna's equivalent receiving area for the interference direction;
- $\gamma_J$  is the polarization coefficient;
- $R_J$  is the distance between the jammer and the radar.

If the jammer's location direction is basically the same as the target, then

$$A_r(\theta) = \frac{G\lambda^2}{4\pi} \quad (26)$$

After substituting in formula (25):

$$P_{JK} = \frac{P_J G_J \gamma_J \lambda^2 G}{(4\pi)^2 R_J^2} \quad (27)$$

When formulas (24) and (27) are substituted into formula (23):

$$\left(\frac{S}{J}\right)_0 = \frac{\sigma_r P T_0 B_s G}{4\pi \left(\frac{R_s^2}{R_J^2}\right) P_J G_J \gamma_J} = k_s (P T_0 B_s G) \quad (28)$$

In the formula,

$$k_2 = \frac{\sigma_t}{4\pi \left(\frac{R_t^4}{R_J^4}\right) P_J G_J Y_J} \quad (29)$$

It is composed of target parameters  $\sigma_t$  and  $R_t$ , and interference conditions  $P_J, G_J, Y_J$  and  $R_J$ .

Therefore, when deciding the size of the radar output signal interference ratio under active jamming, we also decided that the radar's technical parameter for anti-active jamming capabilities size is  $PT_0 B_s G$ . This is a simplification of the radar power and resolution parameter product  $\left(\frac{P}{R_T}\right)$  derived in the previous section.

Now we will take a further look at the radar output signal-interference ratio condition when two types of interference exist simultaneously. Let  $\left(\frac{S}{J+C}\right)$  represent the output signal-jamming ratio.

$$\begin{aligned} \left(\frac{S}{J+C}\right)_0 &= \frac{1}{\left(\frac{J}{S}\right)_0 + \left(\frac{C}{S}\right)_0} = \frac{1}{k_1 T_0 B_s G + k_2 P T_0 B_s G} \\ &= k_2 \left[ \frac{1}{1 + \left(\frac{k_2}{k_1}\right) P} \right] (P T_0 B_s G) \end{aligned} \quad (30)$$

If

$$\left(\frac{k_2}{k_1}\right) P \ll 1 \quad (31)$$

Then

$$\left(\frac{S}{J+C}\right)_0 \approx k_2 (PT_0 B_s G) \quad (32)$$

which is the same as when there is only active jamming.

When we employed a representative technical parameter to calculate the value of  $\left(\frac{k_2}{k_1}\right)$ , we could prove that formula (32)

is established in a rather wide range. Therefore, formula  $PT_0 B_s G$  not only expressed the radar's fundamental anti-active jamming capabilities but it was also able to express the radar's integrated fundamental ECCM capabilities for anti-passive jamming and anti-active jamming.

#### IV. Supplementary Factors for the Fundamental Expression

The already derived radar fundamental ECCM capabilities expression measures the radar's fundamental or potential ECCM capabilities. If we want to measure the radar's ECCM capabilities more completely it is also necessary to have the usefulness or quality level of the radar's various ECCM measures act as supplements. Below we will mention a group of supplementary factors.

##### 1. Quick Changing Carrier Frequency

Because the radar's integrated four dimensional blur function only takes into consideration the signal's complex envelope and has not yet considered the radar's carrier frequency, it only expresses the resolution of the signal carrier frequency when in a static state. The changes of the carrier frequency are often used in the radar ECCM measures to resolve the signal and active jamming. Yet, these changes must be quick changes within the pulse or within a small group of pulses to be able to shake off

an enemy location's track jamming and force the enemy to use wide frequency band jamming. Because the total power of an enemy's jammer is fixed or limited, the jamming power spectrum enlarges  $k_j$  times, the jamming power density then drops  $k_j$  times and the radar's output signal jamming power ratio then rises  $k_j$  times. Because of this, the quick change measures of the carrier frequency are equal to raising the radar's transmission power to  $k_1$  times.

The radar allows the maximum range of its carrier frequency quick changes to be the radar system's instantaneous band width  $B_1$ . Naturally, radar designers have made every effort to reach:

$$k_1 = \frac{B_1}{B_s} \quad (33)$$

Therefore, after the radar has quick changing frequency measures, the expression of the radar's anti-active jamming capabilities should add a supplementary  $k_1$  factor.

## 2. Side Lobes

When we defined the radar's integrated resolution parameters we only considered the sectional volume when the integrated blur function main peak decreased 6 decibels. Because of this, the corresponding signal blur function and antenna direction figure also only considered its main peak 3 decibel area. Yet, there are many side peaks around the main peak and they influence the ECCM capabilities within a fixed range. This will be discussed below.

When the present microwave radar antenna direction figure main peak (commonly called the antenna beam main lobe) is very sharp-pointed, the active jamming carried out from the side peak (commonly called side lobe or secondary lobe) is already the principal jamming method of the radar against the enemy.

The side lobe level has already become a technical index for measuring the radar's ECCM capabilities. Therefore, in the expression of our measuring the radar's anti-active jamming capabilities, it is necessary to introduce the supplement factory  $G_s$  to represent the radar antenna's side lobe level.

We defined factor  $G_s$  as:

$$G_s \text{ (decibel)} = 10 \lg \left( \frac{\text{(antenna power direction figure (main lobe peak value))}}{\text{(antenna power direction figure (maximum secondary lobe peak value))}} \right) - 25 \quad (34)$$

Defining it in this way takes into consideration the present radar technical level. The antenna's main side lobe power ratio of 25 decibels can be viewed as a medium level representative value. When it is higher than 25 decibels this represents the antenna's high grade design which causes the  $G_s$  to have a positive value. On the contrary, when it is lower than 25 decibels this represents a poor design causing the  $G_s$  to have a negative value. This type of method is used to cause the  $G_s$  factor to influence the numerical value of the original anti-active jamming capabilities fundamental expression.

The  $G_s$  only has one value for the needle-shaped beam. The  $G_s$  should include two factors for the fan-shaped beam, that is, a horizontal side lobe factor  $G_{SH}$  and a vertical side lobe factor  $G_{SV}$ . These two factors are separately added after calculating formula (34).

$$G_s = G_{SH} + G_{SV} \quad (35)$$

When the radar has an offsetting device, the offsetting benefits should be added into  $G_s$ . Sometimes when the radar signal's blur function is in a relatively distant area of its

main peak there exist many relatively high branch peaks (also called grating lobes) and side peaks (also called side lobes) near the main lobe.

The branch lobes or grating lobes usually lie in the time domain of the radar's sustained interference and outside of the frequency domain. Here, we will put off discussion on this temporarily.

The signal side lobe is a signal processing circuit which must be inhibited. Its disadvantage lies in a weak signal producing interference near a strong signal. Yet, it is different from the antenna beam side lobe in that it does not belong to a hostile interference entrance. The demands for the inhibited signal side lobes also do not resemble the antenna side lobes direct columns which are the radar's ECCM performance. Because of this, we do not take the signal side lobe inhibition as an ECCM factor for calculations.

### 3. Signal Processing

The radar resolution described by the radar blur function indicates the potential abilities of the radar's resolve signal and if the potential abilities are realized it is still necessary to adopt measures in signal processing. Firstly, the radar receiver should be a matching wave filter because the radar signal's blur function is essentially formed from a group of different Doppler frequency target echos which pass through the output wave combination of a matching wave filter within the same period of time [4,5]. Yet, the radar does not necessarily use an integrated matching wave filter. For example, generally in dealing with passive jamming the radar does not use a Doppler frequency shunt circuit matching wave filter but after it is in a single circuit matching wave filter it connects the MTI circuit. Further, in order to deal with non-white noise type active jamming it is also necessary to connect special

filters. The quality and anti-jamming usefulness of these signal processing circuits are supplementary factors which we must consider.

Firstly, we will consider the quality of the MTI. B.D. Steinberg has already defined quality factor I for measuring the quality of the MTI's technical measures [6],

$$I = \frac{\text{MTI output signal stray wave power ratio}}{\text{MTI input signal stray wave power ratio}} \quad (36)$$

SCV is often used in a radar technical performance expression to substitute for I. The value of SCV is 6 decibels lower than I.

In the anti-passive jamming capabilities expression, we defined a moving target to indicate quality factor  $P_M$ :

$$P_M(\text{decibels}) = \text{SCV} - 25 \quad (37)$$

Taking the constant 25 decibels, we first consider that it is able to represent the canonical level of the modern radar MTI visibility coefficient SCV and at the same time cause it to be convenient for memory and use with the previous side lobe factor constant.

Second, the signal processing factor which must be considered is a constant false alarm processing quality factor.

The derivation of the radar's integrated resolution formula takes the radar's receiving system linearity as a basis. If the strength of the signal, interference or both surpasses the dynamic range of the radar's receiving system, this causes the receiving system to be saturated or obstructed and the radar's resolution

to decrease drastically. Because of this, the constant false alarm is a necessary radar measure for various types of anti-jamming.

Therefore, the action of the constant false alarm processing in the anti-jamming is anti-saturation and after constant false alarm processing the signal interference ratio has a loss. Because of this, we defined the constant false alarm processing supplementary factor in the radar's ECCM capabilities expression as:

$$\rho_f^{(1)}(\text{分贝}) = 10 \lg \left( \frac{\Delta M}{L_{CF}} \right) - 25 \quad (38)$$

Key: 1. (Decibels)

In the formula,

$\Delta M$  represents the allowable increased multiple in the radar receiving system's dynamic range after adding in the constant false alarm processing device;

$L_{CF}$  represents the constant false alarm loss;

The selected theorem of constant 25 decibels is from the same previous formula.

Noise frequency modulation jamming is the often encountered wide band noise type active jamming. In order to deal with this type of interference, modern radar has already made wide use of Dicke-Fix (i.e. wide-limited-narrow circuit). We defined the Dicke-Fix supplementary factors for the anti-active jamming capabilities as:

$$\rho_N^{(1)}(\text{分贝}) = (EIF)_{\nu} - 8 \quad (39)$$

Key: 1. (Decibels)

#### 4. Antenna Polarization

The radar's comprehensive resolution discussed previously

did not include the influence of antenna polarization. Therefore, it is necessary to further analyze the polarized resolution. Theoretically speaking, because the radar target's scattered echo and outside interference are completely independent, the polarization states can never be the same. Because of this, they can be used to cause the antenna to, as best as possible, have polarization matching for the useful echo signals and exert the mismatched method for the interference to obtain ECCM results. Yet, in reality, it has good results for rain and cloud interference.

Because raindrops are nearly circular, most of its reverse scattering for the circular polarized waves are reverse rotational circular polarized waves but aircraft and other complex man-made targets are not like this. Therefore, the use of a circular polarized antenna or an antenna whose polarization can be randomly adjusted can benefit a signal-interference ratio of 10-20 decibels. Yet, complex structured natural objects which produce interfering complex waves, for example surface object complex waves, are not able to obtain this benefit.

As regards man-made interference, if active jamming comes from a jammer or passive jamming object which possesses relatively uniform scattered polarization characteristics (for example, interference tinsel cords hanging down all assume a horizontal state), then the use of a polarized adjustable antenna or the polarization offset method can have very good ECCM results. Yet, in an electronic war, the enemy actually takes precautions against these measures. Its jammer is usually a pair of simultaneously started machines which separately transmit two types of opposite polarized waves. Its put in interference wire is also designed to hang down with one half horizontal and the other half vertical. Because of this, under actual countermeasure conditions, the radar antenna feed polarization

which can be adjusted can only benefit 3 decibels. If the radar does not have this changeable polarization measure, the  $W_s$  value is 0.

#### 5. Dealing with Response Type-Interference

There are several different types of situations in which response type interference disturbs radar.

Repetitious entering from the secondary lobes is usually used for search radar. This causes response pulses, disturbance and useful hidden target signals on many locations and at different distances on the indicator frame. The measures for dealing with this type of interference are mainly inhibiting the antenna side lobes and causing the radar to have repeated frequency chatter.

For tracking radar, the response type interference mainly has gate pulling and counter-modulation angle deception. The counter measures for the former are wave form differentiation and repeated frequency chatter. The basic measures for the latter are using a signal wave form and space direction angle non-interrelated operating system; for example, the single pulse goniometer system.

We have already discussed wave form resolve and antenna side lobe isotopes previously.

The repetition frequency chatter measure is already being widely used in modern radar. Besides counter response type interference, it is also able to inhibit a nearby station's synchronic interference and is also able to overcome the blind speed of the MTI technique. As regards the signal's three dimensional blur figure, its action causes the branch peak of the nail board form blur function to lower and the lowered multiple

is equal to the numeral  $J$  of the chatter changes. Shown on the radar's reception terminal, it also surpasses the periodic response signal's lowered output power  $J$  times. For this, we defined the repetition frequency chatter measure's supplementary factor for the radar's ECCM capabilities as:

$$\rho_j^{(1)}(\text{分贝}) = 10 \lg J - 8 \quad (40)$$

Key: 1. (Decibels)

By taking a constant 8 decibels, because the modern radar  $J$  is commonly 5 to 7, 8 decibels represents all levels. At the same time, it is also identical to formula (39) and is thus easy to remember.

The reason that the counter modulation angle deception interference can start operating is that the radar's useful signals are interrelated on the wave form and antenna space direction angle. Previously, when we deduced the radar's integrated resolution parameter, it was assumed that the signal wave form and antenna directional angle were not interrelated. Because of this, the obtained radar ECCM capabilities expression did not include this element and thus awaits further research.

#### V. Summary and Calculation Examples

We will sum up in table 2 the radar's ECCM capabilities expression proven above.

	(1) 抗消极干扰能力 (AC)	(2) 抗积极干扰能力 (AJ)	(3) 综合抗干扰能力 (AJC)
(4) 基本表达式	$T_0 B_S G$	$PT_0 B_S G$	$PT_0 B_S G$
(5) 补充因子			
(6) ① 快速频率因子		$k_f$ [见(23)式] (16)	$k_f$
(7) ② 边瓣因子		$G_S$ [见(34)式] (17)	$G_S$
(8) ③ 活动目标质量因子	$\rho_M$ [见(37)式] (14)		$\rho_M$
(9) ④ 恒虚警因子	$\rho_F$ [见(38)式] (15)	$\rho_F$	$\rho_F$
(10) ⑤ 宽-限-窄电路因子		$\rho_N$ [见(39)式] (18)	$\rho_N$
(11) ⑥ 天线极化因子	$W_S$	$W_S$	$W_S$
(12) ⑦ 重复频率抖动因子		$\rho_J$ [见(40)式] (19)	$\rho_J$
(13) 全 式	$T_0 B_S G W_S \rho_M \rho_F$ (20) 或 $T_0 B_S G F_{AC} F_{SC}$ ( $F_{AC} = W_S$ , $F_{SC} = \rho_M \rho_F$ )	$PT_0 k_f B_S G G_S W_S \rho_F \rho_N \rho_S$ (21) 或 $PT_0 B_I G F_A F_{S_I}$ ( $F_A = G_S W_S$ , $F_{S_I} = \rho_F \rho_N \rho_J$ )	$PT_0 k_f B_S G_S W_S \rho_M \rho_F \rho_N \rho_S$ (22) 或 $PT_0 B_I G F_A F_S$ ( $F_A = G_S W_S$ , $F_S = \rho_M \rho_F \rho_N \rho_J$ )

Table 2

- Key:
1. Anti-passive jamming capabilities (AC)
  2. Anti-active jamming capabilities (AJ)
  3. Integrated anti-jamming capabilities (AJC)
  4. Fundamental expression
  5. Supplementary factor
  6. Quick changing frequency factor
  7. Side lobe factor
  8. Moving target quality factor
  9. Constant false alarm factor
  10. Wide-limited-narrow circuit factor
  11. Antenna polarization factor
  12. Repetition frequency chatter factor
  13. Whole expression
  14. See formula (37)
  15. See formula (38)
  16. See formula (23)
  17. See formula (34)
  18. See formula (39)
  19. See formula (40)
  20. Or
  21. Or
  22. Or

It can be seen that the radar's ECCM capabilities expression has two parts. The first is the fundamental part. This part

measures a radar's fundamental or potential ECCM capabilities determined by its major technical parameters. Its significance is similar to other radar fundamental measurement formulas in wide use at the present. For example, the fundamental measurement formula of search radar force is the power and antenna aperture product  $PA$ ; further, the fundamental measurement formula for the accurate tracking radar's goniometric angle precision is the power, antenna aperture and (antenna gain)  $[2]$  product  $PAG[2]$  [7].

The second is the supplementary factors part. This part shows the radar's ECCM measures and their quality level. Within this part those factors belonging to the antenna aspect can be jointly called antenna quality factor  $F_A$  (only the part that acts on the passive jamming is  $F_{AC}$ ). Those belonging to the signal aspect are jointly called signal quality factor  $F_S$  (those that act on passive jamming are  $F_{SC}$  and those that act on active jamming are  $F_{SJ}$ ).

By combining the fundamental part and supplementary factors part we can obtain: anti-passive jamming capabilities expression  $AC = T_o B_o G F_{AC} F_{SC}$ ; anti-active jamming capabilities expression  $AJ = P T_o B_o G F_A F_{SJ}$ . These two formulas form an approximately direct ratio with the radar's corresponding output signal interference power ratio. In the formulas, each factor cannot compensate for the other.

Finally we have the combined anti-jamming capability expression  $AJC = P T_0 B_1 G F_A F_S$ . This formula can broadly and generally indicate the overall capability of radar to resist various types of jamming but is not directly proportional to the radar signal and overall jamming power ratio. In the formula, the various factors cannot compensate for each other.

Now, we will discuss the measuring method for a multichanneled radar's ECCM capabilities.

Many radar systems consist of multiple channels and they are divided into several different categories:

(1) Each channel has a different carrier frequency, yet the space beams are the same or overlapping; for example, frequency diversity system radar.

(2) Each channel's carrier frequency is identical, yet the space beam positions are different or only have partial overlapping. For example, pulse system radar and some three coordinate radar.

(3) Each channel's carrier frequency is different and the space beam positions are also different or only have partial overlapping; for example, some three coordinate radar.

For each channel's ECCM capability measurement formula, as was already shown above, we calculate the whole radar system's ECCM capability and consider them separately according to three categories of conditions.

For the frequency diversity radar which belong to category (1), one channel receives interference while the other channels still operate normally. If all the channels receive interference then the whole system is inhibited. Because of this, the system's anti-active jamming capacity is:

$$(AJ)_s = \sum_{i=1}^n (AJ)_i \quad (41)$$

In the formula,  $n$  is the channel's total. If each channel's carrier frequency differs greatly and do not belong to the same frequency band then the systems anti-passive jamming capability is:

$$(AC)_s = \sum_{i=1}^n (AC)_i \quad (42)$$

Yet, in all situations, each channel carrier frequency still belonged to the same frequency band. At this time:

$$(AC)_s = (AC)_{i_{max}} \quad (43)$$

In the formula,  $(AC)_{i_{max}}$  represents the largest one in each channel  $(AC)$ . Using the system's integrated ECCM capability calculation method, the above analysis should be the same as the anti-active jamming capability. Therefore it is defined as:

$$(AJC)_s = \sum_{i=1}^n (AJC)_i \quad (44)$$

For the category (2) multiple beam radar system, when one space beam receives interference the other independent beams still operate. Because of this, the system's anti-active jamming capability is:

$$(AJ)_s = k_R \sum_{i=1}^n (AJ)_i \quad (45)$$

In the formula,  $k_R$  represents the overlapping coefficient of the partial overlapping condition in the beam. If each beam has an independent  $k_R=1$  and if there is a partial overlapping of  $k_R < 1$  then when we previously defined the radar's space directional angle resolution and took the antenna beam's 3 decibel angle width as the resolved unit, if the space two beams are overlapping below 3 decibels this can be viewed as the fundamental independence, taking  $k_R=1$ . With the same reasoning, the system's anti-passive jamming capability is:

$$(AC)_s = k_k \sum_{i=1}^n (AC)_i \quad (46)$$

The system's integrated ECCM capability is:

$$(AJC)_s = k_k \sum_{i=1}^n (AJC)_i \quad (47)$$

For the category (3) systems, the anti-active jamming capabilities are the same as formula (41). As regards the anti-passive jamming capabilities, we observe whether or not each channel's carrier frequency belongs to the same frequency band and use formula (42) or (46). The system's integrated ECCM capabilities are still based on formula (44).

Below we will calculate and compare four types of radar ECCM capabilities according to each of the above mentioned formulas. They are: two new models, the three coordinate radar AN/TPS-43E (manufactured by Westinghouse Company of the U.S.) and AR-3D (manufactured by Bendix Company of the U.S.); two older search radar A and B types (see table 3).

(1) 需 达 系 统	(2) 备 注					
	(3) 型	(4) 号	(5) 号	(6) 号	(7) 号	(8) 号
	多波束6通道	抑制制8通道	多波束5通道	抑制制4通道	雷达系统各通道	
	三坐标雷达	三坐标雷达	二坐标雷达	二坐标雷达	功率与天线增益	
	AN TPS-43E	AR-3D	甲	乙	丙	丁
(9) 总发射功率(千瓦)	5	10	4	1.6	(35)	
(10) 第一通道天线增益 $G_1$ (分贝)	38.5	41.5	42.5	39.3	前三种系统的第一通道, 即波束仰角最低通道	
(11) 第一通道发射功率 $P_1$ (千瓦)	1.1	3.2	0.8	0.4	前二种是估计值 (36)	
(12) 发射损耗(分贝)	4	6	2	4	估计值 (37)	
(13) 雷达信号带宽 $B_s$ (兆赫)	1	10	1	1		
(14) 信号持续时间 $T_0$ (秒)	0.03	0.028	0.02	0.03		
(15) $T_0 B_s G_1$ (分贝)	83.3	96.0	85.5	84.1		
(16) $P_1 T_0 B_s G_1$ (分贝瓦)	109.8	124.7	112.5	106.1	已扣除发射损耗 (38)	
(17) 补充因子, $k_f$ (分贝)	23	0	0	0	后三种雷达系统都无捷变频 (39)	
(18) $G_{SH}$ (分贝)	-4	0	-5	-3		
(19) $G_{SV}$ (分贝)	-2	-2	-5	-5		
(20) $G_s$ (分贝)	-6	-2	-10	-2		
(21) $W_s$ (分贝)	0	0	0	0	均无极化可调整措施 (40)	
(22) $k_M$ (分贝)	-2	-4	-25	-7	甲型无MTI (41)	
(23) $k_N$ (分贝)	-8	-8	-2	-8	均无Dicke-Fix (42)	
(24) $P_F$ (分贝)	0	0	-25	-25	前二种是估计值甲、乙型 均无CFAR (43)	
(25) $P_I$ (分贝)	0	0	-8	-3	前二种是估计值甲、乙型 均无重复频率抖动措施 (44)	
(26) 抵消极干扰补充因子总计 (分贝)	-2	-4	-50	-32		
(27) 累积极干扰补充因子总计 (分贝)	9	-10	-51	-49		
(28) 补充因子总计(分贝)	7	-14	-76	-56		
(29) 第一通道抵消极干扰能力 $(AC)_1$ (分贝)	81.5	92	35.5	52.1		
(30) 第一通道抗累积干扰能力 $(AJ)_1$ (分贝瓦)	118.8	114.7	61.5	57.1		
(31) 第一通道综合抗干扰能力 $(AJC)_1$ (分贝瓦)	116.8	110.7	36.5	50.1		
(32) 系统抵消极干扰能力 $(AC)_s$ (分贝)	86.5	92.1	41.3	52.1		
(33) 系统抗累积干扰能力 $(AJ)_s$ (分贝瓦)	123.4	119.5	67.3	63.1		
(34) 系统综合抗干扰能力 $(AJC)_s$ (分贝瓦)	121.4	115.5	42.3	56.1		

Table 3

Table 3.

- Key:
1. Radar system
  2. Remarks
  3. Type
  4. Multiple beam 6 channel three coordinate radar AN/TPS-43E
  5. Frequency scanning system 8 channel three coordinate radar AR-3D
  6. Multiple beam 5 channel two coordinate radar A type
  7. Frequency diversity system 4 channel two coordinate radar B type
  8. Radar system with each channel's power and antenna gain (see table 4)
  9. Total emission power (kilowatts)
  10. The first channel's antenna gain  $G_1$  (decibels)
  11. The first channel's emission power  $P_1$  (kilowatts)
  12. Emission loss (decibels)
  13. Radar signal band width  $B_s$  (megahertz)
  14. Signal's continuous time  $T_o$  (seconds)
  15.  $T_o B_s G_1$  (decibels)
  16.  $P_1 T_o B_s G_1$  (decibel watts)
  17. Supplementary factors:  $k_J$  (decibels)
  18. (decibels)
  19. (decibels)
  20. (decibels)
  21. (decibels)
  22. (decibels)
  23. (decibels)
  24. (decibels)
  25. (decibels)
  26. Anti-passive jamming supplementary factors total (decibels)
  27. Anti-passive jamming supplementary factors total (decibels)
  28. Supplementary factors total (decibels)
  29. First channel's anti-passive jamming capability (AC) (decibels)
  30. First channel's anti-active jamming capability (AJ)<sub>1</sub>, (decibel watts)
  31. First channels integrated ECCM capability (AJC), (decibel watts)
  32. System's anti-passive jamming capability (AC)<sub>s</sub>, (decibels)

33. System's anti-active jamming capability (AJ)<sub>s</sub>, (decibel watts)
34. System's integrated ECCM capability (AJC)<sub>s</sub>, (decibel watts)
35. The first channels of the first three types of systems are the beam's lowest elevated angle channel
36. The first two types are estimated values
37. Estimated value
38. Emission loss already deducted
39. The latter three types of radar systems do not have quick changing frequencies
40. All are non-polarized adjustable measures
41. B type without MTI
42. All without Dicke-Fix
43. The first two types are estimated values of the A and B types which are without CFAR
44. The first two types are estimated values of the A and B types which are without repetition frequency chatter measures

(1) 雷达名称	TPS-43E				AR-3D				甲 (2) 型				乙 (3)				
(4)	(5) 通道号	R <sub>max</sub>	G	P	其他 (6)	R <sub>max</sub>	G	P	其他 (7)	R <sub>max</sub>	G	P	其他 (21)	R <sub>max</sub>	G	P	其他 (16)
各通道的作用	1	1	1	1		1	1	1	(8) 有 MTI	1	1	1		1	1	1	无 (17)
距离 R <sub>max</sub> , 天线增益 G, 反射功率 P, 相互比例关系	2	0.9	0.8	1		1	1	1	(9) 无	1	1	1		1	1	1	无 (18)
	3	0.8	0.64	1		0.9	1	0.66	(10) 无	1	1	1		1	1	1	无 (19)
	4	0.6	0.36	1		0.7	1	0.21	(11) 无	0.7	0.5	1		1	1	1	无 (20)
	5	0.4	0.25	0.4		0.55	1	0.09	(12) 无	0.5	0.25	1					
	6	0.3	0.25	0.15		0.45	1	0.04	无 (13)								
	7					0.4	1	0.025	无 (14)								
	8					0.3	1	0.008	无 (15)								

Table 4 The General Characteristics of Each Channel for Four Types of Radar

Key: 1. Name of radar  
 2. A type  
 3. B type

4. The operational distance for each channel is  $R_{\max}$ , the antenna gain is  $G$ , the reflection power is  $P$  and there is a mutual proportion relationship
5. Channel number
6. Other
7. Other
8. With MTI
9. Without
10. Without
11. Without
12. Without
13. Without
14. Without
15. Without
16. Other
17. With MTI
18. Without
19. Without
20. Without
21. Other

It can be seen from the calculation results that because the AR-3D signal band width is large and its antenna gain is high, its anti-passive jamming capability is about 6 decibels higher than that of the TPS-43E. Yet, because the AR-3D does not have quick changing frequency capability, its anti-active jamming capability is actually about 4 decibels lower than the latter. It is worth noting that the AR-3D systems anti-passive jamming capability only increases 0.1 decibels as compared to the first channel. Besides the first channel, this is due to the other channels not having MTI circuits.

As regards the two older types of search radar, the numerical values calculated from their fundamental ECCM abilities expression are not low and are actually close to those of the first two types of three coordinate radar. This shows that their ECCM potential capabilities are strong. Yet, because they basically do not add any ECCM technical measures or only have very few measures, the supplementary factors are all relatively high negative values and the final calculated ECCM capability

expressed numerical values are much lower than those of the three coordinate radar. Their performance in an interference environment drops drastically and their difference from modernized radar is very obvious. On the other hand, in view of their possessing very strong ECCM potential capabilities, if we carry out technological innovations and add necessary ECCM technical measures then we can remake it so that it possesses ECCM capabilities close to those of modernized radar. We can adopt formula calculations to obtain the increased numerical value index of their ECCM capabilities.

Now we can sum up the major uses of the radar's ECCM capabilities measurement formula which we obtained as follows:

(1) We can use the radar's own technical parameters to measure the numerical value indices of the radar's anti-passive jamming capabilities, anti-active jamming capabilities and integrated ECCM capabilities. This is convenient for making comparisons between various types of radar or between various types of design plans for certain radar.

(2) Because the anti-passive jamming capability expression and anti-active jamming capability expression are approximately in direct ratio to the output signal's interference power ratio under corresponding interference conditions, we can take their calculated numerical values and directly use them to compare and calculate the levels of surveyed location performance decreases for the various plans of various types of radar or one type of radar in an interference environment.

(3) The radar's ECCM capabilities expression includes the fundamental and supplementary factors parts. Because of this, we can separately calculate the radar's potential ECCM capabilities and the effects of the radar's ECCM technical measures. For certain radar we can use this analysis in design or in technological innovation to increase the investment-result ratio of certain complex ECCM measures.

Finally, it should be pointed out that when the same radar is in different operational conditions (for example, search or tracking conditions), if its technical parameters or channel numbers are different then the ECCM capabilities numerical values calculated according to the formulas will be different.

#### References

1. S.L. Johnson, ECCM Improvement Factors(EIF), International Countermeasures Conference, 1976.
2. Li Nengjing: Measuring Method for Radar's ECCM Capabilities, Acta Aeronautica et Astronautica Sinica, no. 1 (1979), pp. 70-81.
3. H. Urkowitz, C.A. Hauer and J.F. Koval, Generalized Resolution in Radar Systems, Proc.IRE. 50, No. 10, Oct. 1962, pp. 2093-2105.
4. A.W. Lihaijieke (? romanization): The Radar Resolution Theory, Scientific Publishers, 1973.
5. Zhang Zhizhong: The Selection and Processing of Radar Signals, Defense Industries Publishers, 1979.
6. B.D. Steinberg, Signal Enhancement by Linear Filtering in Pulse Radar, Lectures 20-22 of special summer course, University of Pennsylvania (June, 1961).
7. D.K. Barton, Real-World Radar Technology, The Record of the IEEE 1975 International Radar Conference, pp. 1-22.

### Abstract

This article reviews the commonly used methods for expression of radar's ECCM performance, points out their disadvantages and proposes that it is required to establish the formulae which consist only of the radar's technical parameters in order to measure the radar's ECCM capabilities.

By means of logical argumentation and ambiguity function theory we can derive the followings: (1) The radar's 4-dimensional generalized resolution parameter can be used to express the radar's basis anti-clutter capability. The simplified expression of this parameter is  $T_0$  (the dwelling time at a radar's target, or the integration time of a echo signal of the radar)  $\times B_s$  (the radar signal bandwidth)  $\times G$  (the radar antenna gain); (2) The product of an average radar's transmitting power and its generalized resolution parameter  $PT_0 \times B_s G$  can be used to express the radar's anti-jamming capability, and the same formula may also be used to express the total interference rejection capability in gross.

By another approach, i.e. by calculation of the radar's output signal to interference power ratio under various interference conditions, the given formulae have further been proven.

The given formulae consisting of the radar's fundamental parameters are the fundamental parts of the measuring formula of the radar's ECCM capabilities. They represent the radar basic or potential ECCM performance. The supplementary factors for the ECCM capability formulae are composed of the technical specifications of the radar's ECCM devices. The general rule of composition is to take the typical quality level (or the middle level) specification (in db) as the base figure. If the quality level of some devices is higher, a positive factor will be got, and if lower—a negative. For example, the equation for MTI supplementary factor  $\rho_M$  is

$$\rho_M(\text{db}) = \text{SCV} - 25(\text{db})$$

where 25 db is the middle level specification for SCV of modern MTI radar.

As many radar systems consist of multiple channels, in this article we propose a set of equations for the multichannel radar system's ECCM capabilities in terms of the ECCM capabilities of the individual channel.

In the last part of this article, 4 radar systems are taken as examples, their ECCM capabilities are calculated by means of the given formulae. Application of obtained results to radar's system analysis and system design are discussed.

BRIEF REPORT ON THE FIRST FLIGHT TEST RESEARCH ACADEMIC  
EXCHANGE MEETING

The Chinese Aeronautics and Astronautics Institute convened China's first flight test research academic exchange meeting from December 16-21, 1980 at Yantai in Shandong Province. The conference was prepared and managed by the Test Flight Institute. Attending the conference were 28 representatives from related units and 77 authors of papers from China. Among these, besides the engineers and technicians, there were also pilots with long term test flight experience.

At the conference, 74 papers were exchanged. The contents were concerned with the flight test theories, methods, test techniques, flying techniques and testing techniques of aircraft, dynamic devices, electronics, special designed air conditioning and aviation armaments. The conference was divided into three stages. The first stage was a general meeting exchange and besides exchanging seven papers, two special reports were given. The second stage was divided into three sets of exchanges: aircraft, dynamic devices, and electronic, special designs and test instruments. Altogether, 44 papers were read (another 23 written papers were exchanged). The third stage consisted of specialized discussions of problems dealing with the advance of flight test research, promoting academic exchange and establishing related academic organizations. From beginning to end the conference was very conscientious, enthusiastic and pervaded with a friendly atmosphere.

The conference had abundant content, wide specialized fields and strong real practice which caused everyone to broaden their outlook, increase their knowledge and attain to great gains. Everyone considered that this indicated China's flight test research enterprises were going from the stage of having studied and comprehended foreign test flight theory and methods and were beginning to enter a stage in which China was initiating its own independent new creative research. The representatives each requested that this type of academic meeting be convened in the future.

During the conference, they discussed existing problems in China's present test flight research, proposed establishing corresponding academic organizations and chose a name list for the preparatory group of the academic organizations. The convening of the second academic exchange meeting during the third quarter of next year by the Flight Mechanics Alliance was also decided at the conference.

## AIMING COMPUTATION FOR FIGHTER WEAPON AIMING SYSTEM

Zhang Sen  
(Optic Machinery Research Institute)

### Abstract

This paper presents several derivations of the aiming computing equations for the "Non-Director" (also called "Disturbed Recticle") system in the aiming computer systems of the air-to-air gunsight and head-up display weapon. This paper deals with four situations: the fighter attacks a non-maneuverable target which is considered as moving in a straight line at a constant speed; the fighter attacks a maneuvering target and the corrections for the maneuvering of the target are taken into account in the aiming computation; the fighter attacks a maneuvering target and the corrections for the maneuvering of the target and the effect of the fighter's own roll rate are also taken into account in the aiming computation; during the attack of the fighter on a maneuvering target the historical tracer line (hot line) and a version of the damped tracer line based on multiple Lcos computations are adapted in the computation for air-to-air gun snap-shot.

### Symbols

M target point  
M<sub>y</sub> target leading point  
 $\xi$  bullet's oblique firing length  
 $\bar{n}$  ballistic lowering quantity  
 $\bar{D}$  target distance

$\dot{\bar{D}}, \ddot{\bar{D}}$	distance change rate and distance change acceleration
$\bar{V}_0$	commencing speed of muzzle
$\bar{V}_1$	fighter's speed
$\bar{V}_{01}$	bullet's composite velocity ( $\bar{V}_{01} = \bar{V}_0 + \bar{V}_1$ )
$\bar{V}_{01}^0$	unit vector of $V_{01}$
$\bar{V}_M$	target velocity
$\bar{V}_{cp}$	bullet's mean velocity
$\bar{\omega}_M$	target's relative angle velocity
$\bar{\omega}_1$	fighter's rotational angle velocity
$o-\bar{x}_1\bar{y}_1\bar{z}_1$	is the fighter's body coordinate system $\bar{x}_1^0\bar{y}_1^0\bar{z}_1^0$ which are separately the unit vectors on three axes
$\alpha, \beta$	fighter's attack angle and slip angle
$\theta$	fighter's pitching angle
$\Upsilon$	fighter's slope angle
$\psi_{\Sigma\mu} (-\mu)$	pitching total correction angle (or pitching total leading angle)
$\psi_{\Sigma\nu} (-\nu)$	azimuth total correction angle (or azimuth total leading angle); when $\mu$ and $\nu$ are in air-to-air gun snap-shot, this also indicates the fighter's pitching and azimuth angles of the tracer point on the tracer line.
$\omega_{Mx_1}, \omega_{My_1}, \omega_{Mz_1}$	indicate the projection of the target's relative angle velocity on the three axes of the fighter body's coordinate system
$\omega_{1x_1}, \omega_{1y_1}, \omega_{1z_1}$	indicate the projection of the fighter's rotational angle velocity on the three axes of the fighter body's coordinate system
$T_j$	computation time ( $T_j^* = \tilde{a}T_j$ )
$T_y$	the flight time required from after the bullet is shot until it hits the target
$\dot{\psi}_{\Sigma\mu}, \dot{\psi}_{\Sigma\nu}$	the rate of change for the pitching and azimuth total correction angles

$\alpha_{pitching}$ ,  $\alpha_{azimuth}$  the fighter's pitching and azimuth aiming angle components  
 $n$  fighter's normal overload  
 $\bar{a}_{lift}$  fighter's lift acceleration  
 $\bar{a}_{tangential}$ ,  $\bar{a}_{centripal}$  the fighter's tangential and centripal accelerations  
 $S$  Laplace operator  
 $\tau_1$  time constant  
 $\bar{g}$  gravitational acceleration  
 $ab, K_1, K_2, K_3, F, \tilde{a}$  the constants related to the ballistic and fighter flight parameters

All of the vectors have the following relationship with the fighter body's coordinate system:

$$\begin{aligned}
 \bar{D} &= D \begin{pmatrix} \cos \mu \cos \nu & \sin \mu & -\cos \mu \sin \nu \end{pmatrix} \begin{bmatrix} \bar{x}_1^* \\ \bar{y}_1^* \\ \bar{z}_1^* \end{bmatrix} \\
 \dot{\bar{D}} &= \dot{D} \begin{pmatrix} \cos \mu \cos \nu & \sin \mu & -\cos \mu \sin \nu \end{pmatrix} \begin{bmatrix} \bar{x}_1^* \\ \bar{y}_1^* \\ \bar{z}_1^* \end{bmatrix} \\
 \bar{V}_1 &= V_1 \begin{pmatrix} \cos \alpha \cos \beta & \sin \alpha & -\cos \alpha \sin \beta \end{pmatrix} \begin{bmatrix} \bar{x}_1^* \\ \bar{y}_1^* \\ \bar{z}_1^* \end{bmatrix} \\
 \bar{a}_* &= a_* \begin{pmatrix} 0 & 1 & 0 \end{pmatrix} \begin{bmatrix} \bar{x}_1^* \\ \bar{y}_1^* \\ \bar{z}_1^* \end{bmatrix} \\
 \bar{\eta} &= \eta \begin{pmatrix} -\sin \theta & -\cos \theta \cos \gamma & \cos \theta \sin \gamma \end{pmatrix} \begin{bmatrix} \bar{x}_1^* \\ \bar{y}_1^* \\ \bar{z}_1^* \end{bmatrix}
 \end{aligned}$$

Key: 1. Lift  
2. Lift

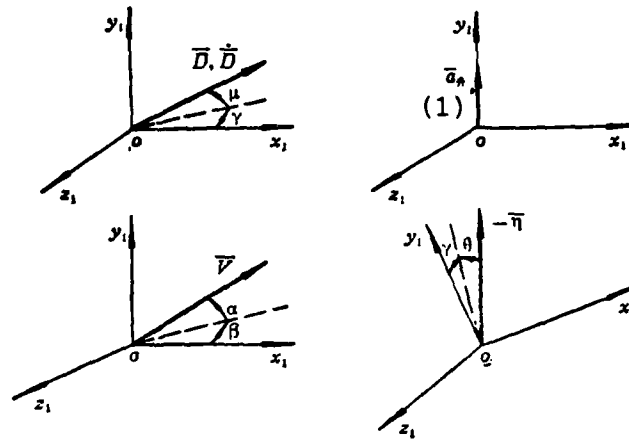


Fig. 1. The Relationship of All of the Vectors and the Fighter's Fuselage Coordinate System

In the fighter's fuselage coordinate system  $o-\bar{x}_1\bar{y}_1\bar{z}_1$ ,  $O$  is the point of origin in the fighter's gravitational center; the  $ox_1$  points straight toward the nose along the aircraft's longitudinal axis direction; the  $\bar{oy}_1$  points straight toward the cockpit along the aircraft's mechanical axis direction;  $\bar{oz}_1$  and  $\bar{ox}_1$ , and  $\bar{oy}_1$  form a right angle right hand coordinate system relationship.

Key: 1. Lift

The total design of the fighter weapon aiming system has a multifaceted content and the determining of the aiming computer equations is one of its important functions. Below we will discuss this problem under four types of different conditions.

1. The aiming computation of a non-maneuverable (or relatively lacking maneuverability) air target.

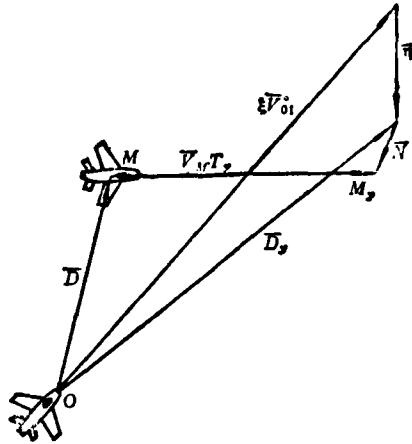


Fig. 2 Aiming Vector Diagram

Fig. 2 is the aiming vector diagram under this type of condition and from this we can arrange a deviation vector aiming equation:

$$\bar{N} = \bar{D} + \bar{V}_M T, - \xi \bar{V}_{01} - \bar{\eta}$$

Because

$$\bar{V}_M = \bar{V}_1 + \frac{d\bar{D}}{dt} = \bar{V}_1 + \dot{\bar{D}} + (\bar{\omega}_M \times \bar{D})$$

therefore

$$\begin{aligned} \bar{N} &= \bar{D} + \bar{V}_1 T, + \dot{\bar{D}} T, + (\bar{\omega}_M \times \bar{D}) T, - \xi \bar{V}_{01} - \bar{\eta} \\ &= \left( 1 + \frac{\dot{\bar{D}}}{\bar{D}} T, \right) \bar{D} + (\bar{\omega}_M \times \bar{D}) T, + \bar{V}_1 T, - \xi \left( \frac{\bar{V}_1 + \bar{V}_0}{V_{01}} \right) - \bar{\eta} \end{aligned}$$

AD-A110 282

FOREIGN TECHNOLOGY DIV WRIGHT-PATTERSON AFB OH  
ACTA AERONAUTICA ET ASTRONAUTICA SINICA.(U)  
DEC 81

F/G 1/3

UNCLASSIFIED

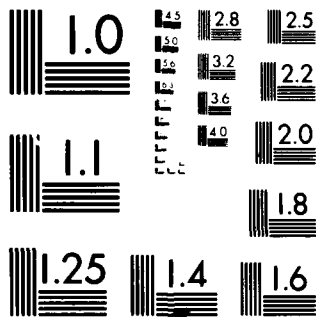
FTD-ID(RS)T-1129-81

NL

3 x 3  
AC A  
10/2/82



END  
DATE  
FILMED  
-82  
DTIC



MICROCOPY RESOLUTION TEST CHART

NATIONAL BUREAU OF STANDARDS-1963-A

Because

$$\xi \approx D, -V_o T,$$

therefore we obtain

$$\bar{N} = \left(1 + \frac{\dot{D}}{D} T\right) \bar{D} + (\bar{\omega}_M \times \bar{D}) T, + \left(1 - \frac{V_{op}}{V_{o1}}\right) \bar{V}_1 T, - \frac{V_{op}}{V_{o1}} T, \bar{V}_o - \bar{\eta}$$

Given that the gun axis and fuselage axis coincide, we use the relationship of all of the vectors and the fuselage coordinate system and project it toward the fighter's fuselage coordinate system. Therefore,  $\alpha, \beta, \mu, \nu, \eta$  and  $\sin \theta$  are all small and relatively small quantities and because of this we can consider  $\sin \alpha \approx \alpha, \sin \beta \approx \beta, \sin \mu \approx \mu, \sin \nu \approx \nu, \cos \alpha \approx \cos \beta \approx \cos \mu \approx \cos \nu \approx 1$ . If we overlook the quadratic or above quadratic small quantity then we can obtain the computing equations for ( $\bar{N}=0$ ) pitching channel total correction angle ( $\psi_{\Sigma \mu}$ ) and azimuth channel total correction angle ( $\psi_{\Sigma \nu}$ ) under aiming conditions:

$$\psi_{\Sigma \mu} = -\mu = \omega_{M1} T, + \frac{\eta \cos \theta \cos \gamma}{(V_{op} - V_{o1}) T},$$

$$\psi_{\Sigma \nu} = -\nu = \omega_{M2} T, - \frac{\eta \cos \theta \sin \gamma}{(V_{op} - V_{o1}) T},$$

In the equations,  $T_j = \frac{D}{v_{cp} - v_1}$  is the smoothing of the aiming line during track aiming and this causes the return of the people and aircraft to be steady. Damping coefficient  $x$  is introduced into the aiming computing equation; to obtain the target's relative angle velocity, we introduce the relationship of the angular velocity and the target's relative angle velocity when the fighter is track aiming:  $\omega_1 = \omega_M + \dot{\gamma}_2$ ; to decrease the dynamic error during track aiming we take  $T_j^* = \tilde{\alpha} T_j$  ( $\tilde{\alpha}$  is smaller than the coefficient of 1). In this way we obtain the following equations:

$$\psi_{z_0} = (\omega_{1z_1} - (1 + \kappa) \dot{\psi}_{z_0}) T_j^* \frac{\eta \cos \theta \cos \gamma}{(V_{sp} - V_1) T_j}$$

$$\psi_{z_0} = (\omega_{1z_1} - (1 + \kappa) \dot{\psi}_{z_0}) T_j^* \frac{\eta \cos \theta \sin \gamma}{(V_{sp} - V_1) T_j}$$

For the sake of simplification and convenience, if we can consider that during an attack the fighter makes equal overload circles, then the second item (aiming angle item) on the right end of the equation can obtain the following form:

Azimuth aiming angle  $\alpha_{az} = \frac{\eta \cos \theta \sin \gamma}{(V_{sp} - V_1) T_j} = \frac{\eta \cos \theta}{(V_{sp} - V_1) T_j} \frac{V_1 \omega_{1z_1} \cos \gamma}{g \cos \theta}$

Key: 1. Azimuth  $= \frac{D \eta V_1 \omega_{1z_1} V_{sp}}{(V_{sp} - V_1) D g D_y} = \frac{V_{sp} \eta V_1}{D_y g D_{\alpha}^2} \omega_{1z_1} T_j^*$

Pitch aiming angle  $\alpha_{pz} = \frac{\eta \cos \theta \cos \gamma}{(V_{sp} - V_1) T_j} = \frac{V_{sp} \eta T_j^*}{D_y D_{\alpha}^2} \cos \theta \cos \gamma$

Key: 1. Pitch

To correct the azimuth aiming angle then we use the method of multiplying  $T_j^*$  times a coefficient  $K_2$  smaller than 1 to approximate the correction and obtain:

$$\psi_{z_0} = (\omega_{1z_1} - (1 + \kappa) \dot{\psi}_{z_0}) T_j^* K_2$$

The total correction angle of the pitching channel also changes because of this:

$$\psi_{z_0} = (\omega_{1z_1} - (1 + \kappa) \dot{\psi}_{z_0}) T_j^* K_2 + \frac{V_{sp} \eta V_1}{D_y g D_{\alpha}^2} \omega_{1z_1} T_j^* + \frac{V_{sp} \eta T_j^*}{D_y D_{\alpha}^2} \cos \theta \cos \gamma$$

It is simplified into:  $\psi_{z_0} = (\omega_{1z_1} - (1 + \kappa) \dot{\psi}_{z_0}) T_j^* K_2 + \frac{V_{sp} \eta T_j^*}{D_y D_{\alpha}^2} \left( \cos \theta \cos \gamma + \frac{V_1 \omega_{1z_1}}{g} \right)$

Because

$$n = \cos \theta \cos \gamma + \frac{V_1 \omega_{1s1}}{g}, \text{ 并取 } \frac{(1) V_{a0} \eta T_0^2}{D_r D_a} \approx (aT_0^2 + b)$$

Key: 1. and take

we then obtain: 
$$\psi_{z0} = [\omega_{1s1} - (1 + \kappa) \dot{\psi}_{z0}] T_0^2 K_2 + (aT_0^2 + b) n$$

Naturally, in accordance with the difference of the selection and simplification methods for the aiming system plan, we can also obtain other forms of the aiming computing equation. For example:

$$\begin{aligned} \psi_{z0} &= [\omega_{1s1} - (1 + \kappa) \dot{\psi}_{z0}] T_0^2 + (aT_0^2 + b) \\ \psi_{z0} &= [\omega_{1s1} - (1 + \kappa) \dot{\psi}_{z0}] T_0^2 K_2 \end{aligned}$$

Whether it is the aiming computing accuracy or decreasing the system's complex equations both are satisfactory.

During the previous derivation and simplification process for the aiming computing equations, we overlooked the influence of the trailing angle item when shooting; further, because the attack is against a non-maneuverable (moving in a straight line at a constant speed) target, the roll rate (the angular rate projected on the fuselage coordinate system  $x_1$  axis) generally does not exceed  $3^\circ$ /second and the error caused by it is usually within 2-3 milliradian. Thus, we do not have to consider it.

## 2. The approximate aiming computing correction for a maneuvering target

This type of aiming computing correction is for improving the original sight (non-head-up display) weapon aiming system for use. Its aiming vector diagram is shown in figure 3.

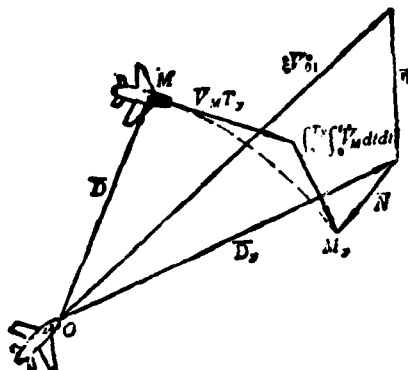


Fig. 3. Aiming Vector Diagram

The arrangement of its deviation vector aiming equation is:

$$\bar{N} = \bar{D} + \bar{V}_M T, + \int_0^T \int_0^t \dot{\bar{V}}_M dt dt - \xi \bar{V}_{01} - \bar{\eta}$$

When the bullet flight time is relatively short (close to the range of fire), we take  $\bar{V}_M$  as a constant (equal to  $\bar{V}_M$  when opening fire).

Further,

$$\bar{V}_M = \bar{V}_1 + \frac{d\bar{D}}{dt} = \bar{V}_1 + \dot{\bar{D}} + (\omega_M \times \bar{D})$$

$$\dot{\bar{V}}_M = \dot{\bar{V}}_1 + \ddot{\bar{D}} + 2\dot{\omega}_M \times \bar{D} + \dot{\omega}_M \times (\omega_M \times \bar{D}) + (\dot{\omega}_M \times \bar{D})$$

Overlooking the angle and second derivative item and second small quantity of the distance, we then obtain:

$$\bar{N} = \bar{D} + \bar{V}_1 T, + \dot{\bar{D}} T, + (\dot{\omega}_M \times \bar{D}) T, + \frac{1}{2} \dot{\bar{V}}_1 T^2 + (\dot{\omega}_M \times \bar{D}) T^2 - \xi \bar{V}_{01} - \bar{\eta}$$

When the fighter is in attack flight,  $\bar{V}_1 = \bar{a}_{\text{tangent}} + \bar{a}_{\text{vector}}$ , yet  $\bar{a}_{\text{tangent}}$  has a very small influence on the aiming computation. Therefore, we can take  $\bar{V}_1 \approx \bar{a}_{\text{vector}}$ ; take  $\eta \approx \frac{1}{2}gT_y^2$  (from this, the caused error is generally within 1%); when the fighter is in equal overload circles, there is the following relation in the acceleration:  $\bar{a}_{\text{lift}} = \bar{a}_{\text{tangent}} + (-g)$ . Thus we can obtain:

$$\bar{N} = \bar{D} + \bar{V}_1 T_y + \bar{D} T_y + (\bar{\omega}_M \times \bar{D}) T_y + \frac{1}{2} \bar{a}_n T_y^2 + (\bar{\omega}_M \times \bar{D}) T_y^2 - \xi \bar{V}_1^2 \quad (1)$$

Key: 1. Lift

Projected on the fighter's fuselage coordinate system, under aiming conditions, after  $\bar{N}=0$  simplification, we obtain:

$$\psi_{z_0} = (\omega_{1z_1} - (1 + \kappa) \dot{\psi}_{z_0}) T_y + \frac{1}{2} \frac{a_n^{(1)}}{(\bar{V}_{sp} - V_1)} T_y = (\omega_{1z_1} - (1 + \kappa) \dot{\psi}_{z_0}) T_y + K_3 a_n T_y$$

Key: 1. Lift

In the formula,  $a_n = ng$

$$K_3 = \frac{g^{(1)}}{2(\bar{V}_{sp} - V_1)}$$

$$\psi_{z_0} = (\omega_{1z_1} - (1 + \kappa) \dot{\psi}_{z_0}) T_y$$

Key 1: Lift

This aiming computing equation took into account the correction of the maneuvering target but did not take into account the influence of the roll rate. This is because most sight computers are electromechanical or electronically simulated wherein it is difficult to realize the correction of the roll rate influence. Yet, it must be pointed out that when there is a relatively large roll rate (over  $10^\circ/\text{second}$ ) the caused error cannot be overlooked. For example, when a fighter carries out aiming attack on a target with equal overload circles, the application of this formula group for aiming computing will be very accurate. Furthermore, this set of equations can also realize the computing of the reticle snap-shots which does not require a central spot of the reticle. It does, however, require

that before the reticle's central spot goes on the target we use the method of advancing the flight time firing of a shell and only then will the target be brought down.

3. Weapon aiming computing taking into account the corrections for the maneuvering of a target and the influence of the fighter's roll rate.

Its relationship within the aiming vector can be seen in fig. 3. The deviation vector aiming equation is:

$$\bar{N} = \bar{D} + \bar{V}_M T, + \int_0^T \int_0^t \dot{\bar{V}}_M dtdt - \xi \bar{V}_{01} - \bar{\eta}$$

With the same principle as was mentioned previously in the second part,  $\dot{\bar{V}}_M$  is viewed as a constant and when the relation of  $\bar{V}_M$  and  $\dot{\bar{V}}_M$  is substituted into the equation and we overlook the angle and second derivation item of the distance, then we obtain:

$$\begin{aligned} \bar{N} = & \bar{D} + \bar{V}_1 T, + \dot{\bar{D}} T, + (\bar{\omega}_M \times \bar{D}) T, + \frac{1}{2} \dot{\bar{V}}_1 T^2 + (\bar{\omega}_M \times \dot{\bar{D}}) T^2 + \frac{1}{2} \bar{\omega}_M \\ & \times (\bar{\omega}_M \times \bar{D}) T^2 - \xi \bar{V}_{01} - \bar{\eta} \end{aligned}$$

With the same rationale we took

$$\begin{aligned} \dot{\bar{V}}_1 \approx \bar{a}_M, \quad \bar{\eta} = \frac{1}{2} \bar{g} T^2, \quad \bar{a}_M = \bar{a}_M + (-\bar{g}) \\ (1) \quad \quad \quad (2) \quad (3) \end{aligned}$$

Key: 1. Tangent  
2. Lift  
3. Tangent

and then we obtained

$$\begin{aligned} \bar{N} = & \bar{D} + \bar{V}_1 T, + \dot{\bar{D}} T, + (\bar{\omega}_M \times \bar{D}) T, + \frac{1}{2} \bar{a}_* T^2 + (\bar{\omega}_M \times \dot{\bar{D}}) T^2 \\ & + \frac{1}{2} \bar{\omega}_M (\bar{\omega}_M \times \bar{D}) T^2 - \xi \bar{V}_{01} \end{aligned}$$

Key: 1. Lift

In the formula

$$\bar{\omega}_M \times (\bar{\omega}_M \times \bar{D}) = \bar{\omega}_M (\bar{\omega}_M \cdot \bar{D}) - \bar{D} (\bar{\omega}_M \cdot \bar{\omega}_M) \approx \bar{\omega}_M D \omega_{1s1} - \bar{D} \omega_M^2$$

When this formula is substituted into the  $\bar{N}$  relation, we obtain:

$$\begin{aligned} \bar{N} = & \bar{D} + \bar{V}_1 T, + \dot{\bar{D}} T, + (\bar{\omega}_M \times \bar{D}) T, + \frac{1}{2} \bar{a}_* T^2 + (\bar{\omega}_M \times \dot{\bar{D}}) T^2 \\ & + \frac{1}{2} \bar{\omega}_M D \omega_{1s1} T^2 - \frac{1}{2} \bar{D} \omega_M^2 T^2 - \xi \bar{V}_{01} \end{aligned}$$

Key: 1. Lift

When each vector is projected toward the fuselage coordinate system and simplified, we can obtain the aiming computing equations under aiming conditions:

$$\begin{aligned} \psi_{2\mu} = -\mu = & [\omega_{1s1} - (1+x)\dot{\psi}_{2\mu}] T, + \frac{1}{2} \frac{a_* (1)}{(V_{0s} - V_1)} T^2, + \frac{1}{2} \omega_{1s1} \nu T, \\ \psi_{2\nu} = -\nu = & [\omega_{1s1} - (1+x)\dot{\psi}_{2\nu}] T, - \frac{1}{2} \omega_{1s1} \mu T, \end{aligned}$$

Key: 1. Lift

In the equations,  $a_{\text{lift}} = ng$ .

This takes into account the correction for the maneuvering of the target as well as the fuselage's roll rate influence on the corrected aiming computing equation. It is generally applied for use in the numerical computer's weapon aiming system.

4. Its application in the head-up display aiming system can carry out snap-shot tracer line aiming computing for air-supported maneuvering targets.

The typical display of this type of aiming attack method developed during the 1970's is shown in fig. 4.

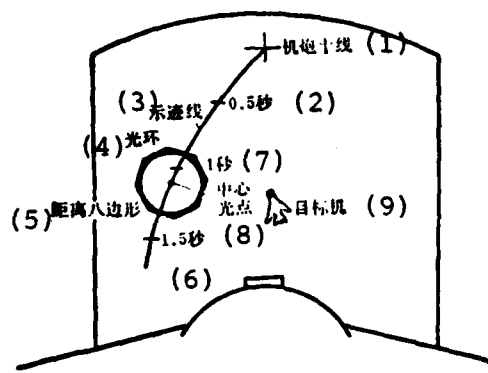


Fig. 4. Typical Display Diagram of Tracer Line

- Key:
1. Gun cross line
  2. 0.5 seconds
  3. Tracer line
  4. Reticle
  5. Distance octagon
  6. 1.5 seconds
  7. 1 second
  8. Central spot
  9. Target aircraft

In principle, the snap-shot tracer line can be divided into two types: one type is the past historical tracer line (also called the hot line) and the other type is the damped calculated tracer line. The so-called historical tracer line indicates the connecting line of the real time calculation and each different

time a hypothetical bullet is fired within a past period of time opposite a fighter's bullet tracing point. Its principle-vector relation diagram is shown in fig. 5.

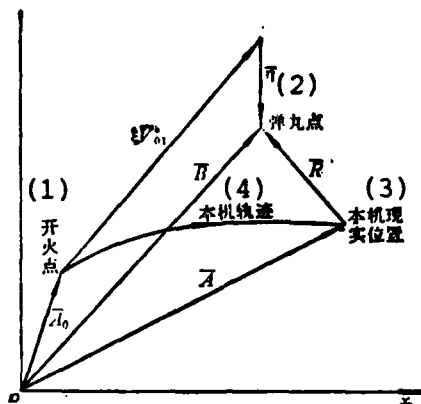


Fig. 5. Principle-Vector Relation Diagram

- Key: 1. Firing point  
 2. Bullet point  
 3. Fighter's realized position  
 4. Fighter's locus

In the figure,  $o$  is the reference point,  $xoy$  is the selected coordinate system;  $\bar{A}(t)$  is the target's maneuvering acceleration.

The realized bullet point position is

$$\bar{B} = \bar{A}_0 + \xi \bar{V}_{01} + \bar{n}$$

The realized fighter position is

$$\bar{A} = \bar{A}_0 + \int_0^{T_y} \int_0^t \bar{A}(t) dt di + \bar{V}_i T_y$$

Because  $\bar{R} = \bar{B} - \bar{A}$ ,  $\bar{R}$  is the vector of the realized bullet position opposite the fighter's realized position. Therefore, we obtain

$$\bar{R} = \xi \bar{V}_0 + \bar{\eta} - \int_0^{T_y} \int_0^t \bar{A}(t) dt di + \bar{V}_i T_y$$

$\bar{A}(t)$  is the fighter's motion acceleration.

When there are projection calculations of all of the vectors in this vector equation within the realized fuselage coordinate system we can then obtain the aiming computing equation of the past historical tracer line. Using the equation, we can calculate the bullet's tracer point each time a hypothetical bullet is fired opposite the fighter's realized position. The connecting line of these points is displayed on the head-up display which is the past historical tracer line.

The damped calculated tracer line is sometimes also called the damped tracer line. Because of the differences of the computing method and damped lead-in method, it has many different types. The most commonly used among them is the type of tracer line obtained after repeated calculations using the total correction angle aiming computing equations derived in part three above. The damping in the equation can set up a composition that is changeable. The total correction angle aiming computing equation mentioned previously can also be rewritten in the following form:

$$\mu = \frac{-1}{1 + \tau_1 S} \left[ \omega_{1z} + \frac{1}{2} \frac{ng}{(V_{sp} - V_1)} + \frac{1}{2} \omega_{1z} v \right] T,$$

$$v = \frac{-1}{1 + \tau_1 S} \left[ \omega_{1y} - \frac{1}{2} \omega_{1z} \mu \right] T,$$

In the equations,  $\mu$  and  $v$  separately indicate each different Ty time tracer point on the tracer line opposite the fighter's pitching angle and azimuth angle;

$\tau_1$  is the damping time constant which can change within  $0.5 T, -1.20 T,$ ;

S is the Laplace operator.

The above can be used for the tracer line of air-to-air gun snap-shot and has often been applied to antiaircraft guns (such as the American six barrel gun). Furthermore, if this type of attack method is used for most single barrel aerial guns with relatively low firing speeds, the shooting down probability of air-supported targets cannot be very high. Naturally, if several more simultaneous volleys are installed on the aircraft, in principle, this is also a type of remedy method yet this is further limited by other conditions.

This paper only analyzed and discussed several specific problems regarding the fighter weapon aiming system. It did not, however, mention the director type weapon aiming system or the MRGS system which is now being developed abroad.

#### References

1. AD786464, MAJOR ANTHONY L. LEATHAM, MAJOR JOHN C. DURRETT, A DIGITAL LEAD COMPUTING OPTICAL SIGHT MODEL, SEPTEMBER, 1974, p. 50.
2. AD775360, Berg, R.L., Sears, M.M., AIR-TO-AIR FIRE CONTROL EXPOSITION PHASE III (EXPO III), September, 1973, p. 105.

3. U.S. Air Force Academy Technical Report 69-3, Gilbert, S.W., Preyss, A.E. and Willis, R.E., Snap-Shot Gunsight for Fixed-Gun Fighter Aircraft, December, 1969.
4. AGARD-LS-76, J.T. SHEPHERD, THE APPLICATION OF DISPLAYS IN NAVIGATION/ATTACK SYSTEMS.

#### **Abstract**

This paper presents several derivations of the aiming computing equations for the "Non-Director" or the "Disturbed Reticule" system in the aiming computer systems of the air-to-air gunsight and head-up display weapon. The paper deals with four cases; the fighter attacks the non-maneuverable target which is considered as moving in a straight line at a constant speed; the fighter attacks a maneuvering target and the corrections for the maneuvering of the target are taken into account in the aiming computation; the fighter attacks a maneuvering target and the corrections for the maneuvering of the target and the effect of fighter's own roll rate are taken into account in the aiming computation; during the attack of the fighter on a maneuvering target the historical tracer line (hot line) and a version of the damped tracer line based on multiple Leos computations are adapted in the computation for air-to-air gun snap-shot.

THE OPTIMUM DESIGN OF NON-MOMENT LAMINATED COMPOSITE PLATE  
- According to static failure strength condition -

Ma Zukang  
(Northwestern Polytechnical University)

Abstract

When the upper and/or lower panels of the loading box of the aircraft wing surface is made of the fiber reinforced composite laminates, they can frequently be simplified as a non-moment plate. This paper introduces an optimum design method of the laminated plate according to static failure strength condition. The mathematical tool used in the measure is the Lagrangian multiplier method and the static failure strength condition is adopted as Hill-Tsai criteria and Norris criteria.

The formulas for optimum design have not only been derived, but also reformed to be convenient for application in the computer. How to establish the ultimate strength of laminates is also discussed in detail. An example, illustrating the solution procedure and how to select the optimum scheme of lamination design, is presented in this paper. Some technical problems are briefly discussed in the last part.

At the stage of the preliminary structural design, this procedure can be considered as an engineering method of lamination optimum design for the loading panel of laminated composite which works under tension or compression (assuming that the buckling failure would not occur).

## I. Preface

The total bearing action of the upper and/or lower panels of the loading box of the aircraft wing surface is mainly the axial load and shear load in the bearing plate plane. Even the aerodynamic load of the vertical plate plane is a local bearing problem which cannot be overlooked in the preliminary structural design when calculating the total strength. Aside from this, to avoid the coupling effects of the laminated composite plate, the lamination should be designed into a symmetrical mirror surface. Furthermore, because the curve of the wing's stressed panel is very small and is close to a flat plate, the wing's stressed panel can be taken as a non-moment laminated plate. That is, moments without internal or external force. Further, the laminated plate is in a plane stress condition. Frequently, a  $0^\circ/+45^\circ/90^\circ$  lamination is used by this type of loading laminated plate (the principle of this method is still appropriate for other lamination angles).

Because the lamination of the laminated plate mainly affects the layer's normal stress and shear stress but has a very small effect on the bearing capability, the main content of this paper concerning the optimum design of non-moment laminated plate is the determination of the number of layers needed by each directional layer based on the size of the external load so that the laminated plate will have the lightest weight under certain constraint conditions. These constraint conditions are under the action of the design load and in accordance with the static failure strength criteria, the laminated plate's safety tolerance is zero (or the remaining strength coefficient is 1). Mathematically, this is the problem of finding the conditional extreme value which can be solved by using the Lagrangian multiplier method.

## II. Constraint Conditions

We can select suitable failure criteria based on the type

reinforced fiber. For example, we can use the Norris criteria (generalized divalent interaction law)

$$\left(\frac{N_x}{D_x}\right)^2 + \left(\frac{N_y}{D_y}\right)^2 - \frac{N_x N_y}{D_x D_y} + \left(\frac{N_s}{D_s}\right)^2 = 1$$

or the Hill-Tsai criteria

$$\left(\frac{N_x}{D_x}\right)^2 + \left(\frac{N_y}{D_y}\right)^2 - \frac{N_x N_y}{D_x^2} + \left(\frac{N_s}{D_s}\right)^2 = 1$$

In the formulas, the  $N_x, N_y$  and  $N_s$  are the design loads (service loads) of the unit lengths on the x, y and s axes defined in figure 1. The unit is pounds/inch or kilograms/centimeter.

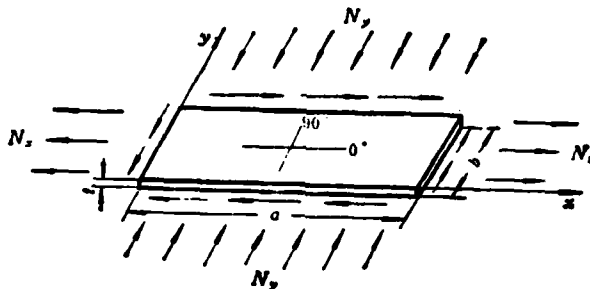


Fig. 1. The Plane Stress Action on the Laminated Plate

In  $N_k = f_k t = f_k (t_x + t_y = t_s)$ , ( $k$  is the service stress of the  $k$  direction and  $k=x, y, s$ ).

$D_x, D_y$  and  $D_s$  are the ultimate loads (permissible loads) of the unit lengths on the y and s directions. The unit is also

pounds/inch or kilograms/centimeter.

In  $D_k = F_k t = F_k (t_x + t_y + t_s)$ ,  $F_k$  is the ultimate stress (ultimate strength) of the  $k$  direction and  $k=x, y, s$ .

### III. Determining the Ultimate Strength of the Laminated Plate

When we take into account that the ultimate strength of the laminated plate along a certain axis direction is obtained from the ultimate strength of each directional layer provided in the corresponding direction according to the linear weighted average rule, it is

$$F_x = (F_{xx}t_x + F_{xy}t_y + F_{xs}t_s) \frac{1}{t} = \left( \frac{F_{xx}}{F_a} \frac{t_x}{t} + \frac{F_{xy}}{F_a} \frac{t_y}{t} + \frac{F_{xs}}{F_a} \frac{t_s}{t} \right) F_a$$

$$= (a_{xx}L + a_{xy}M + a_{xs}N) F_a$$

In the formula,

$F_x$  is the ultimate strength of the laminated plate along the  $x$  axis (the unit is kilograms/centimeter<sup>2</sup> or 1000 pounds/inch<sup>2</sup>);

$F_{xx}, F_{xy}, F_{xs}$  are the ultimate strengths able to be provided along the  $x$  axis by each directional layer under plane stress conditions;

$F_a$  is the longitudinal tensile ultimate stress of the single direction composite material;

$t_x, t_y, t_s$  are the thicknesses of each directional layer;

$t$  is the total thickness of the laminated plate;

$L, M, N$  are the thickness ratios of each directional layer;

$a_{kj}$  is the stress coefficient ( $kj=x, y, s$ ).

Based on the definitions of figure 1, we know that  $F_{xx} = F_a$  and therefore  $a_{xx} = 1$ .

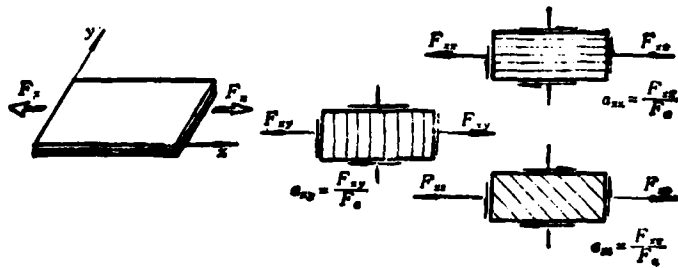


Fig. 2. Schematic Drawing of Ultimate Strength for the Laminated Plate in Each Direction.

In the same way, we can obtain:

$$F_y = (a_{yz}L + a_{yy}M + a_{y1}N)F_a$$

$$F_x = (a_{xz}L + a_{xx}M + a_{x1}N)F_a$$

Based on the definitions of figures 3(a) and (b) we know that  $a_{yy} = 1$ ,  $a_{yx} = a_{xy}$ ,  $a_{xs} = a_{ys}$ ,  $a_{sx} = a_{sy}$ , and  $a_{ss}$  and  $a'_{ss}$  are not necessarily equal yet to simplify we consider that  $a_{ss} = a'_{ss}$ .

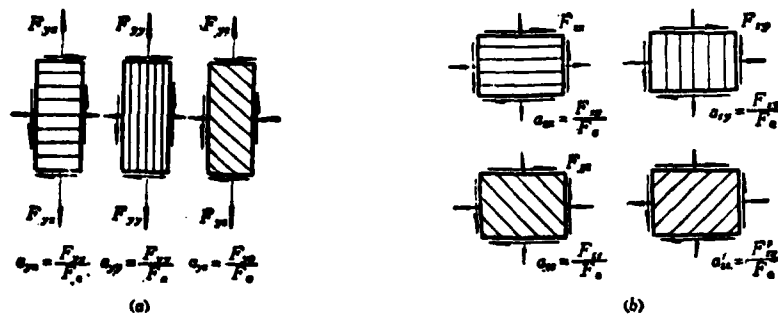


Fig. 3. Schematic Drawing of Ultimate Strength for the Laminated Plate in Each Direction.

Written in a matrix form, it is:

$$\begin{bmatrix} F_x \\ F_y \\ F_z \end{bmatrix} = \begin{bmatrix} a_{xx} & a_{xy} & a_{xz} \\ a_{yx} & a_{yy} & a_{yz} \\ a_{zx} & a_{zy} & a_{zz} \end{bmatrix} \begin{bmatrix} LF_o \\ MF_o \\ NF_o \end{bmatrix}$$

If we use the ultimate load of the unit width then it is:

$$\begin{bmatrix} D_x \\ D_y \\ D_z \end{bmatrix} = \begin{bmatrix} a_{xx} & a_{xy} & a_{xz} \\ a_{yx} & a_{yy} & a_{yz} \\ a_{zx} & a_{zy} & a_{zz} \end{bmatrix} \begin{bmatrix} t_x F_o \\ t_y F_o \\ t_z F_o \end{bmatrix}$$

#### IV. The Method of Lamination Optimum Design Method

##### 1. Method and Steps

Because it is necessary that the determined variables are  $t_x$ ,  $t_y$ ,  $t_s$ , the weight function of the non-moment plate is  $f(t_x, t_y, t_s) = (t_x + t_y + t_s)AY$ . In the formula, A is the plate surface area and Y is material's specific gravity

The constraint condition is a certain strength criterion.

For example, using the Norris criteria,

$$\varphi(t_x, t_y, t_s) = \left(\frac{N_x}{D_x}\right)^2 + \left(\frac{N_y}{D_y}\right)^2 - \frac{N_x N_y}{D_x D_y} + \left(\frac{N_z}{D_z}\right)^2 - 1 = 0.$$

In the formula,  $D_x$ ,  $D_y$  and  $D_s$  are all functions of  $t_x$ ,  $t_y$  and  $t_s$ , and then  $N_x$ ,  $N_y$  and  $N_s$  are related to  $t_x$ ,  $t_y$  and  $t_s$ .

Applying the Lagrangian multiplier method:

$$\begin{aligned}
 W &= f(t_x, t_y, t_z) + \lambda \varphi(t_x, t_y, t_z) \\
 &= (t_x + t_y + t_z)AY + \lambda \left[ \left( \frac{N_x}{D_x} \right)^2 + \left( \frac{N_y}{D_y} \right)^2 - \frac{N_x N_y}{D_x D_y} + \left( \frac{N_x}{D_x} \right)^2 - 1 \right]
 \end{aligned}$$

Separately letting  $\frac{\partial W}{\partial t_x} = 0$ ,  $\frac{\partial W}{\partial t_y} = 0$  and  $\frac{\partial W}{\partial t_z} = 0$ , we can attain the following three formulas:

$$\frac{AYD_x^2}{2\lambda F_x} = a_{xx}N_x^2 + a_{yy}N_y^2 \left( \frac{D_x}{D_y} \right)^2 - 0.5N_x N_y \left[ a_{xx} \left( \frac{D_x}{D_y} \right) + a_{yy} \left( \frac{D_x}{D_y} \right)^2 \right] + a_{xx}N_x^2 \left( \frac{D_x}{D_x} \right)^2 \quad (1)$$

$$\frac{AYD_y^2}{2\lambda F_y} = a_{xx}N_x^2 + a_{yy}N_y^2 \left( \frac{D_x}{D_y} \right)^2 - 0.5N_x N_y \left[ a_{xx} \left( \frac{D_x}{D_y} \right) + a_{yy} \left( \frac{D_x}{D_y} \right)^2 \right] + a_{yy}N_y^2 \left( \frac{D_x}{D_y} \right)^2 \quad (2)$$

$$\frac{AYD_z^2}{2\lambda F_z} = a_{xx}N_x^2 + a_{yy}N_y^2 \left( \frac{D_x}{D_y} \right)^2 - 0.5N_x N_y \left[ a_{xx} \left( \frac{D_x}{D_y} \right) + a_{yy} \left( \frac{D_x}{D_y} \right)^2 \right] + a_{xx}N_x^2 \left( \frac{D_x}{D_x} \right)^2 \quad (3)$$

When formula (1) is reduced into formula (2) and the  $a_{sx} = a_{sy}$  relation is applied, we obtain:

$$(a_{xx} - a_{yy})N_x^2 + (a_{yy} - a_{xx})N_y^2 \left( \frac{D_x}{D_y} \right)^2 - 0.5N_x N_y \left[ (a_{xx} - a_{yy}) \left( \frac{D_x}{D_y} \right) + (a_{yy} - a_{xx}) \left( \frac{D_x}{D_y} \right)^2 \right] = 0 \quad (4)$$

When formula (1) is reduced into formula (3), we obtain:

$$\begin{aligned} (a_{zz} - a_{zz'})N_z^2 + (a_{yy} - a_{yy'})N_y^2 \left(\frac{D_z}{D_y}\right)^2 - 0.5N_z N_y \left[ (a_{zz} - a_{zz'})\left(\frac{D_z}{D_y}\right) + (a_{yy} - a_{yy'})\left(\frac{D_z}{D_y}\right)^2 \right] \\ + (a_{zz} - a_{zz'})N_z^2 \left(\frac{D_z}{D_y}\right)^2 = 0 \end{aligned} \quad (5)$$

The selected strength criteria can be rewritten as:

$$D_z^2 = N_z^2 + N_y^2 \left(\frac{D_z}{D_y}\right)^2 - N_z N_y \left(\frac{D_z}{D_y}\right) + N_z^2 \left(\frac{D_z}{D_y}\right)^2 \quad (6)$$

The  $\left(\frac{D_x}{D_y}\right)$  found in formula (4) is substituted into formula (5) and then the found  $\left(\frac{D_x}{D_s}\right)$  is substituted into formula (6) and we proceed to find  $D_x$ . The positive and negative signs of  $D_x$  are identical to those of  $N_x$ .

We have already obtained from the last section that:

$$\begin{bmatrix} D_x \\ D_y \\ D_z \end{bmatrix} = \begin{bmatrix} a_{xx} & a_{xy} & a_{xz} \\ a_{yx} & a_{yy} & a_{yz} \\ a_{zx} & a_{zy} & a_{zz} \end{bmatrix} \begin{bmatrix} t_x F_x \\ t_y F_y \\ t_z F_z \end{bmatrix} = F_a [A] \begin{bmatrix} t_x \\ t_y \\ t_z \end{bmatrix}$$

$$\begin{bmatrix} t_x \\ t_y \\ t_z \end{bmatrix} = \frac{D_x}{F_x} [A]^{-1} \begin{bmatrix} 1 \\ (D_x/D_y) \\ (D_x/D_z) \end{bmatrix} \quad (7)$$

When the found  $D_x$ ,  $\frac{D_x}{D_y}$  and  $\frac{D_x}{D_z}$  are substituted into formula (7), if  $[A]^{-1}$  and  $F_a$  are already known, then we can find the values of  $t_x$ ,  $t_y$  and  $t_z$ . When  $t_k$  is divided by the thickness of a single layer plate then we obtain the layer number  $n_k$  of each directional layer. However, in most situations the  $n_k$  is not necessarily a positive integer so that at this time we can take the closest positive integer as the feasible scheme value. In this way, we have several sets of feasible schemes and its safety tolerance for each set of calculations is

$$\text{M. S.} = \frac{1}{\left(\frac{N_x}{D_x}\right)^2 + \left(\frac{N_y}{D_y}\right)^2 - \frac{N_x N_y}{D_x D_y} + \left(\frac{N_z}{D_z}\right)^2} - 1$$

The selection of M.S. is the largest positive value as the optimum design scheme.

## 2. Calculation Examples

A cylindrical structure having a radius of  $R=10$  inches, a maximum pressure inside the cylinder of  $P=1000$  pounds/inch<sup>2</sup> also sustains a maximum torque of 2 million inch pounds. The material used is boron/epoxy composite material,

its single direction permissible strength is  $F_a=173,000$  pounds/inch<sup>2</sup>, and the single layer thickness of each type of lamination ( $0^\circ, 90^\circ, \pm 45^\circ$ ) is  $t_0=0.0075$  inches. After arranging the test data, the stress coefficient matrix which is

$$[A] = \begin{bmatrix} a_{xx} & a_{xy} & a_{xz} \\ a_{yx} & a_{yy} & a_{yz} \\ a_{zx} & a_{zy} & a_{zz} \end{bmatrix} = \begin{bmatrix} 1 & -0.1266 & 0.2133 \\ -0.1266 \left(\frac{N_y}{N_x}\right)^2 & 1 & 0.2133 \\ 0.2133 & 0.2133 & 0.4266 \end{bmatrix}$$

finds the lamination optimum design scheme of this structured cylinder.

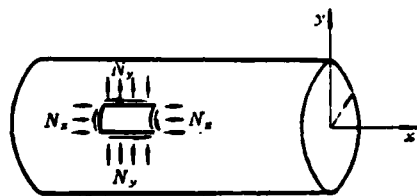


Fig. 4. Example Figure

The solution of the external load is

$$N_x = PR = 1 \times 10 = 10,000 \text{ pounds/inch}$$

$$N_y = P \frac{R}{2} = 5,000 \text{ pounds/inch}$$

$$N_s = \frac{T}{2\pi R^2} = 3.183 \text{ pounds/inch}$$

therefore  $\frac{N_y}{N_x} = 0.5, \frac{N_s}{N_x} = 0.3183$

$$[A] = \begin{bmatrix} 1 & -0.1266 & 0.2133 \\ -0.0316 & 1 & 0.2133 \\ 0.2133 & 0.2133 & 0.4266 \end{bmatrix}, \quad [A]^{-1} = \begin{bmatrix} 1.202 & 0.304 & -0.735 \\ 0.181 & 1.166 & -0.674 \\ -0.674 & -0.735 & 3.049 \end{bmatrix}$$

When already known data is substituted into formulas (4), (5) and (6), we can obtain  $\frac{D_x}{D_y} = 1.772$ ,  $\frac{D_x}{D_s} = 2.362$  and  $D_x = 12,100$  pounds/inch. Further, when the obtained results are substituted into formula (7), we can obtain

$$\begin{bmatrix} t_x \\ t_y \\ t_z \end{bmatrix} = \frac{12,100}{173} \begin{bmatrix} 1.202 & 0.304 & -0.735 \\ 0.181 & 1.166 & -0.674 \\ -0.674 & -0.735 & 3.049 \end{bmatrix} \begin{bmatrix} 1 \\ 1 \\ 2.362 \end{bmatrix} = \begin{bmatrix} 0.0743 \\ 0.0387 \\ 0.0141 \end{bmatrix} \text{英寸} \quad (1)$$

$$\begin{bmatrix} n_x \\ n_y \\ n_z \end{bmatrix} = \frac{1}{t_0} \begin{bmatrix} t_x \\ t_y \\ t_z \end{bmatrix} = \frac{1}{0.0075} \begin{bmatrix} 0.0743 \\ 0.0387 \\ 0.0141 \end{bmatrix} = \begin{bmatrix} 9.9 \\ 5.2 \\ 1.8 \end{bmatrix} \text{层} \quad (2)$$

Key: 1. Inch  
2. Layer

Because  $\Sigma n = 16.9$  layer, therefore we take the  $\Sigma n = 17$  layer. In this way we have the following three types of feasible schemes and separately calculate their safety tolerances.

$$D_x = F_s(a_{xx}t_x + a_{xy}t_y + a_{xz}t_z) = 1.298n_x - 0.164n_y + 0.277n_z$$

$$D_y = F_s(a_{yx}t_x + a_{yy}t_y + a_{yz}t_z) = -0.041n_x + 1.298n_y + 0.277n_z$$

$$D_s = F_s(a_{sx}t_x + a_{sy}t_y + a_{sz}t_z) = 0.277(n_x + n_y + 2n_z)$$

(1) 设计方案	$n_x$	$n_y$	$n_z$	$D_x$	$D_y$	$D_s$	M.S.
1	9	6	2	11.252	7.973	5.263	+0.008
2	10	5	2	12.714	6.634	5.263	+0.0416
3	10	6	1	12.273	7.655	4.986	+0.0352

Key: 1. Design scheme

Based on the M.S. values, we should select scheme 2 as the lamination optimum design scheme.

### 3. Improvement of Method

During actual operation, the calculation of the structural design is a step-by-step approximation process. In addition, the external loads and stressed panels often require partitioned calculations and thus in order to decrease the amount of work and make it convenient for using an electronic computer, we can use the above mentioned calculation measures to make the following changes. According to the matrix formula we know

$$[A]^{-1} = \frac{1}{|A|} \begin{bmatrix} A_{22} & A_{yz} & A_{12} \\ A_{zy} & A_{yy} & A_{1y} \\ A_{z1} & A_{y1} & A_{11} \end{bmatrix}$$

In the formula,  $A_{22} = a_{yy}a_{11} - a_{yz}a_{1y}$ ,  $A_{zy} = a_{yz}a_{12} - a_{yy}a_{11}$  etc. Formula (7) can be rewritten as:

$$\begin{bmatrix} t_x \\ t_y \\ t_z \end{bmatrix} = \frac{D_x}{F_s |A|} \begin{bmatrix} A_{22} & A_{yz} & A_{12} \\ A_{zy} & A_{yy} & A_{1y} \\ A_{z1} & A_{y1} & A_{11} \end{bmatrix} \begin{bmatrix} \frac{1}{D_x} \\ \frac{D_y}{D_x} \\ \frac{D_z}{D_x} \end{bmatrix}$$

Therefore, we obtain

$$\frac{t_x}{t_z} = \frac{A_{yz} + A_{yy} \frac{D_y}{D_x} + A_{1y} \frac{D_z}{D_x}}{A_{22} + A_{yz} \frac{D_y}{D_x} + A_{12} \frac{D_z}{D_x}} = r_1 \quad (8)$$

$$\frac{t_y}{t_z} = \frac{A_{z1} + A_{y1} \frac{D_y}{D_x} + A_{11} \frac{D_z}{D_x}}{A_{22} + A_{yz} \frac{D_y}{D_x} + A_{12} \frac{D_z}{D_x}} = r_2 \quad (9)$$

Furthermore, formulas (4), (5) and (6) can separately be re-written as:

$$(a_{xx} - a_{yy}) + (a_{yz} - a_{yy}) \left( \frac{N_z}{N_x} \right)^2 \left( \frac{D_x}{D_y} \right)^2 - 0.5 \left( \frac{N_z}{N_x} \right) \left[ (a_{xz} - a_{xy}) \left( \frac{D_x}{D_y} \right) + (a_{yz} - a_{yy}) \left( \frac{D_x}{D_y} \right)^2 \right] = 0 \quad (10)$$

$$(a_{xx} - a_{xz}) + (a_{yz} - a_{yy}) \left( \frac{N_z}{N_x} \right)^2 \left( \frac{D_x}{D_y} \right)^2 - 0.5 \left( \frac{N_z}{N_x} \right) \left[ (a_{xz} - a_{xy}) \left( \frac{D_x}{D_y} \right) + (a_{yz} - a_{yy}) \left( \frac{D_x}{D_y} \right)^2 \right] + (a_{xz} - a_{xy}) \left( \frac{N_z}{N_x} \right)^2 \left( \frac{D_x}{D_y} \right)^2 = 0 \quad (11)$$

$$\frac{D_x^2}{N_x^2} = 1 + \left( \frac{N_z}{N_x} \right)^2 \left( \frac{D_x}{D_y} \right)^2 - \left( \frac{N_z}{N_x} \right) \left( \frac{D_x}{D_y} \right) + \left( \frac{N_z}{N_x} \right)^2 \left( \frac{D_x}{D_y} \right)^2 \quad (12)$$

When the  $\left( \frac{D_x}{D_y} \right)$  from formula (10) is substituted into formula (11) and the  $\left( \frac{D_x}{D_s} \right)$  of formula (11) is then substituted into formulas (8) and (9), we can find  $r_1$  and  $r_2$ . At the same time, when  $\left( \frac{D_x}{D_y} \right)$  and  $\left( \frac{D_x}{D_s} \right)$  are substituted into formula (12), we can find  $\frac{D_x}{N_x}$ .

Letting  $\frac{D_x}{N_x} = R$ , then  $D_x = RN_x$

Further  $D_x = F_s(a_{xx}t_x + a_{xy}t_y + a_{xz}t_z) = F_s t_x (a_{xx} + a_{xy}r_1 + a_{xz}r_2)$

Therefore, we obtain  $RN_x = F_s t_x (a_{xx} + a_{xy}r_1 + a_{xz}r_2)$

We know from this that

$$\frac{F_s t_x}{N_x} = \frac{F_s}{N_x} (t_x + t_y + t_z) = \frac{R(1 + r_1 + r_2)}{a_{xx} + a_{xy}r_1 + a_{xz}r_2} \quad (13)$$

$$L = \frac{t_y}{t_x} = \frac{1}{1 + r_1 + r_2} \quad (14)$$

$$N = \frac{t_z}{t_x} = \frac{r_2}{1 + r_1 + r_2} \quad (15)$$

Only if we give the values of  $\frac{N_y}{N_x}$  and  $\frac{N_s}{N_x}$ , based on the known (A) and the  $F_a$  in accordance with formulas (8)-(15), we can find the corresponding numerical values of L and N, and  $\frac{F_a t}{N_x}$ . If we take a series of  $\frac{N_y}{N_x}$  and  $\frac{N_s}{N_x}$  based on a certain specific value then we can use hand computation or an electronic computer to calculate the following table for the approximate step-by-step calculation during the preliminary design.

$\frac{N_y}{N_x}$	$\frac{N_s}{N_x}$	$\frac{F_a t}{N_x}$	L	N
1.00	0			
↕	0.25			
	0.50			
	0.75			
1.00	1.00			
0.75	0			
↕	0.25			
	⋮			

#### 4. Special Circumstances

(1) If there is only the action of  $N_k$

The optimum design of lamination is naturally accomplished by the lamination along the k direction,

$$t_k = \frac{N_k}{a_{kk} F_a} \quad (k = x, y, s)$$

(2) If there is only the action of  $N_x$  and  $N_s$  then  $N_y \approx 0$ . This type of loaded situation has practical significance for the stress panel of the wing surface and therefore we will discuss this in greater detail.

From formula (11) we can obtain:

$$\frac{D_x}{D_t} = \sqrt[3]{\frac{a_{xx} - a_{xt}}{a_{tx} - a_{tt}} \frac{1}{\left(\frac{N_t}{N_x}\right)^3}} \quad (16)$$

Because

$$\begin{bmatrix} D_x \\ D_t \end{bmatrix} = \begin{bmatrix} a_{xx} & a_{xt} \\ a_{tx} & a_{tt} \end{bmatrix} \begin{bmatrix} F_x t_x \\ F_t t_t \end{bmatrix}$$

we therefore obtain

$$r = \frac{t_t}{t_x} = \frac{a_{xx} - a_{xt} \left(\frac{D_x}{D_t}\right)}{a_{tx} \left(\frac{D_x}{D_t}\right) - a_{tt}} \quad (17)$$

From formula (12) we can obtain

$$R = \sqrt{1 + \left(\frac{N_t}{N_x}\right)^3 \left(\frac{D_x}{D_t}\right)^3} \quad (18)$$

From formula (13)

$$\frac{Ft}{N_x} = \frac{R(1+r)}{a_{xx} + a_{xt}r} \quad (19)$$

From formula (14)

$$L = \frac{1}{1+r} \quad (20)$$

and from formula (15)

$$N = \frac{r}{1+r} = 1 - L$$

Formulas (16)-(20) are very easily arranged into computer programs. For example, if the stress coefficient and  $F_a$  are taken to be the numerical values of the above examples after going through an electronic computer we can obtain the following table

$\frac{N_f}{N_s}$	0	0.1	0.2	0.3	0.4	0.5	0.6	0.7	0.8	0.9	1.0
$\frac{F_{at}}{N_s}$	(1)	1.043	1.370	1.667	1.947	2.217	2.481	2.738	2.992	3.242	3.489
$L$	(1)	1.229	0.979	0.826	0.718	0.636	0.571	0.517	0.472	0.433	0.399

If the data in the table are drawn into figure lines then it is as shown in fig. 5.

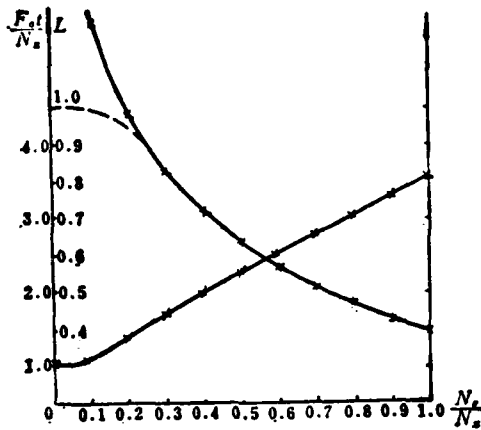


Fig. 5. The  $N_s/N_x - F_a t/N_x - L$  Relation Curve

When  $\frac{N_s}{N_x}$  is very small, we know from formula (16) that  $\frac{D_x}{D_s}$  will be very large and especially when  $\frac{N_s}{N_x} = 0$ ,  $\frac{D_x}{D_s}$  will become infinite. In reality, however, when  $\frac{N_s}{N_x} = 0$ , that is it becomes the single load of  $N_s = N_y = 0$  and  $N_x \neq 0$  then there should be  $\frac{F_a t}{N_x} = 1$  and  $L = 1$ . Therefore, the  $L - \frac{N_s}{N_x}$  curve in fig. 5 should take a value in accordance with the dotted line when  $\frac{N_s}{N_x}$  is smaller than a certain value (for example, taking  $\frac{N_s}{N_x} = 0.3$ ). The dotted line area shows the transformations within two types (single load and double load) of minimum weight designs. Because of the selection of the dotted line area's curve form and stopping point there is a certain randomness and therefore its error can be relatively large.

## V. Discussion of Technique

1. Can we differentiate and determine the number of layers of each directional layer based on the external load of each direction?

Also, is it possible to carry out a lamination design based on the  $t_k = \frac{N_k}{a_{kk} F_a}$  ( $k=x, y, s$ ) formula. When we still take the above example's data, we can obtain:

$$\begin{aligned} t_x &= \frac{10}{173} = 0.0578 \text{ 英寸}^{(1)}, & n_x &= \frac{0.0578}{0.0075} = 7.71 \approx 8 \text{ 层}^{(2)} \\ t_y &= \frac{5}{173} = 0.0289 \text{ 英寸}^{(3)}, & n_y &= \frac{0.0289}{0.0075} = 3.85 \approx 4 \text{ 层}^{(4)} \\ t_s &= \frac{3.183}{0.4266 \times 173} = 0.0431 \text{ 英寸}^{(5)}, & n_s &= \frac{0.0431}{0.0075} = 5.74 \approx 6 \text{ 层}^{(6)} \end{aligned}$$

Key: 1. Inch  
2. Layer  
3. Inch  
4. Layer  
5. Inch  
6. Layer

We know that the differences of the optimum schemes in the contrasting examples are relatively large and it appears that the main reason for these differences is, as regards the laminated plate, causing the external load to be single directional. The stress conditions of each directional layer are still complex stress conditions (if we do not calculate the stress in the layer then they are plane stress conditions) and the interaction within each directional layer cannot be overlooked.

2. Stress coefficient  $a_{kj}$  and single direction composite

longitudinal tensile strength  $F_a$

We can see from the numerical examples that the influence of the numerical value of  $a_{kj}$  on the calculation results is quite large. The value of  $a_{kj}$  is obtained from special single load tests based on the different percentages of each layer of the composite on the x, y and s axes. In the same way,  $F_a$  is also determined from the tests.

### 3. Strength Data

We must take into account that this paper used the laminated plate's strength criteria and that this was for a non-singular laminated plate. Therefore, each of its data items should use the laminated plate. The above mentioned formulas were based on the Norris criteria yet if we use the Hill-Tsai criteria then the formulas can have fewer differences and yet its results can also have some dissimilarities. However, the two formulas are not dissimilar for the  $\frac{N_s}{N_x} \neq 0$  and  $\frac{N_y}{N_z} \neq 0$  situations. If we use the Tsai-Wu tensor multinomial criteria, the derived formula is quite complex and inconvenient to use because there are very many number items and also because it is necessary to use the tensile and compression limit strength. Therefore, it is more convenient to use the previous two types of criteria during the preliminary design.

### References

1. AFFDL-TR-74-20 "PRELIMINARY DESIGN OF WINGS Volume-Minimum Weight Design of Composite Structure" (AD A003667)

### Abstract

When the upper and/or lower panels of the loading box of the aircraft wing or tail are made of the fiber reinforced composite laminates, they can frequently be simplified as a non-moment plate. This paper introduces an optimum design (i. e. minimum weight design) procedure of the laminated plate on static failure strength condition. The mathematical tool used in the procedure is Lagrangian Multiplier method, and the static failure strength condition is adopted as Hill-Tsai criteria or Norris criteria.

The formulae for optimum design have been not only derived, but also reformed to be convenient for the computer. How to establish the ultimate strength of laminates is discussed in detail. An example, illustrating the solution procedure and how to select the optimum scheme of lamination design, is presented in the paper. Some technical problems are briefly discussed in the last part.

At the stage of the preliminary structural design, this procedure can be considered as an engineering method of lamination optimum design for the loading panel of laminated composite, which works under tension or compression (assuming that the buckling failure would not occur).